

DEPARTMENT OF MECHANICAL ENGINEERING & MECHANICS
COLLEGE OF ENGINEERING & TECHNOLOGY
OLD DOMINION UNIVERSITY
NORFOLK, VIRGINIA 23529

INVESTIGATION OF RADIATIVE INTERACTIONS IN
SUPERSONIC INTERNAL FLOWS

By

S. N. Tiwari, Principal Investigator

and

A. M. Thomas

IN-02-CR

40381

P-153

Progress Report

For the period ended May 31, 1991

Prepared for
National Aeronautics and Space Administration
Langley Research Center
Hampton, Virginia 23665

Under

Research Grant NAG-1-423

Drs. J.P. Drummond and A. Kumar, Technical Monitor
FLDMD-Theoretical Flow Physics Branch

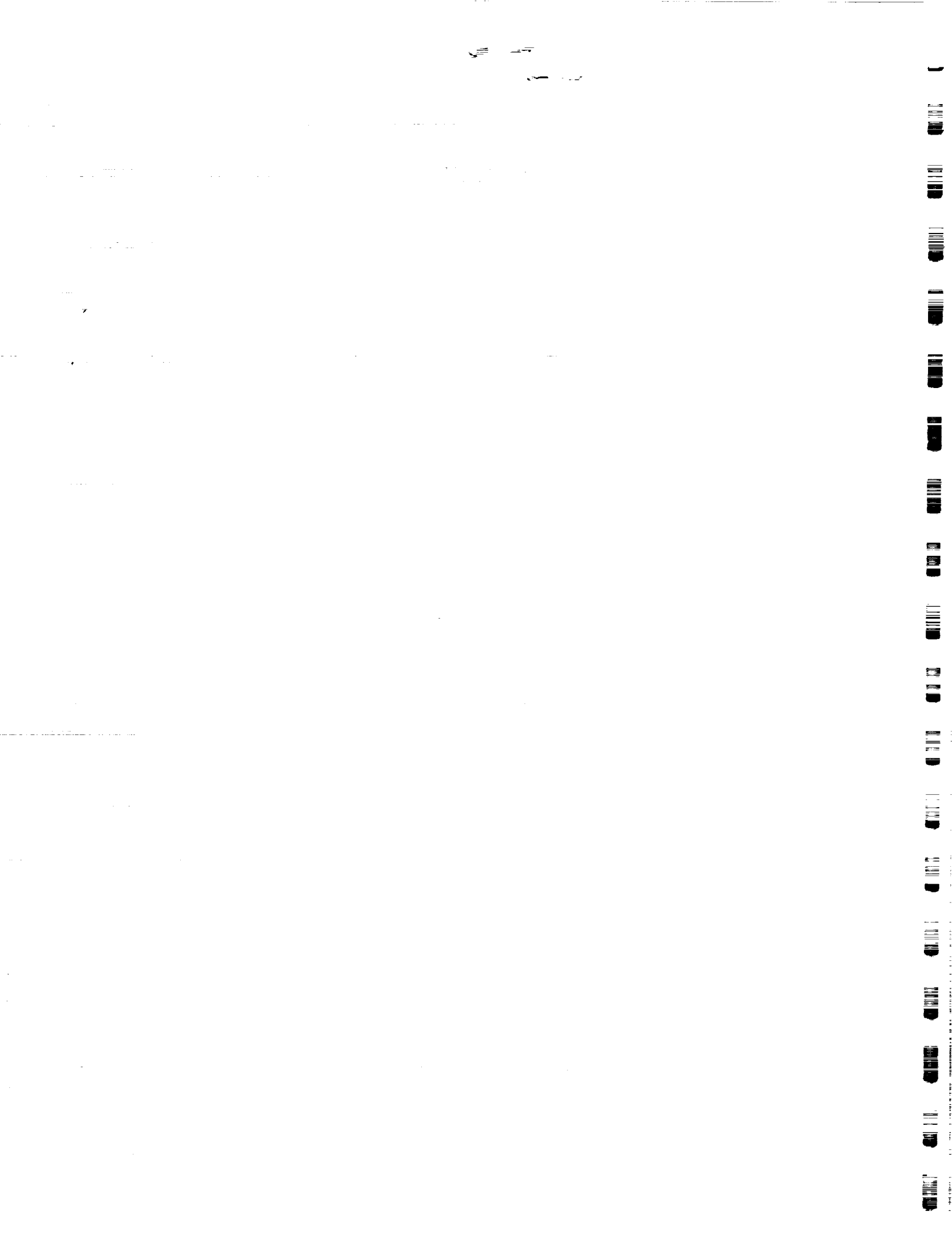
(NASA-CR-188820) INVESTIGATION OF RADIATIVE
INTERACTIONS IN SUPERSONIC INTERNAL FLOWS
Progress Report, period ending 31 May 1991
(Old Dominion Univ.) 153 p CSCL 01A

N91-32078

Unclass
0040381

G3/02

October 1991



DEPARTMENT OF MECHANICAL ENGINEERING & MECHANICS
COLLEGE OF ENGINEERING & TECHNOLOGY
OLD DOMINION UNIVERSITY
NORFOLK, VIRGINIA 23529

**INVESTIGATION OF RADIATIVE INTERACTIONS IN
SUPERSONIC INTERNAL FLOWS**

By

S. N. Tiwari, Principal Investigator

and

A. M. Thomas

Progress Report
For the period ended May 31, 1991

Prepared for
National Aeronautics and Space Administration
Langley Research Center
Hampton, Virginia 23665

Under
Research Grant NAG-1-423
Drs. J.P. Drummond and A. Kumar, Technical Monitor
FLDMD-Theoretical Flow Physics Branch

Submitted by the
Old Dominion University Research Foundation
P.O. Box 6369
Norfolk, Virginia 23508-0369



October 1991

PAGE _____ INTENTIONALLY BLANK

INVESTIGATION OF RADIATIVE INTERACTIONS IN SUPERSONIC INTERNAL FLOW

By

S.N.Tiwari¹ and A.M. Thomas²

SUMMARY

Analyses and numerical procedures are presented to investigate the radiative interactions of absorbing emitting species in chemically reacting supersonic flow in various ducts. The two-dimensional time dependent Navier-Stokes equations in conjunction with radiative flux equation are used to investigate supersonic flows undergoing finite rate chemical reaction in a hydrogen air system. The specific problem considered is the flow of premixed radiating gas between parallel plates. Specific attention was directed toward investigating the radiative contribution of H_2O , OH , and NO under realistic physical and flow conditions. Results are presented for the radiative flux obtained for different gases and for various combination of these gases. The problem of chemically reacting and radiating flows was solved for the flow of premixed hydrogen-air through a 10° compression ramp. Results demonstrate that the radiative interaction increases with an increase in pressure, temperature, amount of participating species, plate spacing, and Mach number. Most of the energy, however, is transferred by convection in the flow direction. In general the results indicate that radiation can have a significant effect on the entire flow field.

¹Eminent Professor, Department of Mechanical Engineering and Mechanics, Old Dominion University, Norfolk VA 23529.

²Graduate Research Assistant, Department of Mechanical Engineering and Mechanics, Old Dominion University, Norfolk VA 23529.

PAGE _____ INDIVIDUALLY BLANK

ACKNOWLEDGEMENTS

This is a progress report on the research project, "Analysis and Computation of Internal Flow Field in a Scramjet Engine," for the period ended May 31, 1991. Special attention during this period was directed to "Investigation of Radiative Interactions in Supersonic Internal Flows."

This was supported by the NASA Langley Research Center (Theoretical Flow Physics Branch of the Fluid Mechanics Division) through the grant NAG-1-423. The grant was monitored by Drs. J.P. Drummond and A. Kumar of FLDMD-Theoretical Flow Physics Branch. The work, in part, was also supported by the Old Dominion University ICAM Project through NASA grant NAG-1-363; this grant was monitored by Dr. Samuel E. Massenberg, University Affairs Officer, NASA Langley Research Center, Hampton, Virginia 23665-5225. The authors express their sincere thanks to Dr. D.J. Singh of Analytical Services and Materials, Inc. for providing assistance in computational procedures used in this study.

PAGE _____ INTERNATIONALLY BLIND

TABLE OF CONTENTS

	<u>Page</u>
SUMMARY	iii
ACKNOWLEDGEMENTS	iv
LIST OF TABLES	vii
LIST OF FIGURES	viii
LIST OF SYMBOLS	xi
Chapter	
1 INTRODUCTION	1
2 GENERAL FORMULATION	7
2.1 Physical Model	7
2.2 Basic Governing Equation	14
2.3 Chemistry Model	18
2.4 Thermodynamic Model	22
3 RADIATION TRANSPORT MODEL	25
3.1 Radiation Absorption Model	25
3.2 Evaluation of Planck Function and Planck Mean Absorption Coefficient	28
3.3 Radiative Flux Equation	31
3.3.1 Basic Formulation	31
3.3.2 Gray Formulation	34

4	METHOD OF SOLUTION	38
4.1	Grid Generation	38
4.2	Solution of the Governing Equations	39
4.3	Physical Conditions and Data Source	42
5	RESULTS AND DISCUSSION	44
6	CONCLUSIONS	74
	REFERENCES	75
	APPENDICES	80
A	DERIVATION OF THE CONDUCTION HEAT FLUX TERM	81
B	RADIATIVE FLUX EVALUATION FOR THE PSEUDO GRAY MODEL	83
C	EXPONENTIAL KERNAL APPROXIMATION	88
D	COMPONENTS OF THE JACOBIAN MATRIX	92
E	PROGRAM FOR THE CALCULATION OF PLANCK MEAN ABSORPTION COEFFICIENT	94
F	AIAA PAPER NO. AIAA-91-0373	103
G	AIAA PAPER NO. AIAA-91-0572	115

LIST OF TABLES

<u>Table.</u>		<u>Page</u>
2.1	Hydrogen-Air combustion mechanism.	21
2.2	Numerical values of various constants.	24

PAGE ~~1~~ UNCLASSIFIED EONE

LIST OF FIGURES

<u>Figure.</u>		<u>Page</u>
2.1	Propulsion alternative.	9
2.2	Airframe-integrated supersonic combustor.	10
2.3	Physical model for absorbing-emitting medium.	11
2.4	Radiating gas flow within a circular tube.	12
2.5	Radiating gas flow in a 10° compression ramp.	13
3.1	Coordinate system for one-dimensional radiative transfer. . . .	32
5.1	Variation of the Planck mean absorption coefficient for H_2O , NO and OH.	45
5.2	Variation of the Planck mean absorption coefficient for different mixtures of H_2O , NO and OH.	46
5.3	Radiative flux vs y at the channel exit, $M_\infty=3.0$	48
5.4	Radiative flux vs y for $P = 1$ atm and 3 atm, $x = 5$ and 10 cm, 50 % H_2O , $M_\infty = 3.0$	49
5.5	Radiative and conductive fluxes vs y for $P = 3$ atm, $x = 5$ and 10 cm, 50 % H_2O , $M_\infty = 3.0$	50
5.6	Radiative flux vs y for H_2O , NO and OH, $P=1$ atm, $M_\infty=3.0$.	52
5.7	Radiative flux vs y for two different plate spacing ($L = 3$ and 6 cm) at $x = 5$ and 10 cm, $M_\infty = 3.0$	53

5.8	Radiative flux vs y for 50 % and 100 % H_2O , $x = 10$ cm, $M_\infty = 3.0, 4.5$	54
5.9	Radiative flux vs y for channel and tube ($L = D = 3$ cm) at x $= 5$ and 10 cm, 50 % H_2O , $M_\infty = 3.0$	55
5.10	Variation of axial velocity across the channel at various x locations.	56
5.11	Temperature variation across the channel at various x locations.	57
5.12	Variation of axial velocity across the channel at various x locations.	59
5.13	Temperature variation across the channel at various x locations, $M_\infty=3.0$, $T_w = 3000$ K.	60
5.14	Variation of q_{RY} with y for different x -locations, $M_\infty = 3.0$, $T_w = 3000$ K.	61
5.15	Variation of axial velocity across the channel at various x locations, $M_\infty = 3.0$, $T_w = 1000$ K.	62
5.16	Temperature variation across the channel at various x locations, $M_\infty = 3.0$, $T_w = 1000$ K.	63
5.17	Variation of q_{RY} with y for different x -locations, $M_\infty = 3.0$, $T_w = 1000$ K.	64
5.18	Temperature variation with x for reacting, and reacting and radiating flows.	66
5.19	Pressure variation with x for reacting, and reacting and radiating flows.	67

5.20	Variation of H_2 and O_2 for reacting flows.	69
5.21	Variation of H_2O mass fraction with x for reacting, and reacting and radiating flows.	70
5.22	Variation of OH mass fraction with x for reacting, and reacting and radiating flows.	71
5.23	Variation of normal radiative flux with x for three chemistry models.	72
5.24	Variation of streamwise radiative flux with x for three chemistry models.	73

PAGE INTENTIONALLY BLANK

LIST OF SYMBOLS

A	band absorptance, m^{-1}
A_0	band width parameter, m^{-1}
C_j	concentration of the jth species, kg-mole/m^3
C_p	constant pressure specific heat, J/kg-K
D	diffusion coefficient
e_b	black body radiation, σT^4 , $\text{J/m}^2\text{s}$
e_w	Planck's function, $\text{J/m}^2\text{-s}$
E	total internal energy, J/kg
f_j	mass fraction of the jth species
h	static enthalpy of mixture, J/kg
H	total enthalpy, J/kg
$I_{b\nu}$	spectral Planck function
k	thermal conductivity, J/m-s-K
P_j	partial pressure of the jth species, N/m^2
Pr	Prandtl number
q_R	total radiative heat flux, $\text{J/m}^2\text{-s}$
R	gas constant, J/kg-K
S	integrated band intensity, $(\text{N/m}^2)^{-1}\text{-m}^{-2}$
T	temperature, K

v	velocity in y direction, m/s
u	velocity in x direction, m/s
z	dummy variable in the y direction
α	heat diffusion coefficient
γ	ratio of specific heats
κ	absorption coefficient
κ_p	Planck mean absorption coefficient
λ	second coefficient of viscosity, wave length, m
μ	dynamic viscosity (laminar flow), kg/m-s
ρ	density, kg/m ³
σ	Stefan-Boltzmann constant, erg/s-cm ² -K ⁴
τ	shear stress, N/m ²
ϕ	equivalence ratio
ω	wave number, m ⁻¹

Chapter 1

INTRODUCTION

In the past several years, there has been a great deal of research toward development of a hypersonic transatmospheric vehicle. At NASA Langley Research Center, the hydrogen-fueled Supersonic combustion ramjet (Scramjet) engine has been a strong candidate for propelling such a vehicle. Both experimental and numerical techniques are being employed for a better understanding of the complex flow field in different regions of the engine.

During the past two decades, tremendous progress has been made in the field of radiative energy transfer in nonhomogeneous nongray gaseous systems. There is a renewed interest in investigating various aspects of radiative energy transfer in participating medium. Radiative interactions have become important in many engineering problems involving high temperature gases. Recent interest lies in the areas of design of high pressure combustion chambers and high enthalpy nozzles, entry and reentry phenomena, hypersonic propulsion, and defense oriented research.

Basic formulations on radiative energy transfer in participating media are available in standard references [1-5]*. The review articles presented in [6-15] are useful in understanding the radiative properties of participating species and the nature of nongray radiation. The validity of radiative transfer analyses depends upon the accuracy with which absorption-emission and scattering characteristics of participating species

* The numbers in brackets indicate references

are modeled. There are several models available to present the absorption-emission characteristics of molecular species and these are reviewed in [12,13]. These models have been used to investigate radiative interactions in several duct flows [16–29].

In a hypersonic propulsion system, the temperature ranges from 1000 – 5000 K. In this range various nonsymmetric molecules such as H_2O , CO_2 and OH become highly radiative participating. Infrared absorption and emission of thermal radiation is a consequence of coupled vibrational and rotational energy transitions. A diatomic molecule is the simplest molecule that will undergo such transition. However, symmetric diatomic molecules, such as H_2 , O_2 , and N_2 have no permanent dipole moment and thus are transparent to infrared radiation. For unsymmetric diatomic and triatomic molecules, such as OH , CO , CO_2 , and H_2O , the infrared spectrum will consist of fundamental vibration-rotation bands occurring at the fundamental frequencies of vibration of the molecule, followed by overtone and combination bands [1].

In the combustion temperature range, some diatomic and triatomic molecules are highly radiative participating species. Various investigators have studied the effect of radiative transfer for channel flows. Marting and Hwuang [30] solved the energy equation for steam flowing between two parallel black walls. The flow was assumed to be steady and the radiation transfer in the flow direction was neglected. It was shown that radiative flux peaks at a small distance from the wall, instead of at the wall. This effect was also noted by Viskanta in a gray analysis for radiation and convection interaction between plates of constant temperatures [31]. This is because at the wall the effect of positive radiant heat flux from the wall is partially cancelled by the negative flux from the layers of hot gas next to the wall. At a small distance into the stream, however, the flux from the wall and hot gas combine to give a maximum heat flux.

Kobiyama et al. [32] studied the problem of combined radiation and convection for compressible laminar flow between two isothermal parallel plates. A comparison between temperature profiles calculated with the treatment of one and two dimensional radiation shows a considerable temperature difference at the entrance region of the heating zone. The problem of combined convection and radiation in a rectangular duct was studied also by Im and Ahluwalia [33] for compressible turbulent flows. The moment method was employed in this study to solve the radiative flux equation. It was concluded that radiative heat transfer causes the thermal boundary layer to grow and skin friction to decrease. The velocity profile was not effected by the radiative heat transfer.

The problem of radiative interaction of gray and nongray absorbing – emitting species between two parallel plates and in a circular tube was studied by Tiwari et al. [34]. In this study, both laminar fully developed incompressible as well as entrance region subsonic flows were considered. Results showed that radiative interactions were quite significant in fully developed incompressible flows. For subsonic flows, the flow field was found to change significantly due to radiative interaction. Tiwari and Singh [20] investigated the transient radiative interactions of nongray absorbing emitting species in laminar fully developed flows between two parallel plates. The particular species considered were OH, CO, CO₂, H₂O, and different mixtures of these species. Their results demonstrated that H₂O is a highly radiation participating species compared to CO₂, CO, and OH. The effect of radiation increases with increasing plate spacing, and the radiative heat transfer was more pronounced at higher wall temperature and pressure. It was also shown that optically thin limits overestimates the influence of radiation. Soufiani and Taine [35] studied the H₂O – air mixture for the above geometry and reached the same conclusion .

For numerical investigation of chemically reacting flows, an appropriate chemistry model must also be selected. Depending on the ratio of the chemical and fluid dynamic time scales, the suitable chemistry model could be a frozen flow model, a finite rate model, an equilibrium (a complete reaction) model. In general, the finite rate model is the most accurate one. In the past several years, a number of finite rate chemistry models for hydrogen – air systems have been introduced in the literature. Rogers and Schenayder [36] proposed as many as 60 reaction paths in their model; this is certainly one of the most complete representatives of hydrogen – air reaction. Unfortunately, the enormous number of reaction paths and chemical species involved in the model makes it unfeasible for numerical investigation of engineering problems. Intermediate level models are reduced to 12 species and 25 reaction paths, and eight species and eight reaction paths. Except for some inaccuracies during the ignition delay period, the eight reaction path model performs as well as the 25 reaction path model. Although these models are less tedious than the 60 path model, they are expected to be too costly for use in routine parametric studies. The global two step model proposed by Rogers and Chinitz [37] is an inexpensive and attractive model for preliminary investigation of reacting flows. This model was deduced by fitting the temperature history of a 28 reaction model [38] used in a series constant pressure stream – tube calculations. There are a number of limitations to this model, such as ignition phase inaccuracy and a tendency to overpredict the flame temperature. This model is considered primarily for initial parametric study.

A more realistic chemistry model was used by Drummond [23] in numerical simulation of a supersonic reacting mixing layer. To explore the behavior of such flows, detailed physical models of convective and diffusive mixing and finite rate chemical reactions in supersonic flow were developed. The finite rate chemistry model consisted of 18 reaction paths and nine species. In this study, two numerical algorithms were

constructed to solve the governing equations. The first algorithm was developed by modifying the unsplit finite difference scheme of MacCormack. The second algorithm employed a hybrid pseudo - spectral technique in the normal to the flow direction for improved resolution of the reacting flowfield. The finite difference algorithm was used in the streamwise direction. It is important to note that the use of a more complete chemistry model rather than the global model in the fluid dynamics equation did not result in a set of temporally stiff equations. Incorporation of the finite rate chemistry model into the fluid dynamics equation can create a set of stiff differential equations. The stiffness is due to a disparity in the time scale of the governing equations. In a time - accurate solution, after the large initial transients have decayed and the solution is changing slowly, taking a larger time step is necessary for efficiency purposes; but explicit methods still require small time steps to maintain stability. An eigenvalue problem with stiff ordinary differential equation (ODE) has been solved to express this clearly in [39]. One way around the problem is to use a fully implicit method. This method however requires the inversion of a large coupled system of linear algebraic equations. The use of a semi - implicit technique, suggested by several investigators [40] provides an alternative to the above problem. In this technique the source term, which is the cause of stiffness, is treated implicitly, and the other terms in the governing equations are treated explicitly.

A comparison of different chemistry models used in investigating radiative interactions was done by Chandrasekhar et al. [28]. The results indicated that the 2 step model predicts ignition before the shock (shorter ignition delay) due to high temperatures in the boundary layer, while the 18 - step model predicts a longer ignition delay. The ignition delay predicted by the 35 - step model appeared to be the average of the above two models. A grid sensitivity analysis was also conducted, and it was

found that a 31 X 31 grid was the most appropriate grid.

The purpose of this study is to investigate the effect of radiative heat transfer in chemically reacting supersonic flow in various ducts under different physical and flow conditions. This provides essential information for investigating the effect of radiative interactions in the combustor of a supersonic combustion ramjet (scramjet) engine. Several codes have been developed to compute the flow field in a scramjet engine [21–24]. The combustion of hydrogen and air results in absorbing - emitting gases such as H_2O , OH and NO . Specific attention, therefore, is directed towards investigating the radiative contribution of these gases under realistic conditions. Based on the study of Ref. 28, a 31 X 31 grid was selected for this study with the 18 step chemistry model. The basic code is converted for the axisymmetric case and several parametric studies are conducted.

A brief discussion of the scramjet engine and the physical problem considered is presented in Chap. 2 along with the governing equations. Chapter 3 provides the formulation of the absorption coefficient and the pseudo-gray model for the absorbing-emitting species. The grid generation technique and solution procedure for the governing equations are presented in Chap. 4. Discussion of the results for several specific cases are provided in Chap. 5, and specific conclusions and recommendations for future studies are provided in Chap. 6.

Chapter 2

GENERAL FORMULATION

2.1 Physical Model

As mentioned in the introduction, the scramjet engine has been a candidate for propelling hypersonic vehicles. In Fig. 2.1, various air breathing and rocket propulsion alternatives are shown. For Mach numbers zero to three, turbojet air-breathing systems have the highest performance. Above a free stream Mach number of three, turbine inlet temperatures constrain performance, and the ramjet becomes more attractive. At about a Mach number of six, the performance of ramjet is greatly reduced. This is due to the dissociation of the reaction products, which is caused by slowing the supersonic flow to subsonic flow through the normal shock that exist in a ramjet. Therefore it is more efficient to allow the engine internal flow to remain at a supersonic speed. Thus for Mach numbers of six and beyond, the fixed geometry scramjet is clearly superior for propelling a vehicle at hypersonic speeds. Hydrogen has been selected as the fuel for the scramjet due to its capability of cooling the engine and the airframe and also because of its high impulse level.

The scramjet engine has several identical modules as shown in Fig. 2.2. The forebody of the aircraft acts as an inlet for precompression and the afterbody as a nozzle for post expansion. The inlet region starts with the forebody of the vehicle and ends with the minimum cross sectional area of each module. In the first part, the air is

compressed by the oblique shock generated from the forebody before it enters the engine. For numerical solution, the flow is best represented by the Navier-Stokes equations in the inlet area of the engine. Using the Euler equations away from the wall region and the boundary layer equation near the wall region can be complicated by the oblique shock interaction with the boundary layer. This can cause flow separation and as a result flow cannot be represented by these equations. Three-dimensional Navier-Stokes equations have been successfully employed by Kumar [21] to investigate the flow field in this region. Chitsomboom et al. [24] have employed the parabolized Navier-Stokes equations to solve this problem, with limited success.

The combustor region is the most complex part of the scramjet engine flow field. As a result, a great deal of research is directed toward better understanding of the combustor flow field. The flow in this region is mostly supersonic, but does have a subsonic region near the fuel injection region. The fluid dynamics become complicated by the fuel injection, flame holding, chemistry, radiation and turbulence. The flow field in this region is represented by the Navier-Stokes equations, turbulence, chemistry and radiation modelling equations. Downstream of the fuel injection strut, the flow can be represented by the parabolized Navier-Stokes equations [24]

The physical problems considered here to investigate the effects of radiative interactions in supersonic flow are two-dimensional laminar flow between parallel plates (Fig. 2.3) and within a circular tube (Fig. 2.4). Another geometry is considered to study the effect of shocks and chemical reactions on the radiative heat transfer and this consists of a channel with a compression-expansion ramp (Fig. 2.5). The governing equations and boundary conditions are provided here for all physical problems considered in this study.

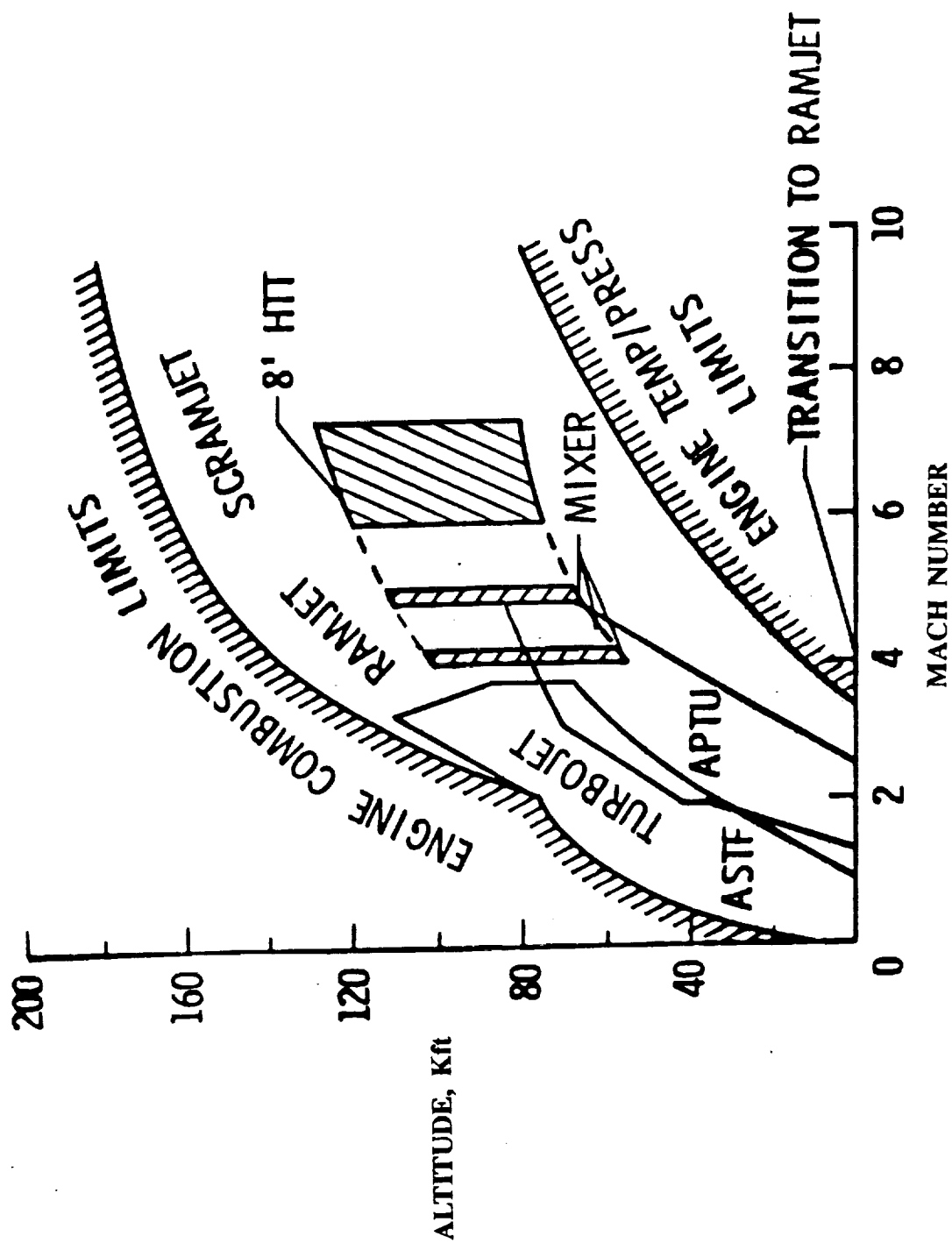


Fig. 2.1 Propulsion alternative

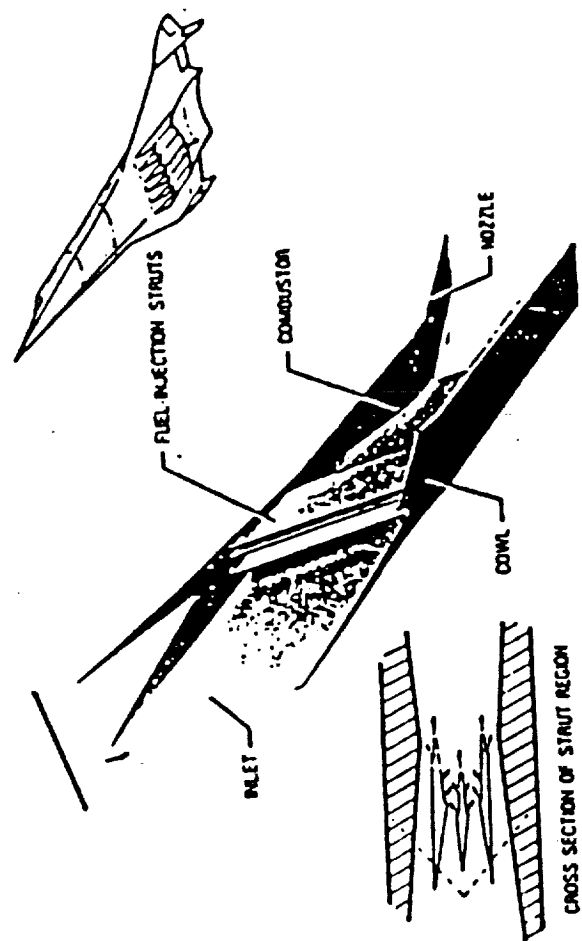
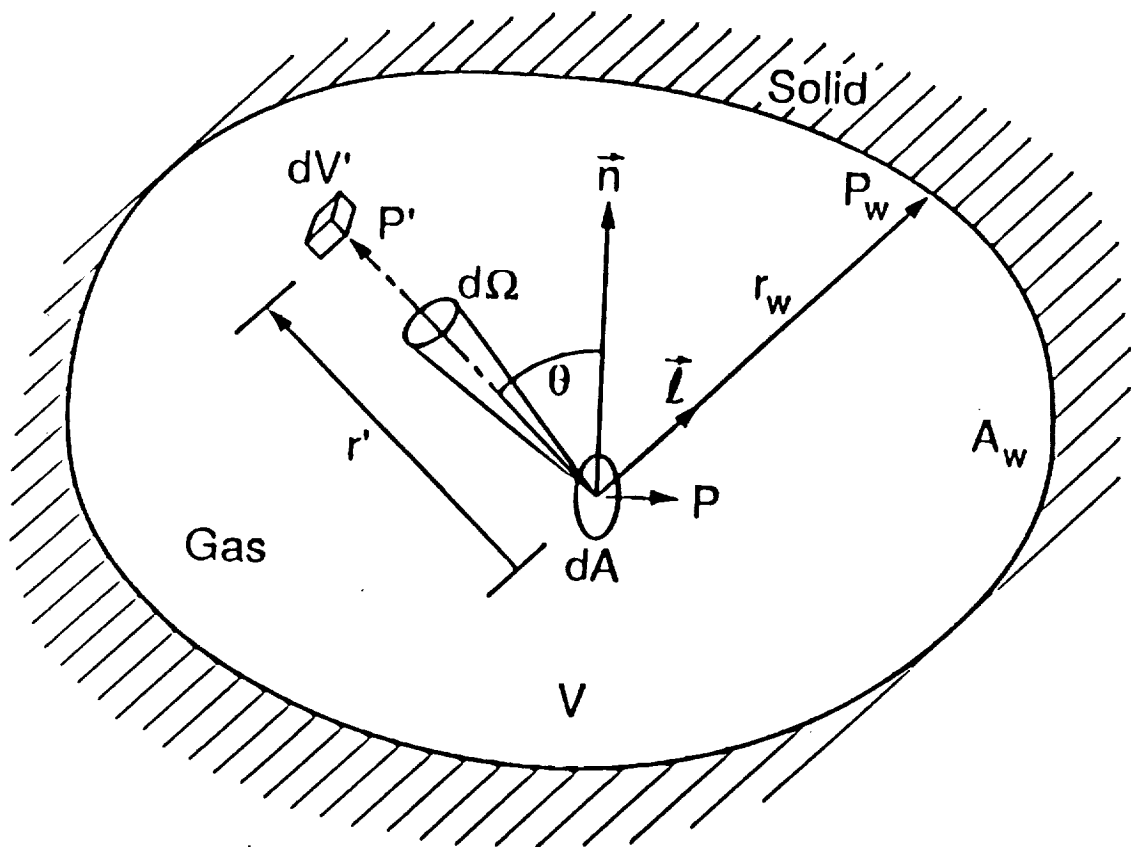
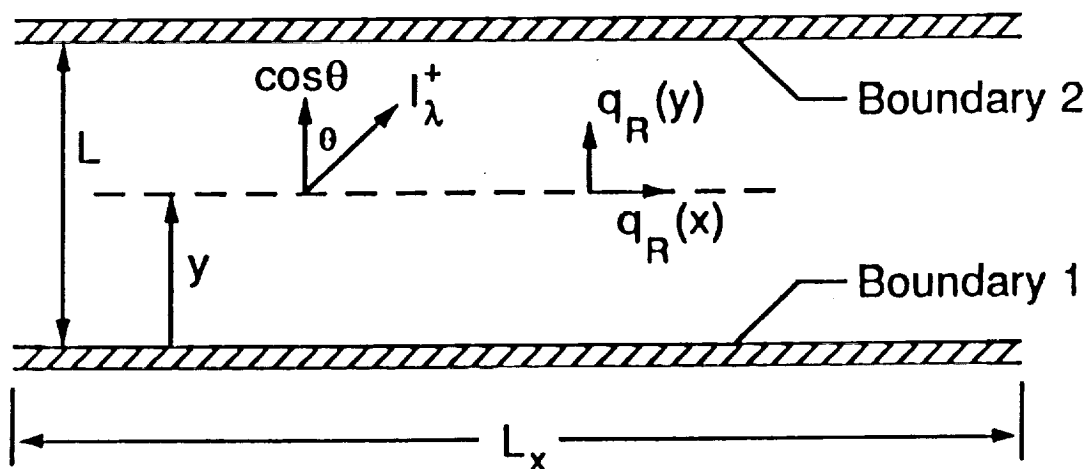


Fig. 2.2 Airframe-integrated supersonic combustion.



(a) Arbitrary configuration.



(b) Plane radiating layer between parallel boundaries.

Fig. 2.3 Physical model for absorbing-emitting medium.

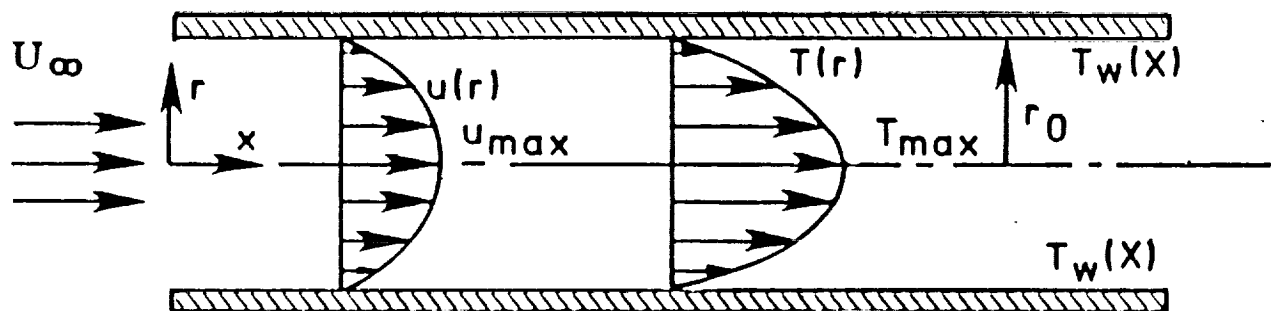


Fig. 2.4 Radiating gas flow within a circular tube.

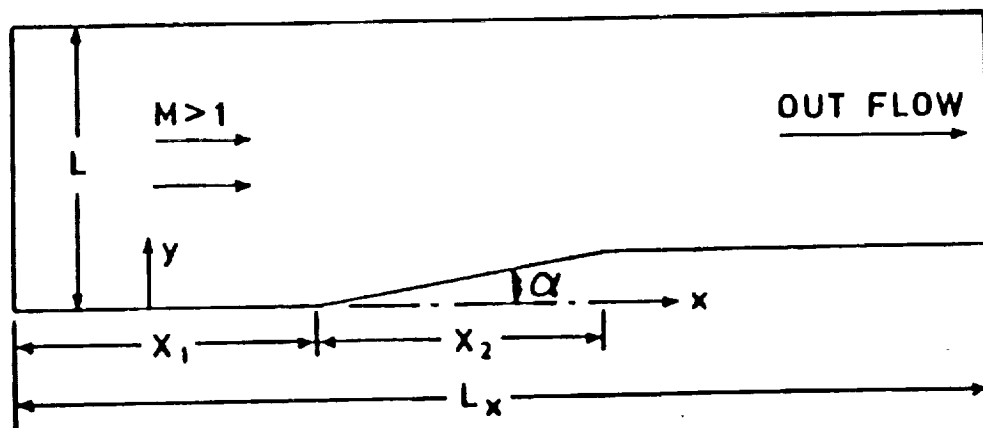


Fig. 2.5 Radiating gas flow in a channel with a compression-expansion ramp.

2054 111431000000 01/20/00

2.2 Basic Governing Equation

The physical problem considered here for basic understanding of radiative interaction in supersonic flows is a two-dimensional variable property laminar flow between two parallel plates. For this model, the two-dimensional Navier-Stokes equations in fully conservative form are used to describe the flow field. These equations, in cartesian coordinates, can be written as [25,29]

$$\frac{\partial \mathbf{U}}{\partial t} + \frac{\partial \mathbf{F}}{\partial x} + \frac{\partial \mathbf{G}}{\partial y} + \mathbf{H} = 0 \quad (2-1)$$

where \mathbf{U} , \mathbf{F} , \mathbf{G} and \mathbf{H} are expressed as

$$\mathbf{U} = \begin{Bmatrix} u \\ \rho u \\ \rho v \\ \rho E \\ \rho f_j \end{Bmatrix}, \quad \mathbf{F} = \begin{Bmatrix} \rho u \\ \rho u^2 - \tau_{xx} \\ \rho uv - \tau_{xy} \\ (\rho E + p)u - \tau_{xy}v + q_{cx} + q_{rx} \\ \rho u f_j - \rho D \frac{\partial f_j}{\partial x} \end{Bmatrix}$$

$$\mathbf{G} = \begin{Bmatrix} \rho v \\ \rho uv - \tau_{xy} \\ \rho v^2 - \tau_{yy} \\ (\rho E + p)v - \tau_{xy}u + q_{cy} + q_{ry} \\ \rho v f_j - \rho D \frac{\partial f_j}{\partial y} \end{Bmatrix}, \quad \mathbf{H} = \begin{Bmatrix} 0 \\ 0 \\ 0 \\ 0 \\ -\dot{w}_j \end{Bmatrix}$$

The viscous stress tensor in the \mathbf{F} and \mathbf{G} terms of Eq. (2-1) are given as

$$\tau_{xx} = -p + \lambda \left(\frac{\partial u}{\partial x} + \frac{\partial v}{\partial y} \right) + 2\mu \frac{\partial u}{\partial x} \quad (2-2a)$$

$$\tau_{xy} = \mu \left(\frac{\partial u}{\partial y} + \frac{\partial v}{\partial x} \right) \quad (2-2b)$$

$$\tau_{yy} = -p + \lambda \left(\frac{\partial u}{\partial x} + \frac{\partial v}{\partial y} \right) + 2\mu \frac{\partial v}{\partial y} \quad (2-2c)$$

The quantities q_{cx} and q_{cy} in F and G terms are the components of conduction heat flux and are expressed as

$$q_{cx} = -k \frac{\partial T}{\partial x} - \rho D \sum_{j=1}^m \left[\left(\frac{\partial f_j}{\partial x} \right) h_j \right] \quad (2-3a)$$

$$q_{cy} = -k \frac{\partial T}{\partial y} - \rho D \sum_{j=1}^m \left[\left(\frac{\partial f_j}{\partial y} \right) h_j \right] \quad (2-3b)$$

where

$$h_j = h_j^0 + \int_{T_0}^T C_{p_j} dT, \quad T_0 = 0 \text{ K}$$

It should be noted that D represents the binary diffusion coefficient and is used for all species. Assuming that the Lewis number (α/D) is unity, Eq. (2-3) reduces to (see Appendix A)

$$q_{cx} = -\frac{\gamma \mu}{pr} \frac{\partial e}{\partial x} \quad (2-4a)$$

$$q_{cy} = - \frac{\gamma \mu}{pr} \frac{\partial e}{\partial y} \quad (2-4b)$$

where $e = h - P/\rho$. The molecular viscosity, μ_e , is assumed to be only temperature dependent, and is evaluated from the Sutherlands formula as

$$\mu_e = \mu_0 \left(\frac{T}{T_0} \right)^{\frac{3}{2}} \frac{T_0 + S}{T + S} \quad (2-5)$$

where μ_0 and T_0 are reference values for individual species and S is the Sutherland constant. Here the reference values were selected for pure air because the flow is dominated by nitrogen. The total internal energy E is given by

$$E = \frac{P}{\rho} + \frac{u^2 + v^2}{2} + \sum_{i=1}^m h_i f_i \quad (2-6)$$

Equation (2-1) can be used to obtain solutions for various kinds of compressible flows. However, boundary conditions and numerical procedures for different flows are quite different. For supersonic flows, the inflow conditions are specified and outflow conditions are obtained by extrapolation. The boundary conditions used along solid surfaces are $u=0$, $v=0$, $\frac{\partial P}{\partial y} = 0$, and $T = T_w$.

The governing equations and boundary conditions for the supersonic flow through a channel with a compression-expansion ramp are essentially the same as for the parallel plate geometry. However, a strong shock is produced at the compression corner and the flow becomes highly reacting from the begining of the x_2 -coordinate (Fig. 2.5).

The basic governing equation for chemically reacting compressible flow through a circular tube can be written as [39]

$$\frac{\partial \mathbf{U}}{\partial t} + \frac{\partial \mathbf{F}}{\partial x} + \frac{1}{y} \frac{\partial (y\mathbf{G})}{\partial y} + \frac{\mathbf{H}}{y} = 0 \quad (2-7)$$

where x , y represent streamwise and radial coordinates, respectively. In Fig. 2.4, the radial coordinate is denoted by r . The definitions of \mathbf{U} , \mathbf{F} and \mathbf{G} in Eq. (2-7), are same as given in Eq. (2-1) but vector \mathbf{H} is expressed as

$$\mathbf{H} = \begin{Bmatrix} 0 \\ 0 \\ \mathbf{P} + \lambda_{\theta\theta} \\ 0 \\ -\dot{\mathbf{w}}_j \end{Bmatrix} \quad (2-8)$$

The viscous terms in this case are given by

$$\tau_{xx} = \lambda \left(\frac{\partial \mathbf{u}}{\partial x} + \frac{\partial \mathbf{u}}{\partial y} + \frac{\mathbf{u}}{y} \right) + 2\mu \frac{\partial \mathbf{u}}{\partial x} \quad (2-9a)$$

$$\tau_{yy} = \lambda \left(\frac{\partial \mathbf{u}}{\partial x} + \frac{\partial \mathbf{u}}{\partial y} + \frac{\mathbf{v}}{y} \right) + 2\mu \frac{\partial \mathbf{v}}{\partial y} \quad (2-9b)$$

$$\tau_{xy} = \mu \left(\frac{\partial \mathbf{u}}{\partial y} + \frac{\partial \mathbf{v}}{\partial x} \right) \quad (2-9c)$$

$$\tau_{\theta\theta} = \lambda \left(\frac{\partial \mathbf{u}}{\partial x} + \frac{\partial \mathbf{u}}{\partial y} + \frac{\mathbf{v}}{y} \right) + 2\mu \frac{\mathbf{v}}{y} \quad (2-9d)$$

The boundary conditions for the circular geometry are similar to the parallel plate geometry.

2.3 Chemistry Model

In the present work, the finite rate chemical reaction of gaseous hydrogen fuel and air is studied. The reaction is modeled by a nine species and eighteen reaction model presented in Table 2.1. Eight of the chemical species (H_2 , O_2 , H_2O , OH , H , O , HO_2 , H_2O_2) are active and the ninth (N_2) is assumed inert. The forward reaction rate of each reaction j is given by the Arrhenius law

$$k_{f_j} = A_j T^{N_j} \exp \left(-\frac{E_j}{R^0 T} \right) \quad (2-10)$$

Values for A , N and E are given in Table 2.1. Knowing the forward rate constants and using the equilibrium constant, the backward rate constants can be obtained from

$$k_{b_j} = \frac{K_{f_j}}{K_{eq_j}} \quad (2-11)$$

The equilibrium constant defined in the above equation is given by

$$K_{eq_j} = \left(\frac{1}{R^0 T} \right)^{\Delta n} \exp \left(\frac{-\Delta G_{R_j}}{R^0 T} \right) \quad (2-12)$$

where

$$\Delta G_{R_j} = \sum_{i=1}^{N_s} \gamma_{ji}'' g_i - \sum_{i=1}^{N_s} \gamma_{ji}' g_i, \quad j = 1, N_s$$

$$\frac{g_i}{R} = A_i(T - T \ln T) + \frac{B_i}{2}T^2 + \frac{C_i}{6}T^3 + \frac{D_i}{12}T^4 + \frac{E_i}{20}T^5 + F_i - G_i T$$

Once the forward and reverse reaction rates have been determined, the production rates of eight species can be found from the law of mass action. For the general chemical reaction

$$\sum_{i=1}^{N_s} \gamma'_{ji} c_i \rightleftharpoons \sum_{i=1}^{N_s} \gamma''_{ji} c_i \quad , \quad j = 1, 2, 3, \dots, N_r \quad (2-13)$$

the law of mass action states that the rate of change of concentration of species i by reaction j is given by

$$(C_i)_j = (\gamma''_{ji} - \gamma'_{ji}) \left[k_{j_f} \prod_{i=1}^{N_s} C_i^{\gamma'_{ji}} - k_{j_r} \prod_{i=1}^{N_s} C_i^{\gamma''_{ji}} \right] \quad , \quad i = 1, 2, \dots, N_s \quad (2-14)$$

The net rate of change in concentration of species i by reaction j is then found by summing the contribution from each reaction as

$$\dot{C}_i = \sum_{j=1}^{N_r} (C_i)_j \quad (2-15)$$

Finally, the production term, \dot{w} , present in the governing equation is obtained from

$$\dot{w}_i = \dot{C}_i M_i \quad (2-16)$$

where M_i is the molecular weight of the i^{th} species.

For some reacting flows, the Jacobian of the chemical system must be evaluated with respect to the field variables, (including each species). Certain chemical systems are numerically unstable when integrated with a time step comparable with the CFL condition. One remedy for this instability is treating implicitly the chemical source terms

\dot{w}_i . This technique requires the Newton linearization of the chemical source term about the previous time step and thus results in the need for evaluation of the Jacobian matrix which relates the rate of change of each source term with respect to each species. This Jacobian can be calculated either numerically or analytically, and presents no special problem once a system of reactions and species has been introduced.

Analytically, the chemical Jacobian is obtained by differentiating Eq. (2-14), and is defined by

$$\frac{\partial \dot{C}_i}{\partial C_m} = \sum_{j=1}^{N_s} (\gamma''_{ji} - \gamma'_{ji}) \left[\frac{K_{fj} \gamma'_{jm}}{C_m} \prod_{i=1}^{N_s} C_i^{\gamma'_{ji}} \frac{K_{bj} \gamma''_{jm}}{C_m} \prod_{i=1}^{N_s} C_i^{\gamma''_{ji}} \right] \quad i = 1, N_s \quad (2-17)$$

The numerical Jacobian is calculated by approximating the limit formula for the derivative as

$$\frac{\partial \dot{C}_i}{\partial C_m} = \lim_{\Delta C_m \rightarrow 0} \frac{C_i(P, T, C_1, \dots, C_{m-1}, C_m + \Delta C_m, C_{m+1}, \dots, C_{ns})}{\Delta C_m} \quad (2-18)$$

2008 INTERNATIONAL EDITION

Table 2.1. Hydrogen-Air Combustion Mechanism [22]

REACTION	A(moles)	N(cm ³)	E(calories/gm-mole)
** following reactions constitute the 18-step model **			
(1) $O_2 + H_2 \rightarrow OH + OH$	1.70×10^{13}	0	48150
(2) $O_2 + H \rightarrow OH + O$	1.42×10^{14}	0	16400
(3) $H_2 + OH \rightarrow H_2O + H$	3.16×10^7	1.8	3030
(4) $H_2 + O \rightarrow OH + H$	2.07×10^{14}	0	13750
(5) $OH + OH \rightarrow H_2O + O$	5.50×10^{13}	0	7000
(6) $H + OH + M \rightarrow H_2O + M$	2.21×10^{22}	-2.0	0
(7) $H + H + M \rightarrow H_2 + M$	6.53×10^{17}	-1.0	0
(8) $H + O_2 + M \rightarrow HO_2 + M$	3.20×10^{18}	-1.0	0
(9) $OH + HO_2 \rightarrow O_2 + H_2O$	5.00×10^{13}	0	1000
(10) $H + HO_2 \rightarrow H_2 + O_2$	2.53×10^{13}	0	700
(11) $H + HO_2 \rightarrow OH + OH$	1.99×10^{14}	0	1800
(12) $O + HO_2 \rightarrow O_2 + OH$	5.00×10^{13}	0	1000
(13) $HO_2 + HO_2 \rightarrow O_2 + H_2O_2$	1.99×10^{12}	0	0
(14) $H_2 + HO_2 \rightarrow H + H_2O_2$	3.01×10^{11}	0	18700
(15) $OH + H_2O_2 \rightarrow H_2O + HO_2$	1.02×10^{13}	0	1900
(16) $H + H_2O_2 \rightarrow H_2O + OH$	5.00×10^{14}	0	10000
(17) $O + H_2O_2 \rightarrow OH + HO_2$	1.99×10^{13}	0	5900
(18) $H_2O_2 + M \rightarrow OH + OH + M$	1.21×10^{17}	0	45500
** remaining reactions complete the 35-step model **			
(19) $O_2 + M \rightarrow O + O + M$	2.75×10^{19}	-1.0	118700
(20) $N_2 + M \rightarrow N + N + M$	3.70×10^{21}	-1.6	225000
(21) $N + O_2 \rightarrow O + NO$	6.40×10^9	1.0	6300
(22) $N + NO \rightarrow O + N_2$	1.60×10^{13}	0	0
(23) $N + OH \rightarrow H + NO$	6.30×10^{11}	0.5	0
(24) $H + NO + M \rightarrow HNO + M$	5.40×10^{15}	0	-600
(25) $H + HNO \rightarrow H_2 + NO$	4.80×10^{12}	0	0
(26) $O + HNO \rightarrow OH + NO$	5.00×10^{11}	0.5	0
(27) $OH + HNO \rightarrow H_2O + NO$	3.60×10^{13}	0	0
(28) $HO_2 + HNO \rightarrow H_2O_2 + NO$	2.00×10^{12}	0	0
(29) $HO_2 + NO \rightarrow OH + NO_2$	3.43×10^{12}	0	-260
(30) $H + NO_2 \rightarrow OH + NO$	3.50×10^{14}	0	1500
(31) $O + NO_2 \rightarrow O_2 + NO$	1.00×10^{13}	0	600
(32) $NO_2 + M \rightarrow O + NO + M$	1.16×10^{16}	0	66000
(33) $M + OH + NO \rightarrow HNO_2 + M$	5.60×10^{15}	0	-1700
(34) $M + OH + NO_2 \rightarrow HNO_3 + M$	3.00×10^{15}	0	-3800
(35) $OH + HNO_2 \rightarrow H_2O + NO_2$	1.60×10^{12}	0	0
** following reactions constitute the global 2-step model [4, 16, 18, 19] **			
(1'') $H_2 + O_2 \rightarrow 2 OH$	11.4×10^{47}	-10.0	4865
(2'') $2 OH + H_2 \rightarrow 2 H_2O$	2.50×10^{64}	-13.0	42500

2005 INTERNATIONAL BUREAU

2.4 Thermodynamic model

The specific heat of individual species, C_{p_i} , is assumed to be a linear function of temperature, i.e.,

$$C_{p_j} = a_j T + b_j \quad (2-19)$$

where a_j and b_j are constants which are obtained by curve fitting the thermodynamic data of Ref. 40. The numerical values of these constants are given in Table 2.2. The specific heat of the mixture is computed by summing specific heats of individual species weighted by species mass fraction

$$\bar{C}_p = \sum_{j=1}^m C_{p_j} f_j \quad (2-20)$$

The static enthalpy of the mixture can be expressed as

$$h = \sum_{j=1}^m \left[h_j^0 + \int_{T_0}^T C_{p_j} dT \right] f_j \quad (2-21)$$

The total enthalpy can now be evaluated as

$$H = h + 0.5 (u^2 + v^2) \quad (2-22)$$

Combining Eqs. (2-19), (2-21) and (2-22) the total enthalpy is expressed as

$$H = \sum_{j=1}^m \left[h_j^0 + \frac{a_j T^2}{2} + b_j T \right] f_j + 0.5 (u^2 + v^2) \quad (2-23)$$

where h_j^0 is the sensible enthalpy of individual species at a reference temperature $T_0 = 0$ K. The gas constant for the mixture is evaluated by a mass weighted summation over all of the species as

$$\bar{R} = \sum_{j=1}^m f_j R_j \quad (2-24)$$

The equation of state for the mixture of the gases therefore can be written as

$$P = \rho \bar{R} T \quad (2-25)$$

Table 2.2 Numerical values of various constants

Species	H(J/Kg)	a	b
O ₂	-271267.025	0.119845	947.937
H ₂ O	-13972530.24	0.43116	1857.904
H ₂	-4200188.095	2.05960	12867.46
OH	1772591.157	0.16564	1672.813
N ₂	-309483.980	0.10354	1048.389
NO	2733268.38	0.34206	1256.78

PAGE _____ INTENTIONALLY BLANK

Chapter 3

RADIATION TRANSPORT MODEL

3.1 Radiation Absorption Model

In order to include the effects of radiative interaction in a physical problem, it is essential to accurately model the absorption – emission characteristics of participating species and provide a correct radiative transfer formulation for the physical process.

Many models are available in the literature to present the absorption – emission characteristic of molecular species; a review of important models are available in [13]. Perhaps the simplest model is the gray gas model, where the absorption coefficient is assumed to be independent of the wave length. Many nongray models are also available in literature. In this study the gray gas model is utilized primarily because of its simplicity.

The total band absorptance of a vibration – rotation band is given by

$$A = \int_{-\infty}^{\infty} [1 - \exp(\kappa_{\omega} X)] d(\omega - \omega_0) \quad (3-1)$$

where κ_{ω} is the volumetric absorption coefficient, ω is the wave number, ω_0 is the wave number at the band center, $X = Py$ is the pressure path length, and the limits of integration are over the entire band pass. Various models are used to obtain the relation for A in Eq. (3-1). A convenient model to represent the average coefficient of a gray

gas is the Planck mean absorption coefficient, κ_p , which is defined as [1]

$$\kappa_p = \int_0^{\infty} \kappa_{\omega} e_{b\omega}(T) d\omega / e_b(T) \quad (3-2)$$

For a multiband gaseous system, this is expressed as

$$\kappa_p = \left[\frac{P_j}{\sigma T^4} \right] \sum_i^n e_{\omega_i}(T) S_i(T) \quad (3-3)$$

where P_j is the partial pressure of j^{th} species in a gas mixture, $e_{\omega_i}(T)$ is the Planck function evaluated at the band center, and $S_i(T)$ is the integrated band intensity of the i^{th} band.

As defined in Eq. (3-2), κ_p is a property of the medium. When κ_p is evaluated at the temperature of the gas, it is usually a mean emission coefficient and it becomes equal to the actual mean absorption coefficient only for the conditions of an equilibrium radiation field. For a nonuniform temperature field, the mean absorption coefficient which is used for the optically thin radiation is the modified Planck mean absorption coefficient, which for black bounding surfaces is defined as

$$\kappa_m(T, T_w) = \frac{\left[\int_0^{\infty} \kappa_{\omega}(T) e_{b\omega}(T_w) d\omega \right]}{e_b(T_w)} \quad (3-4)$$

Note that κ_m is a function of both the gas temperature and the wall temperature. An approximate relation between κ_p and κ_m is available for infrared radiation as [1,9]

$$\kappa_m(T, T_w) = \kappa_p(T_w) \left(\frac{T_w}{T} \right) \quad (3-5)$$

This expression is usually employed in gray gas radiative energy transfer analyses.

Several models for the mean absorption coefficient are available in the literature [1,31]. Since these models account for detailed spectral information of molecular bands, this approach of radiative formulation is referred to as the “pseudo – gray formulation”. The gray gas formulation for radiative transport is very useful in parametric studies.

There are several nongray models available in the literature to represent the absorption – emission characteristics of vibration – rotation bands. These are classified typically in four types: (1) line – by – line (LBL) models, (2) narrow band models, (3) wide band models, and (4) band model correlations. A complete discussion on usefulness and application of these models is provided in [12,13]. For many engineering applications, wide band model correlations provide quite accurate results. The most widely used wide band models are those of Edwards [5,11] and Tien and Lowder [9]. The Tien and Lowder correlation for the total band absorptance is a continuous correlation and is given by

$$\bar{A}(u, \beta) = A(u, \beta) / A_0 = \ln \{ u f(t) [(u + 2) / (u + 2f(t))] + 1 \} \quad (3-6)$$

where

$$f(t) = 2.94 [1 - \exp(-2.60t)] \quad , \quad t = \beta/2 \quad (3-7)$$

and $u = SX/A_0$ is the nondimensional path length, $\beta = 2\pi\gamma/d$ is the line structure parameter, γ is the line half width, S is the integrated band intensity, and A_0 is the band width parameter. Equation (3-6) provides accurate results for pressures higher than 0.5 atmosphere [12,13].

Spectral properties and correlation quantities for various radiation participating species are available in [5,9,11]. These are useful in gray as well as nongray radiative formulations.

3.2 Evaluation of Planck Function and Planck Mean Absorption Coefficient

The spectral emissive power of a black body at a temperature T is given by the Planck's law as [1]

$$e_b(\nu, T) = \frac{2\pi h \nu^3 n^2}{c_0^2 \left[\exp\left(\frac{h\nu}{kT}\right) - 1 \right]} \quad (3-8)$$

where

$$\begin{aligned} c_0 &= \text{speed of light in vacuum } (2.998 \times 10^{10} \text{ cm/s}) \\ h &= \text{Planck's constant } (6.625 \times 10^{-27} \text{ erg-s}) \\ k &= \text{Boltzman constant } (1.380 \times 10^{-16} \text{ erg/K}) \\ n &= \text{Index of refraction of the medium} \end{aligned} \quad (3-9)$$

ν = Frequency of radiation

The speed of light c in a medium is expressed as $c = \lambda \nu$, where λ is the wavelength; this is related to the speed of light in a vacuum by $c = c_0/n$. Thus, $\nu = c_0/(n\lambda)$. If it is assumed that n is independent of frequency, then

$$d\nu = -\left(\frac{c_0}{n\lambda^2}\right) d\lambda,$$

Since $e_{b\lambda} d\lambda = -e_{b\nu} d\nu$, Eq. (3.8) can be expressed as

$$e_b(\lambda, T) = \frac{C_1}{n^2 \lambda^5 \left[\exp\left(\frac{h\nu}{kt}\right) - 1 \right]} \quad (3-10)$$

where

$$C_1 = 2\pi h C_0^2 = (374.135577 \times 10^{-7} \text{ erg-cm}^2/\text{s})$$

$$C_2 = h C_0 / k = (143.9257246 \times 10^{-2} \text{ cm-K})$$

The index of refraction n is assumed to be independent of frequency and its value is taken to be unity. Consequently, Eq. (3-10) is applicable to most gaseous systems.

It is often convenient to express Eq. (3-10) in terms of the wave number $\omega=1/\lambda$. In order to accomplish this, one should note that $d\omega=-\lambda^{-2}d\lambda$ and $e_{b\lambda} d\lambda=-e_{b\omega}d\omega$, such that $e_{b\omega}=\lambda^2 e_{b\lambda}$. Thus Eq. (3-10) can be expressed as

$$e_b(\omega, T) = \frac{2\pi hc_0^2 \omega^3}{\exp\left(\frac{hc_0 \omega}{kT}\right) - 1} = \frac{C_1 \omega^3}{\exp\left(C_2 \frac{\omega}{T}\right) - 1} \quad (3-11)$$

From the definitions of C_1 and C_2 , and ω expressed in cm^{-1} , it is evident that the units for the Planck function in Eq. (3-11) are erg/s-cm or W/cm .

For certain applications, it is desirable to have a convenient expression for the temperature derivative of the Planck function. The quantity of frequent interest is $de_b(\omega, T)/dT$ and this can be obtained from Eq. (3-11) as

$$\frac{de_b(\omega, T)}{dT} = \frac{c_1 c_2 \omega^4 \exp\left(\frac{c_2 \omega}{T}\right)}{T^2 [\exp\left(\frac{c_2 \omega}{T}\right) - 1]^2} \quad (3-12)$$

The Planck mean absorption coefficient κ_p is defined by Eq. (3-2) and is expressed here as

$$\kappa_p = \frac{\int_0^\infty \kappa_\omega e_b(\omega, T) d\omega}{\sigma T^4} \quad (3-13)$$

It should be noted that for an isotropic medium κ_ω depends only on temperature; i.e., $\kappa_\omega = \kappa_\omega(T)$. Thus, κ_p is a property of the medium, provided that conditions of local thermodynamic equilibrium exist [1].

The integrated intensity of a band S (i.e., the integrated band absorption) is defined as

$$S(T) = \int_{\Delta\omega} \left(\frac{\kappa_\omega}{P} \right) d\omega \quad (3-14)$$

where $\Delta\omega$ represents the spectral range of the band. If the value of S is available at a given (standard) temperature T_0 , then the value of S at any other temperature is obtained from the relation

$$S(T) = \left(\frac{T_0}{T} \right) S(T_0) F(T) \quad (3-15)$$

where $F(T)$ is a function of temperature and its value depends upon the nature of the band. For fundamental vibration-rotation bands, the value of $F(T)$ is unity, i.e., $F(T)=1$. For combination and overtone bands of certain species, the values of $F(T)$ are available in the literature. However, for many species, the relationship for variation of S with temperature for combination and overtone bands are not yet available.

Within a narrow vibration-rotation band, the Planck function variation with the wavelength is small and its value may be evaluated at the band center, i.e., $e_b(\omega, T) = e_b(\omega_c, T)$. With this assumption, Eq. (3-13) is written for a multiband system as

$$\kappa_p(T) = \frac{\left\{ \sum_{i=1}^N \left[e_b(\omega, T) \int_{\Delta\omega_i} \kappa_{\omega_i} d\omega_i \right] \right\}}{\sigma T^4} \quad (3-16)$$

where N represents the number of vibration – rotation bands of a gas. By employing the definition of S given in Eq. (3-14), Eq. (3-16) is expressed for a single homogeneous gas as

$$\kappa_p(T) = \frac{P \sum_{i=1}^N [e_b(\omega_{ci}, T) S_i(T)]}{\sigma T^4} \quad (3-17)$$

where $S_i(T)$ represents the integrated band intensity of the i^{th} band of the gas. Equation (3-17) can be modified to apply to a mixture of different gases as

$$\kappa_p(T) = \frac{\sum_j P_j \left\{ \sum_{i=1}^N [e_b(\omega_{ci}, T) S_i(T)] \right\}_j}{\sigma T^4} \quad (3-18)$$

where j denotes the number of species in the mixture and P_j is the partial pressure of the j^{th} species.

3.3 Radiative Flux Equation

The equations of radiative transport are expressed generally in integro – differential form; the integration involves both the frequency spectrum and the physical coordinates. To overcome the complexity of the radiative transport equations, a tangent slab approximation was employed in [26,27]. This approximation treats the gas layer as a one dimensional slab in the evaluation of the radiative flux. The multi – dimensional equations of radiative transfer are formulated for an arbitrary geometry, and then an approximate method is used to present the formulation for gray and nongray gases. The complete formulation is available in [27], and essential relationships are provided in this section.

3.3.1 Basic Formulation

The radiative transport equations in the present study are obtained only for an absorbing – emitting medium contained within solid walls of different configuration as shown in Figs. 2.3–2.5. The general formulation of radiative transfer for the gas under the condition of local thermodynamic equilibrium is given by (see Figs. 2.3 and 3.1)

PAGE _____ INTENTIONALLY BLANK

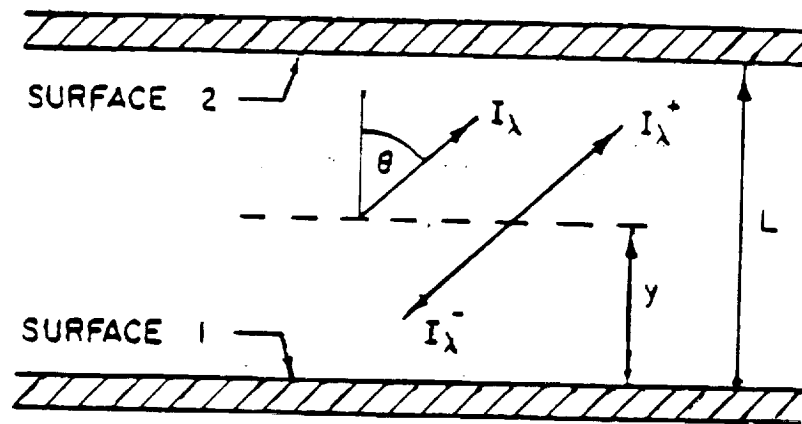


Fig. 3.1 Coordinate system for one-dimensional radiative transfer.

2168 INTERNATIONALLY ALONE

$$I_{\nu}(P) = I_{\nu}(P_w) e^{-\int_0^{r_w} \kappa_{\nu}(\xi) d\xi} + \int_0^{r_w} \kappa_{\nu}(P') I_{b\nu}(P') e^{-\int_0^{r'} \kappa_{\nu}(\xi) d\xi} dr' \quad (3-19)$$

The first term on the right hand side represents the contribution from the wall to the intensity at P, and the second term represents the contribution from the intervening gases between P and P_w. The origin of the coordinate system in Eq. (3-19) is chosen at the point P. The radiative flux at the point P in the direction of \vec{l} is

$$q_R = \int_{4\pi} \int_0^{\infty} I_{\nu} \vec{l} d\nu d\Omega \quad (3-20)$$

Substituting Eq. (3-19) into Eq. (3-20), the radiative flux is expressed as

$$\begin{aligned} q_R = & \int_{4\pi} \int_0^{\infty} I_{\nu}(P_w) e^{-\int_0^{r_w} \kappa_{\nu}(\xi) d\xi} \vec{l} d\nu d\Omega \\ & + \int_{4\pi} \int_0^{\infty} \int_0^{r_w} \kappa_{\nu}(P') I_{b\nu}(P') e^{-\int_0^{r'} \kappa_{\nu}(\xi) d\xi} \vec{l} dr' d\nu d\Omega \end{aligned} \quad (3-21)$$

The divergence of the radiative flux is formulated as

$$\nabla \cdot q_R = \int_{4\pi} \int_0^{\infty} \vec{l} \cdot \nabla I_{\nu} d\nu d\Omega \quad (3-22)$$

A beam of intensity $I_{\nu}(r, \Omega)$ travelling in the \vec{l} direction satisfies the equation of radiative heat transfer

$$\vec{l} \cdot \nabla I_{\nu} = \gamma_{\nu} I_{\nu} + \kappa_{\nu} I_{b\nu} - \beta_{\nu} I_{\nu} \quad (3-23)$$

where γ_{ν} is the scattering coefficients and $\beta_{\nu} = \gamma_{\nu} + \kappa_{\nu}$ is referred to as the extinction coefficient. For negligible scattering ($\gamma_{\nu} = 0$), Eq. (3-23) reduces to

$$\vec{l} \cdot \nabla I_\nu = \kappa_\nu (I_{b\nu} - I_\nu) \quad (3-24)$$

By combining Eq. (3-22) and Eq. (3-24), one obtains

$$\nabla \cdot \mathbf{q}_R = \int_{4\pi} \int_0^\infty \kappa_\nu (I_{b\nu} - I_\nu) d\nu d\Omega \quad (3-25)$$

Now substituting Eq. (3-19) into Eq. (3-25), the divergence of the radiative flux is expressed as

$$\begin{aligned} \nabla \cdot \mathbf{q}_R = & 4\pi \int_0^\infty \kappa_\nu(\mathbf{p}) I_{b\nu}(\mathbf{p}) d\nu - \int_{4\pi} \int_0^\infty \kappa_\nu(\mathbf{p}) I_\nu(\mathbf{p}_w) e^{-\int_0^{r_w} \kappa_\nu(\xi) d\xi} \\ & - \int_{4\pi} \int_0^\infty \int_0^{r_w} \kappa_\nu(\mathbf{p}) \kappa_\nu(\mathbf{p}') I_{b\nu}(\mathbf{p}') e^{-\int_0^{r'} \kappa_\nu(\xi) d\xi} d\mathbf{r}' d\nu d\Omega \end{aligned} \quad (3-26)$$

Equations (3-21) and (3-26) are used to obtain various approximate forms for the radiative flux and its divergence.

3.3.2 Gray Formulation

In the previous section, it was observed that the radiative flux terms are represented by an integral equations. Solving these equations is extremely time consuming because of the complexity of integration over space and frequency. Therefore, a pseudo – gray model is selected for efficient parametric studies. To express the radiative flux for a gray medium, one may assume that κ_ν is independent of the frequency. This is rarely a physically realistic approximation; but it serves as an initial stepping stone towards nongray analyses. Therefore, Eq. (3-21) and Eq. (3-26) for a gray medium are written as

$$q_R = \int_{4\pi} I(P_w) e^{-\int_0^{r_w} \kappa(\xi) d\xi} d\Omega + \int_{4\pi} \int_0^{r_w} \kappa(p') I_b(p') e^{-\int_0^{r_w} \kappa(\xi) d\xi} dr' d\Omega \quad (3-27)$$

and

$$\begin{aligned} \nabla \cdot q_R = & 4\pi \kappa(p) I_b(p) - \int_{4\pi} \kappa(p) I(P_w) e^{-\int_0^{r_w} \kappa(\xi) d\xi} d\Omega \\ & - \int_{4\pi} \int_0^{r_w} \kappa(p) \kappa(p') I_b(p') e^{-\int_0^{r'} \kappa(\xi) d\xi} dr' d\Omega \end{aligned} \quad (3-28)$$

To solve the radiative flux terms for the gray medium, Eqs. (3-27) and (3-28) can be transformed into Cartesian coordinates, and then any one of the standard integration techniques to evaluate the radiative flux term are applied. It is more convenient and efficient to convert the equations to a set of ordinary differential equations (ODE). For the present case, differentiating Eq. (3-28) by using the Leibnitz rule results in

$$\begin{aligned} \nabla^2 q_R = & 4\kappa(p) \frac{\partial e_b}{\partial r} + \int_{4\pi} \kappa^2(p) I(P_w) e^{-\int_0^{r_w} \kappa(\xi) d\xi} d\Omega \\ & + \int_{4\pi} \int_0^{r_w} \kappa(p) \kappa(p') I_b(p') e^{-\int_0^{r'} \kappa(\xi) d\xi} dr' d\Omega \end{aligned} \quad (3-29)$$

A substitution of Eq. (3-29) into Eq. (3-27) gives a second order nonhomogenous ordinary differential equation for one dimensional radiative transfer as

$$\frac{d^2 q_R}{dr^2} - \kappa^2(P) q_R = 4\kappa(P) \frac{de_b}{dr} \quad (3-30)$$

It should be pointed out that if the tangent slab approximation is employed, then the method of exponential kernel approximation is used to convert the equations to a set of ODE's. The transformation of Eq. (3-28) into a differential equation by exponential kernel approximation is shown in Appendix C. The result is of the same form as Eq. (3-30), but the coefficients are different; i.e.,

$$\frac{d^2 q_R}{dr^2} = \frac{9}{4} \kappa^2(P) q_R + 3\kappa(P) \frac{de_b}{dr} \quad (3-31)$$

Equations (3-30) and (3-31) differ in the coefficients due to the employment of the exponential kernel approximation in the second approach. These equations require two boundary conditions. For nonblack diffuse surfaces, the boundary conditions corresponding to Eqs. (3-30) and (3-31) are given in [12].

For black walls and for $T_1 = T_2$, the boundary conditions for Eq. (3-31) become

$$q_R\left(\frac{1}{2}\right) = 0, \quad \frac{3}{2} q_R(0) = \frac{1}{\tau_0} \left(\frac{dq_R}{d\xi} \right)_{\xi=0} \quad (3-32)$$

where

$$\tau_0 = \kappa_P L, \quad \xi = \frac{y}{L} \quad (3-35)$$

For a black circular tube, the spectral radiative heat flux in the radial direction is given by the expression [17]

$$\begin{aligned}
q_R(r) = & \frac{4}{\pi} \int_0^{\frac{\pi}{2}} \left\{ \int_{r \sin \gamma}^r F_\omega(r') k_\omega a \exp \left[-\frac{bk_\omega}{\cos \gamma} (r - r') \right] dr' \right. \\
& - \int_r^{r_0} F_\omega(r') k_\omega a \exp \left[-\frac{bk_\omega}{\cos \gamma} (r - r') \right] dr' \\
& \left. + \int_{r \sin \gamma}^{r_0} F_\omega(r') k_\omega a \exp \left[-\frac{bk_\omega}{\cos \gamma} (r + r' - 2r \sin \gamma) \right] dr' \right\} d\gamma
\end{aligned} \tag{3-33}$$

where $F_\omega(r') = e_\omega(r') - e_\omega(T_w)$ and constants a and b have values of unity and $5/4$, respectively. A combination of Eq. (3-20) and (3-34) provides a convenient expression for the total radiative flux for nongray analyses.

For a gray medium, the expression for the total radiative flux can be obtained for a circular tube from differential approximation as [1,17]

$$\frac{d}{dr} \left[\frac{1}{r} \frac{d}{dr} (r q_R) \right] - \frac{9}{4} k_p^2 q_R = 3\sigma k_p \frac{dT^4}{dr} \tag{3-34}$$

The boundary condition for this equation is found to be

$$\frac{3}{2} q_R(1) = -\frac{1}{\tau_0} \left[\frac{1}{\xi} \frac{d}{d\xi} (\xi q_R) \right]_{\xi=1}, \quad q_R(0) = 0, \tag{3-35}$$

where

$$\tau_0 = \kappa_p r_0, \quad \xi = \frac{r}{r_0} \tag{3-39}$$

With certain modifications, the radiative flux equations presented in this section can also be used to investigate the radiative interactions in the flow direction. The procedure for doing this is provided in [27].

PAGE _____ INTERNATIONAL BOUND

Chapter 4

METHOD OF SOLUTION

The grid generation technique and solution procedures for the governing equations using the unsplit MacCormack [43] technique are briefly described in this chapter

4.1 Grid Generation

Grids are generated using an algebraic grid generation technique developed by Smith and Weigel [42]. From the computational point of view, it is desirable to have a uniform rectangular grid enclosed in a cube, where the exterior of the grid represents the physical boundaries. To have such grids, the body – fitted coordinate system is transformed linearly from the physical domain (x, y) to the computational domain (ξ, η) as follows :

Lower Boundary

$$\begin{aligned} X_1 &= X(\xi, 0) \\ Y_1 &= Y(\xi, 0) \end{aligned} \tag{4-1}$$

Upper Boundary

$$\begin{aligned} X_2 &= X(\xi, 1) \\ Y_2 &= Y(\xi, 1) \end{aligned} \tag{4-2}$$

Between the Boundaries

$$\begin{aligned} X &= X(\xi, 1)\eta + X(\xi, 0)(1 - \eta) \\ Y &= Y(\xi, 1)\eta + Y(\xi, 0)(1 - \eta) \end{aligned} \tag{4-3}$$

where

$$0 \leq \xi \leq 1 ; 0 \leq \eta \leq 1$$

The grid should be concentrated in the region of high gradients to accurately predict the solution. Therefore, more grid points are required near the solid boundaries. The concentration of the grid in the η direction can be accomplished by

$$\bar{\eta} = \frac{(\beta_y + 1) - (\beta_y - 1) \exp[-c(\eta - 1 + \alpha)/(1 - \alpha)]}{(2\alpha + 1) \{1 + \exp[c(\eta - 1 + \alpha)/(1 - \alpha)]\}} \quad (4-4)$$

where

$$c = \ln \left(\frac{\beta_y + 1}{\beta_y - 1} \right)$$

If α is equal to zero, the compression takes place only near the lower wall ($\eta = 0$), and if α is set equal to one half, the compression takes place near both the walls. The term β_y has a value between one and two, and as it gets closer to one, the grid becomes more concentrated near the walls. Employing this concentration, Eq. (4-3) is written in terms of η as

$$\begin{aligned} X &= X(\xi, 1) \bar{\eta} + X(\xi, 0) (1 - \bar{\eta}) \\ Y &= Y(\xi, 1) \bar{\eta} + Y(\xi, 0) (1 - \bar{\eta}) \end{aligned} \quad (4-5)$$

where

$$0 \leq \bar{\eta} \leq 1$$

It should be noted that the grid is concentrated near solid walls in the normal direction to resolve the boundary layer. Uniform spacing is used in the streamwise direction.

4.2 Solution of the Governing Equations

The MacCormack's finite-difference scheme is used to discretize and solve the governing equations. As such, Eq. (2-1) is expressed in the computational domain as

$$\frac{\partial \hat{U}}{\partial t} + \frac{\partial \hat{F}}{\partial \xi} + \frac{\partial \hat{G}}{\partial \eta} + \hat{H} = 0 \quad (4-6)$$

where

$$\hat{U} = UJ$$

$$\hat{F} = FY_\eta - GX_\eta$$

$$\hat{G} = GX_\xi - FY_\xi$$

$$\hat{H} = HJ$$

$$J = X_\xi Y_\eta - Y_\xi X_\eta$$

Equation (4-6) is discretized temporally and written as

$$\hat{U}^{n+1} = \hat{U}^n - \Delta t \left[\frac{\partial \hat{F}^n}{\partial \xi} + \frac{\partial \hat{G}^n}{\partial \eta} + \hat{H}^{n+1} \right] \quad (4-7)$$

The source term H^{n+1} must be linearized next. It is expanded in a Taylor series in time to give

$$\hat{H}^{n+1} = \hat{H}^n + \Delta t \frac{\partial \hat{H}}{\partial t} + o(\Delta t)^2$$

or

$$\hat{H}^{n+1} = \hat{H}^n + \Delta t \frac{\partial \hat{H}}{\partial \hat{U}} \left(\frac{\hat{U}^{n+1}}{\Delta t} - \frac{\hat{U}^n}{\Delta t} \right) \quad (4-8)$$

A substitution of Eq. (4-8) into (4-7) gives the temporally discrete equation in delta form as

$$\left[I + \Delta t \frac{\partial \hat{H}}{\partial \hat{U}} \right] \Delta \hat{U}^{n+1} = -\Delta t \left[\frac{\partial \hat{F}}{\partial \xi} + \frac{\partial \hat{G}}{\partial \eta} + \hat{H} \right]^n \quad (4-9)$$

where $U^{n+1} - U^n$ is expressed as ΔU^{n+1} , $\left[\frac{\partial \hat{H}}{\partial \hat{U}} \right]$, is the Jacobian matrix of H and $[I]$ is the identity matrix. The terms of the Jacobian matrix are detailed in Appendix D.

Once the temporal discretization used to construct Eq. (4-9) has been performed, the resulting system is spatially differenced using the unsplit MacCormack predictor – corrector scheme. This results in a spatially and temporally discrete, simultaneous system of equations at each grid point. Each simultaneous system is solved using the Householder technique [45] in combination with MacCormack technique, which is then used to advance the equation in time. The modified MacCormack scheme then becomes

$$\left[\mathbf{I} + \Delta t \left(\frac{\partial \hat{\mathbf{H}}}{\partial \hat{\mathbf{U}}} \right)_{ij}^n \right] \Delta \hat{\mathbf{U}}_{ij}^{n+1} = -\Delta t \left[\frac{\partial \hat{\mathbf{F}}}{\partial \xi} + \frac{\partial \hat{\mathbf{G}}}{\partial \eta} + \hat{\mathbf{H}} \right]_{ij}^n \quad (4-10a)$$

$$\hat{\mathbf{U}}_{ij}^{n+1} = \hat{\mathbf{U}}_{ij}^n + \Delta \hat{\mathbf{U}}_{ij}^{n+1} \quad (4-10b)$$

$$\left[\mathbf{I} + \Delta t \left(\frac{\partial \hat{\mathbf{H}}}{\partial \hat{\mathbf{U}}} \right)_{ij}^n \right] \Delta \hat{\mathbf{U}}_{ij}^{n+1} = -\Delta t \left[\frac{\partial \hat{\mathbf{F}}}{\partial \xi} + \frac{\partial \hat{\mathbf{G}}}{\partial \eta} + \hat{\mathbf{H}} \right]_{ij}^{n+1} \quad (4-10c)$$

$$\hat{\mathbf{U}}_{ij}^{n+1} = \hat{\mathbf{U}}_{ij}^n + 0.5 \left[\Delta \hat{\mathbf{U}}_{ij}^{n+1} + \hat{\mathbf{U}}_{ij}^{n+1} \right] \quad (4-10d)$$

Equations (4-10) are used to advance the solution from time n to $n + 1$, and iteration process is continued until a desired integration time has been reached .

The details of gray gas as well as nongray radiative flux formulations and solution procedure are available in [1]. For the gray gas model, the governing equations are discretized using a central difference scheme. The discretization of Eqs. (3-31) and (3-34) results respectively in

$$\left(\frac{2}{A_j} \right) q_{j-1} - \left[\frac{2}{B_j} \left(\frac{1}{C_j} + \frac{1}{\Delta y_j} \right) + \frac{9}{4} \kappa_j^2 \right] q_j + \left(\frac{2}{A_j \beta_j} \right) q_{j+1} = \text{RHS} \quad (4-11)$$

$$\left(\frac{2}{A_j} + \frac{1}{2y_j C_j} \right) q_{j+1} - \left[\frac{2}{B_j} \left(\frac{1}{C_j} + \frac{1}{\Delta y_j} \right) + \frac{9}{4} \kappa_j^2 + \frac{1}{y^2} + \frac{1}{2y_j C_j} - \frac{1}{2y_j \Delta y_j} \right] q_j + \left(\frac{2}{A_j \beta_j} - \frac{2}{2y_j \Delta y_j} \right) q_{j-1} = \text{RHS} \quad (4-12)$$

where

$$A_j = \Delta y_j^2 (1 + \beta_j), \quad B_j = \Delta y_j (1 + \beta_j), \quad C_j = \beta_j \Delta y_j,$$

$$\text{RHS} = 1.5 \kappa_j \left[\frac{e_{j+1} - e_j}{\beta_j \Delta y_j} + \frac{e_j - e_{j-1}}{\Delta y_j} \right], \quad \Delta y_j = y_j - y_{j-1}, \quad \beta_j = \frac{y_{j+1} - y_j}{y_j - y_{j-1}}$$

Equations (4-11) and (4-12) along with boundary conditions given by Eqs. (3-32a) and (3-32b) form tridiagonal systems of equations which can be solved efficiently by the Thomas algorithm.

In the nongray gas formulation, the divergence of the radiative flux is evaluated using a central difference scheme and is treated as radiative source term in the energy equation. Since the radiative flux terms involves integral formulation, unlike other flux terms which are only in a differential form, it is uncoupled and treated separately.

4.3 Physical Conditions and Data Source

The physical conditions for which specific flowfield analysis and computations are needed are discussed in [21-28]. In this work selected parametric studies have been conducted for certain flow and physical conditions. Radiation participating species which are considered are H₂O, OH and NO. Radiative properties of these species are available in [5,9,11-13]. Different amounts of these gases, in combination with air, are considered for parametric studies. Essential data for the chemistry model employed are obtained from Refs. 28 and 29 and these are provided in Table 2.1.

For basic studies, the physical dimensions considered for the channel are $L=3$ cm and $L_x=10$ cm, and for the circular tube they are $L=D=3$ cm and $L_x=10$ cm. Reacting flow calculations are obtained for a 10^0 compression nozzle.

As discussed in Chap. 2, the governing equations Eq. (2-1) requires boundary conditions along all four boundaries. For the cases considered in this study, the inflow boundary is always supersonic, so the velocity and species are specified there. The upper and lower surfaces are solid boundaries, so the no slip boundary conditions ($u=0$, $v=0$) are used to specify the velocity components. In addition, along these solid boundaries the temperature gradient is held constant for one case and for another case the temperature is specified. The outflow boundary is also supersonic, and therefore velocity components, static temperature and pressure, and species concentration are extrapolated.

The governing equations also require initial conditions. The equations are initialized by setting values of the velocity, static temperature, and pressure, and species concentration through the domain to the values at the inflow boundary. Having specified all required initial and boundary data, the equations are marched in time from the initial time to some final specified time level.

Chapter 5

RESULTS AND DISCUSSION

Based on the theory and computational procedure described in the previous sections, an existing code was modified to solve the two-dimensional Navier-Stokes equations for radiating supersonic laminar flow between two parallel black plates. A similar code was developed for radiating supersonic flows in a circular tube. In most cases, the radiative interaction was considered only in the normal direction. Extensive results have been obtained for pure H_2O , OH , and NO as homogenous participating species, and for different mixture of these species with air.

As mentioned earlier, the Planck mean absorption coefficient κ_p (or κ_m) is considered to be an optically thin radiation absorption coefficient, although it has been used in other optical ranges as well [1,9]. The appropriate absorption coefficient for the optically thick radiation is the Rosseland mean absorption coefficient κ_R . It has been noted in [1] that if the medium is gray, then $\kappa_p = \kappa_R = \kappa$; otherwise $\kappa_p > \kappa_R$. Thus use of κ_p (or κ_m) in pseudo-gray gas formation will provide maximum influence of radiative interaction. The κ_p values for H_2O , OH , and NO have been calculated from Eq. (3-17) by employing radiative properties available in [5,9,11], and these are illustrated in Figs. 5.1 and 5.2. Figure 5.1 shows the results of 100% homogenous species, whereas results in Fig. 5.2 are for different mixtures. The results provide indication of the radiative ability of different species at a given temperature. Values of κ_p for other species are available in [1,9].

PAGE _____ INFORMATIONAL PLANS

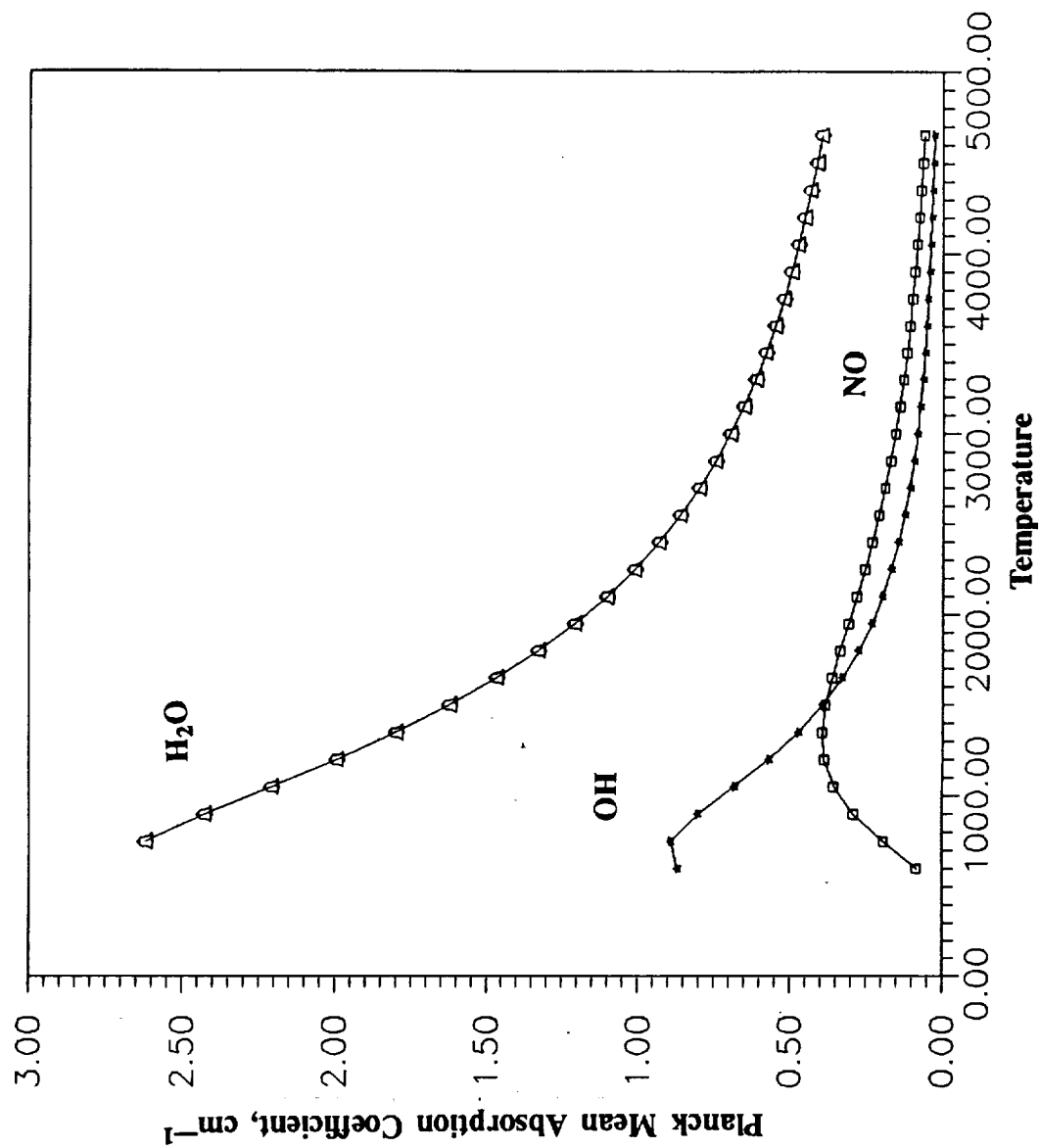


Fig. 5.1 Variation of Planck mean absorption coefficient for H₂O, NO and OH.

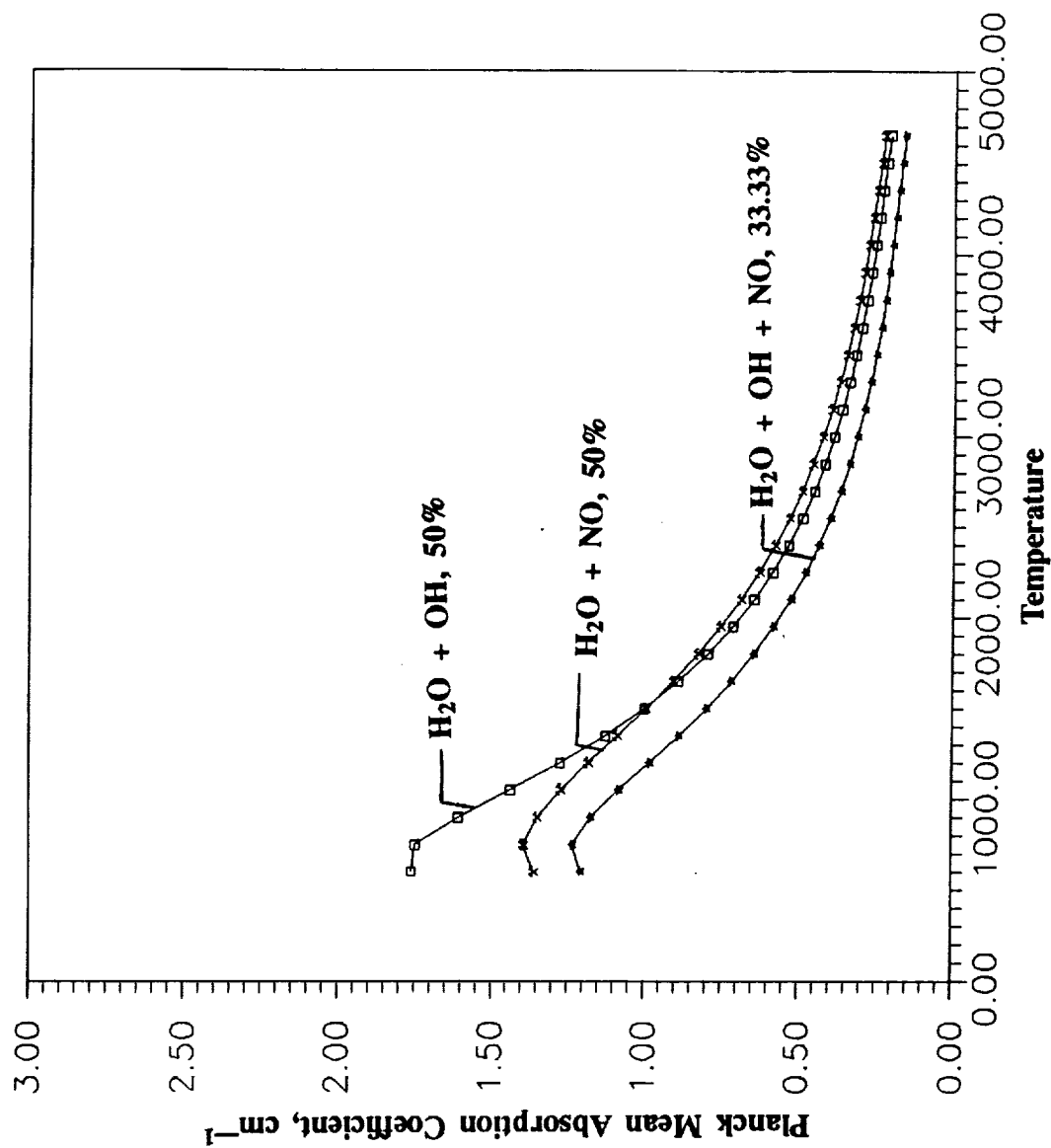


Fig. 5.2 Variation of the Planck mean absorption coefficient for different mixtures of H₂O, NO and OH.

For basic understanding of supersonic entrance region flow, illustrative results for flowfield variables and heat transfer have been obtained for nonreacting flows between two parallel plates and within a circular tube. The physical dimensions considered for the channel are $L=3$ cm and $L_x=10$ cm. In most cases, the inflow conditions considered are $P_\infty=1$ atm, $T_\infty=1,700$ K, $U_\infty=2574$ m/s ($M_\infty=3.0$) with varying amounts of radiation participating species in combination with air. The surface temperature varies with x , and is determined at the first grid point normal to the surface. Certain variations in physical and inflow conditions are also considered for parametric studies. The chemical reactions are not considered in obtaining the results, and radiative flux results are presented only for the normal direction.

Results for the radiative flux as a function of nondimensional position, are illustrated for $P = 1$ atm. The results presented in Fig. 5.3 for different water vapor concentrations indicate that radiative interaction increases slowly with an increase in the amount of the gas. It is noted that the radiation flux is approximately zero in the center of the channel ($y = 1.5$ cm) and is significantly higher towards the top and bottom of the plates. This however would be expected because of the symmetry of the problem and the relatively high temperatures near the boundaries. The results for 50% H_2O are presented in Fig. 5.4 for two different pressures ($P = 1$ and 3 atm) and x -locations ($x = 5$ and 10 cm). It is noted that the increase in pressure has dramatic effects on the radiative interaction.

For a mixture of 50% H_2O in air, the conduction and radiation heat transfer results are compared in Fig. 5.5, for $P = 3$ atm and for two different x -locations ($x = 5$ and 10cm). The results demonstrate that the conduction heat transfer is restricted to the region near the boundaries, and does not change significantly from one x -location to another. The radiative interaction, however, is seen to be important everywhere in the

PAGE _____ INTENTIONALLY BLANK

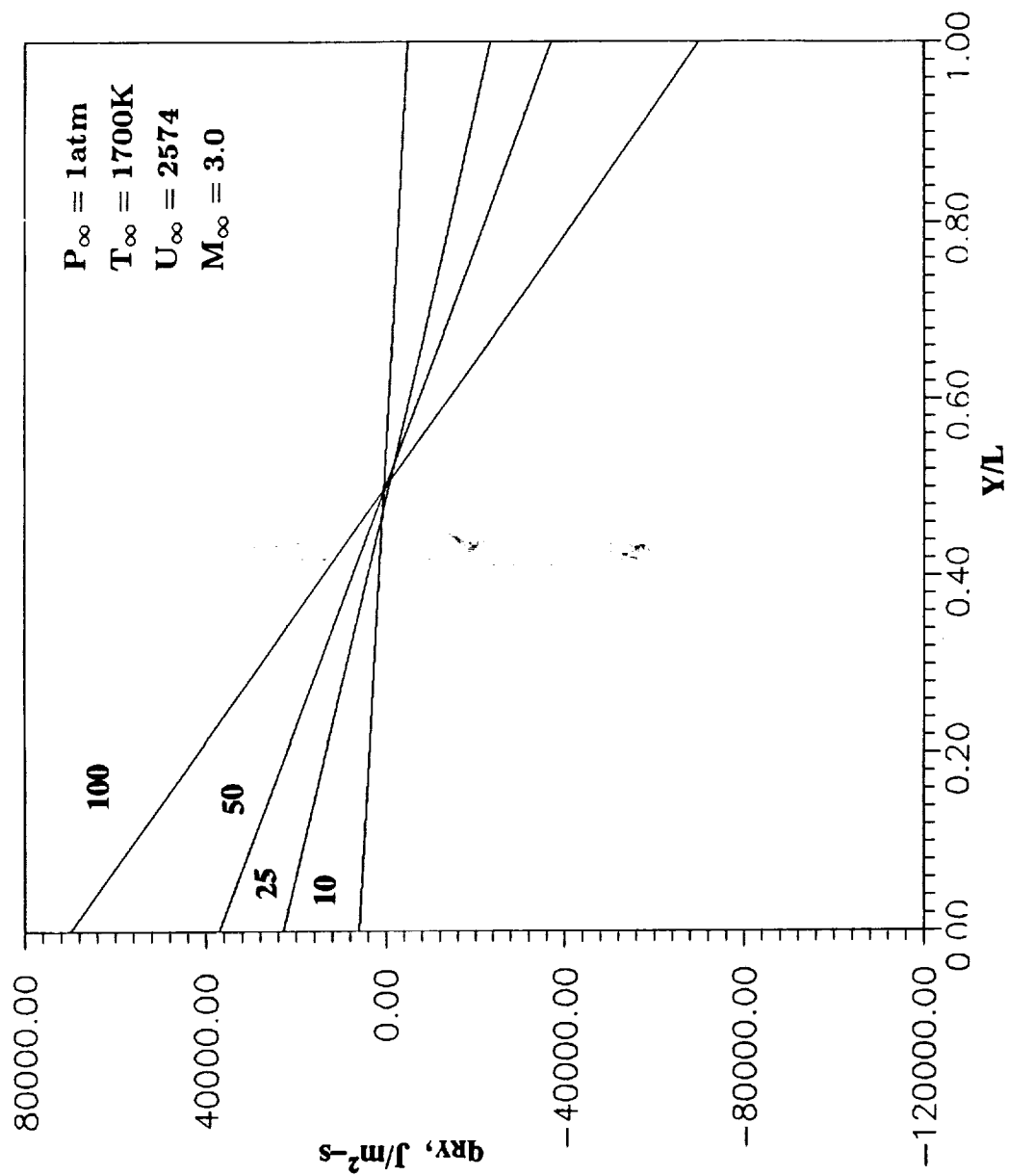


Fig. 5.3 Radiative flux vs y at the channel exit $M_{\infty} = 3.0$.

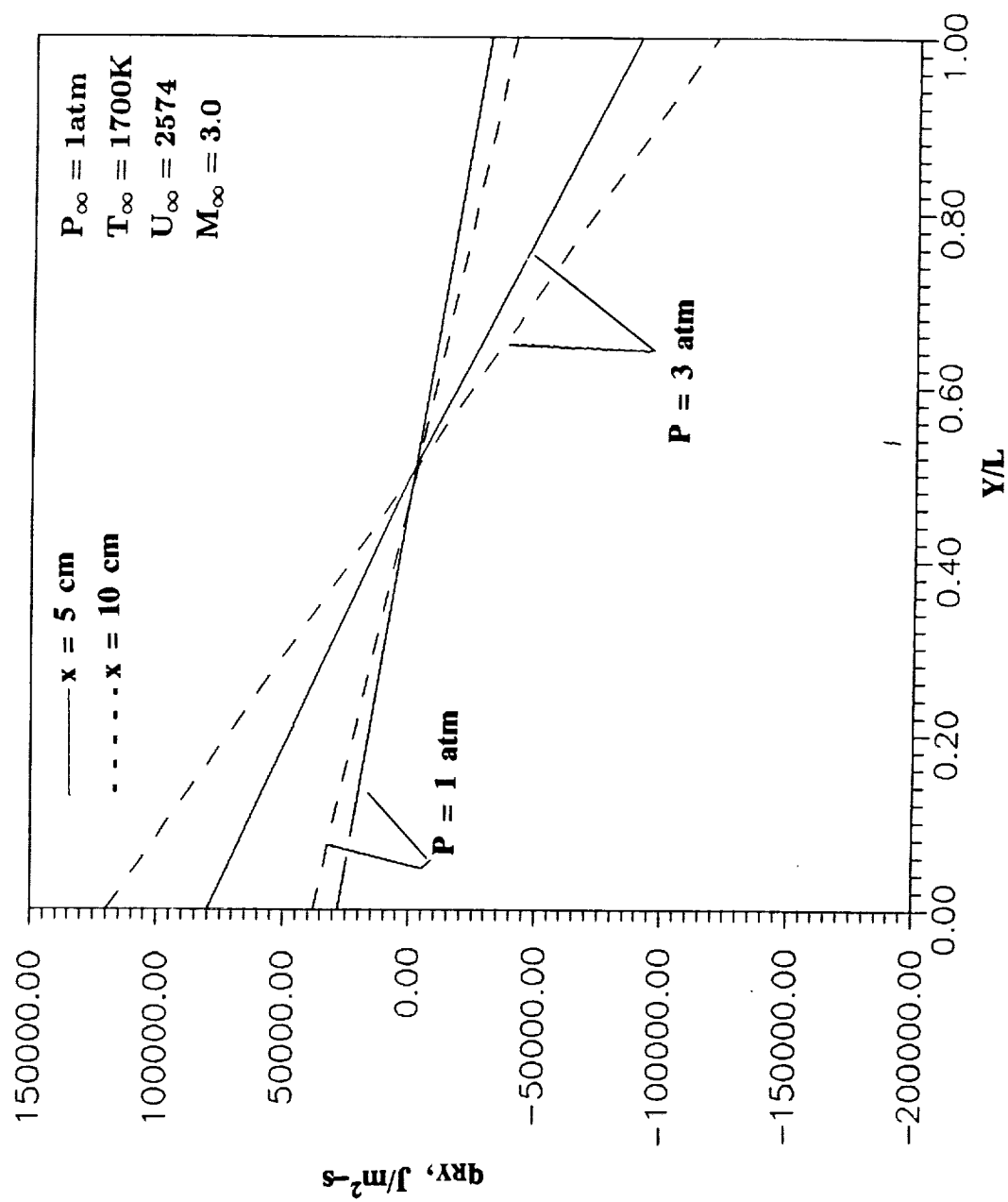


Fig. 5.4 Radiative flux vs y for $P = 1 \text{ atm}$ and 3 atm , $x = 5 \text{ cm}$ and 10 cm , 50% H_2O , $M_{\infty} = 3.0$.

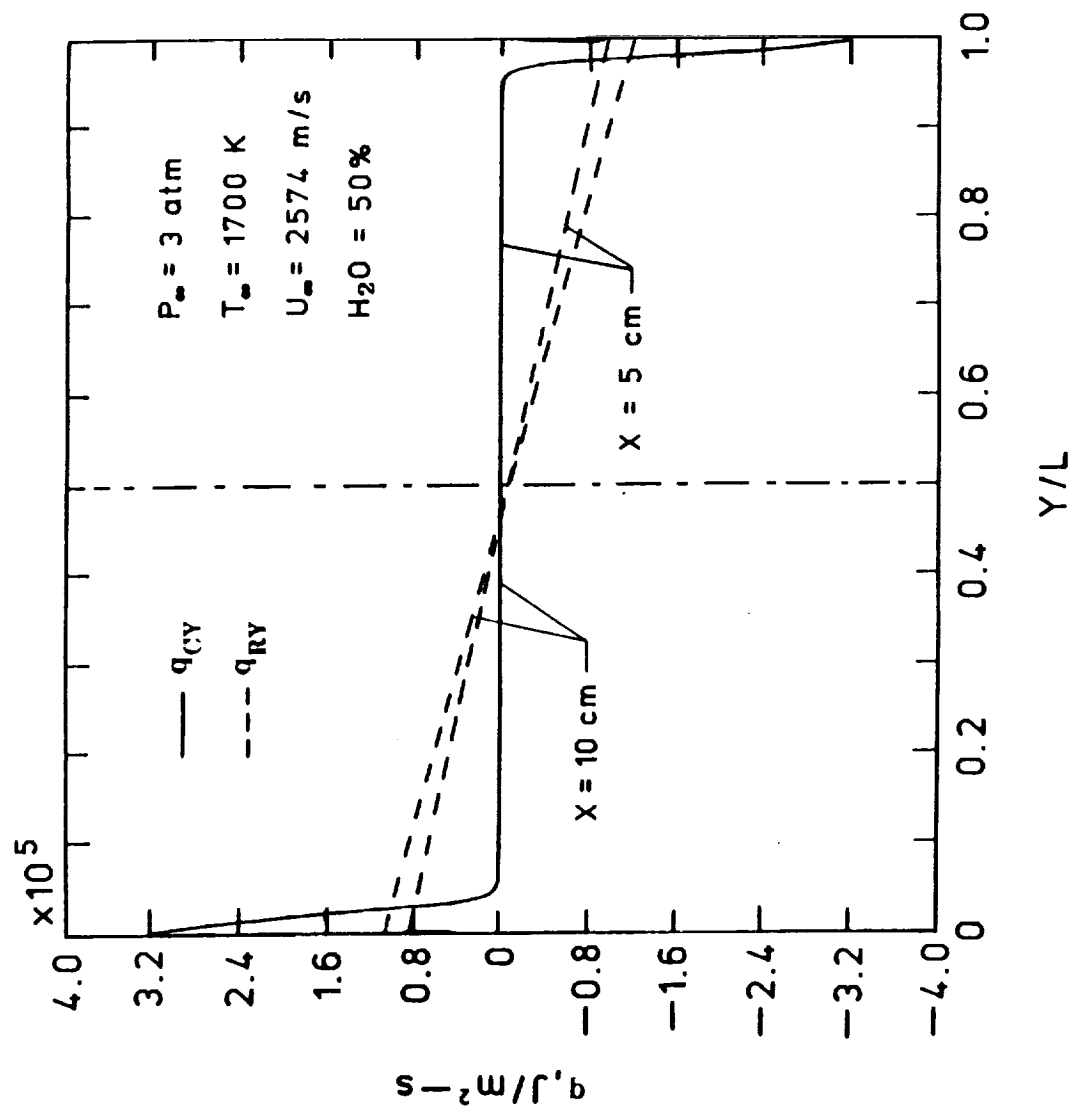


Fig. 5.5 Radiative and conductive fluxes vs. y for $P = 3 \text{ atm}$, $x = 5$ and 10 cm , $50\% \text{ H}_2\text{O}$, $M_\infty = 3.0$.

~~THIS~~ INTENTIONALLY BLANK

channel, and this can have a significant influence on the entire flow field.

Comparative results for 100% homogeneous species of H_2O , NO , and OH are illustrated in Fig. 5.6, at the exit plane ($x = 10$ cm). As would be expected, the radiative contribution of H_2O (with five bands) is significantly higher than NO and OH . Only the fundamental bands of NO and OH are considered in this study, and it is noted that NO is a better radiating gas in comparison to OH .

For a mixture of 25% H_2O in air, radiative flux for two different plate spacings ($L = 3$ and 6 cm) are illustrated in Fig. 5.7 for two x -locations ($x = 5$ and 10 cm). The rate of radiative transfer is a strong function of the amount of the participating species and the pressure path length PL . Consequently, the results for the larger plate spacing indicate significantly higher radiative interactions.

The effect of increased Mach number on the radiative transfer is illustrated in Fig. 5.8 for pure H_2O and for a mixture of 50% H_2O in air. The results shown are for the exit plane ($x = 10$ cm). At higher Mach number, the boundary layer is relatively thinner and the temperature in the boundary layer is significantly higher. This in turn results in a higher rate of radiative transfer.

For a mixture of 50% H_2O in air, comparative results for the parallel plate channel and the circular tube are presented in Fig. 5.9, for two x -locations ($x = 5$ and 10 cm). The results for the circular tube exhibit the same trend as for the parallel plate geometry. Since the circular geometry provides additional degrees of freedom for radiative transfer, the rate of radiative transfer is higher for the tube.

Figures 5.10 and 5.11 show the velocity and temperature profiles across the channel at three different x -locations ($x = 2, 5$ and 10 cm). It is seen that the flow attains a near steady-state value towards the exit of the channel. It is also noted that due to the

~~SECRET~~ INTENTIONALLY BLANK

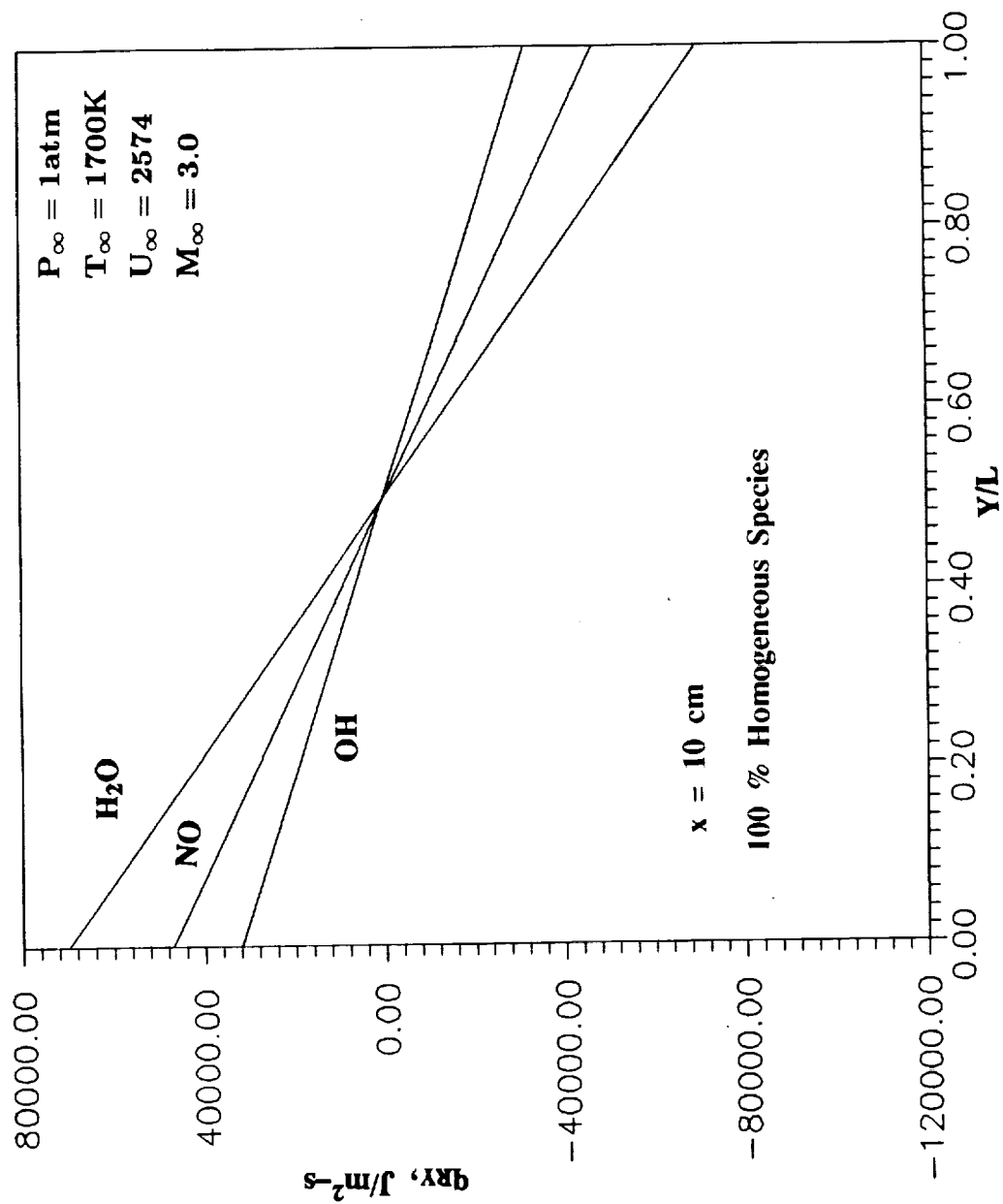


Fig. 5.6 Radiative flux vs y for H_2O , NO and OH , $P = 1 \text{ atm}$ $M_{\infty} = 3.0$.

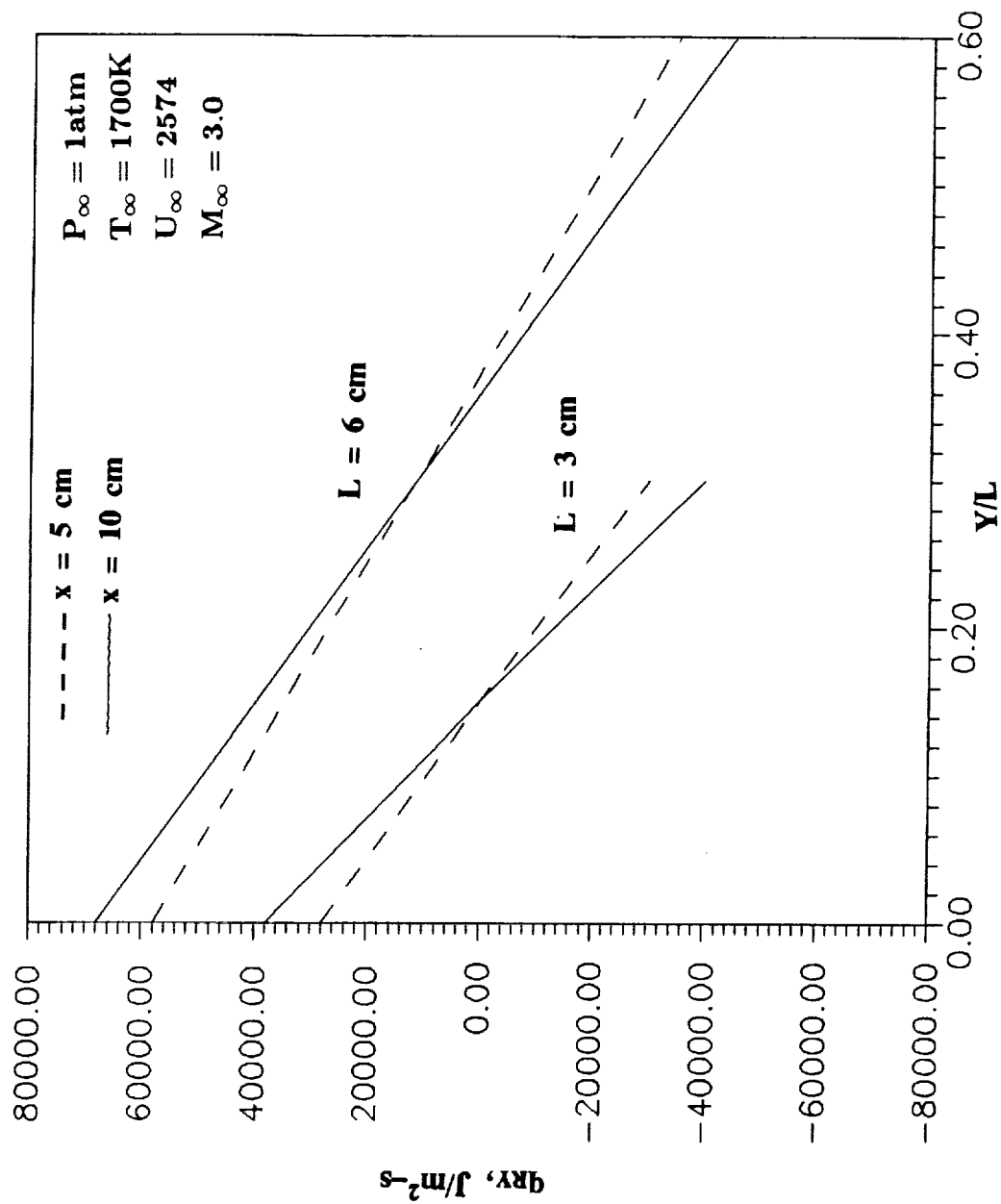


Fig. 5.7 Radiative flux vs y for two different plate spacing ($L = 3$ and 6 cm) at $x = 5$ and 10 cm , $M_{\infty} = 3.0$.

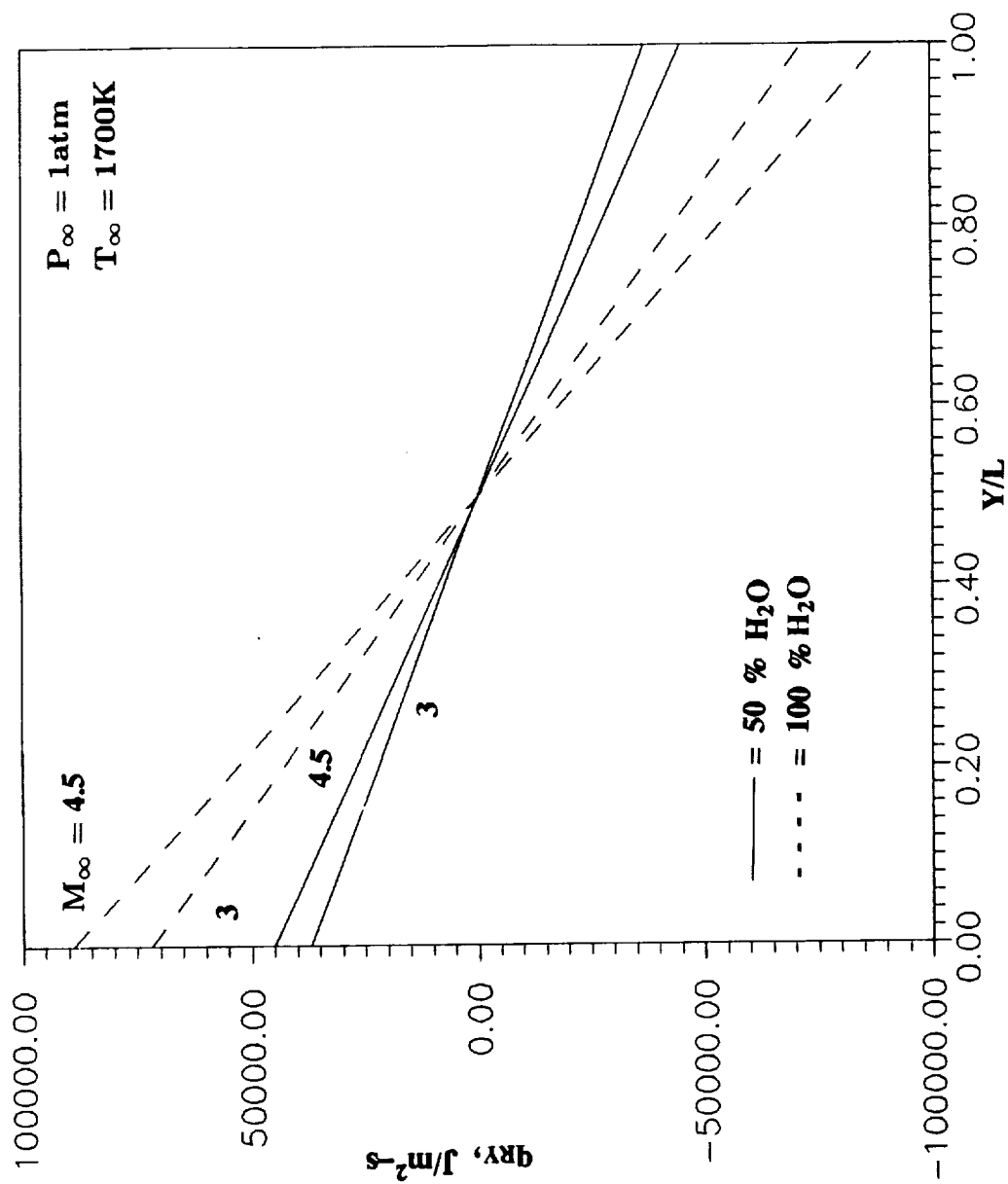


Fig. 5.8 Radiative flux vs y for 50 % and 100 % H_2O , $x = 10 \text{ cm}$, $M_{\infty} = 3.0, 4.5$.

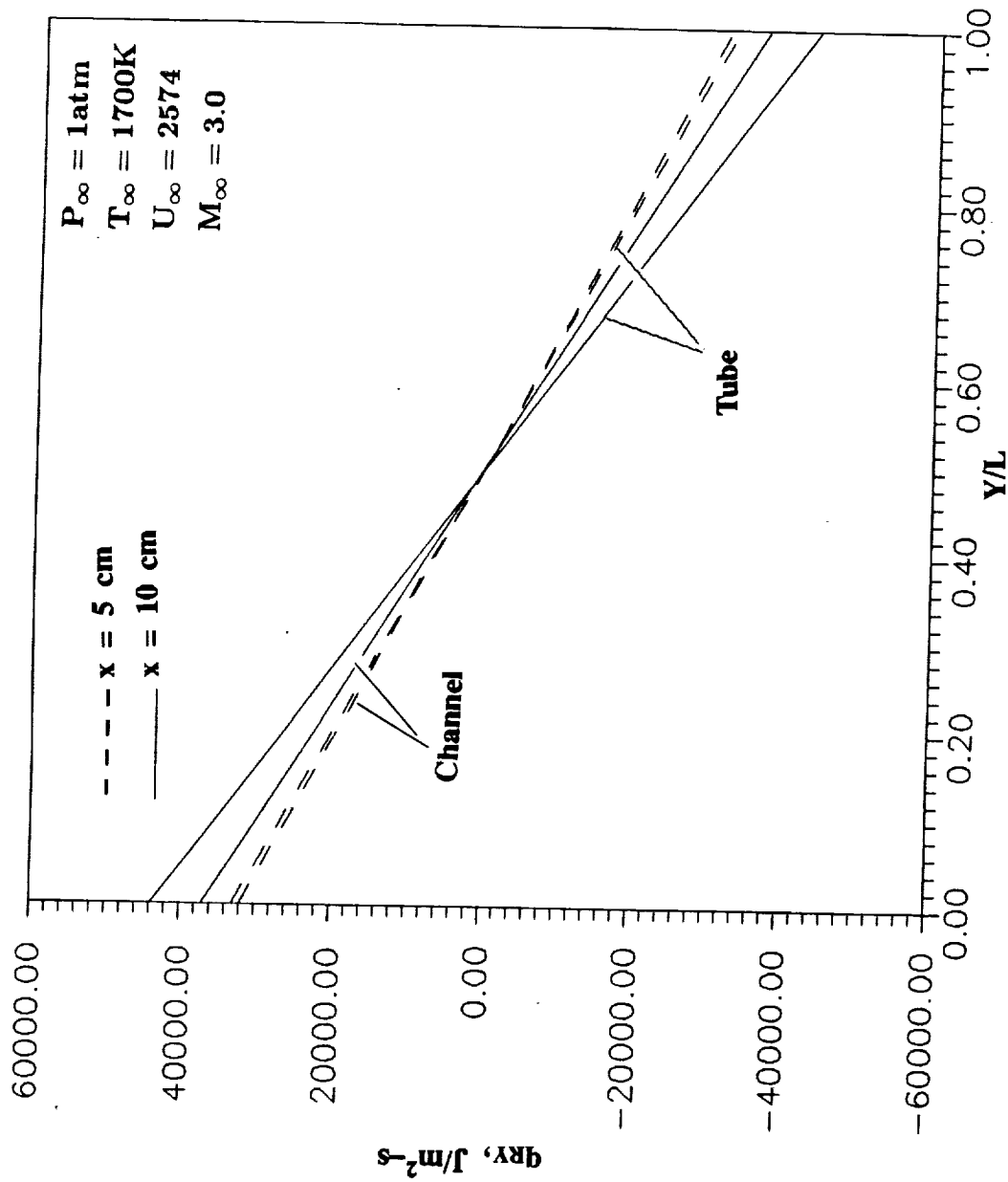


Fig. 5.9 Radiative flux vs y for channel and tube ($L = D = 3 \text{ cm}$) at $x = 5$ and 10 cm , $50 \% \text{ H}_2\text{O}$, $M_{\infty} = 3.0$.

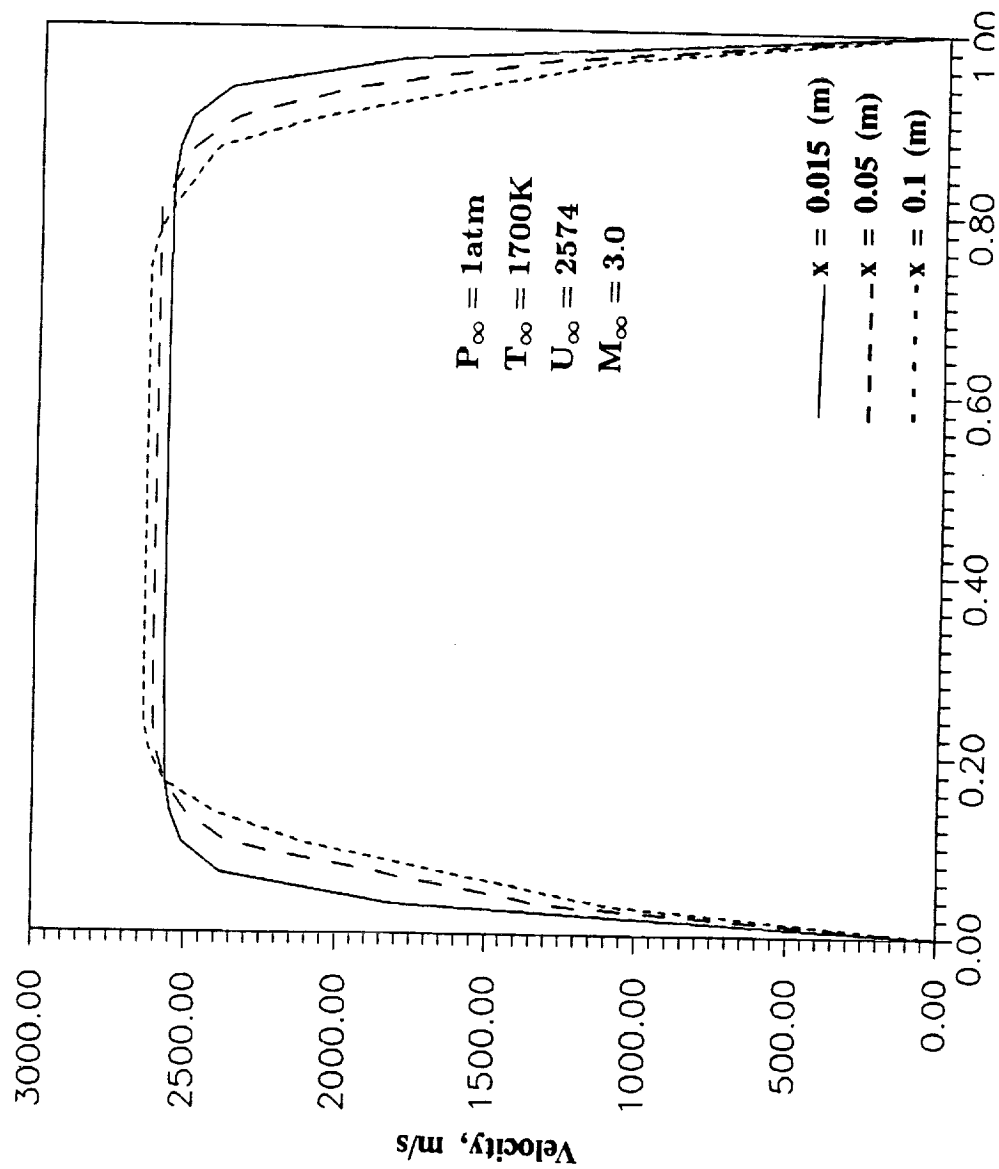


Fig. 5.10 Variation of axial velocity across the channel at various x locations.

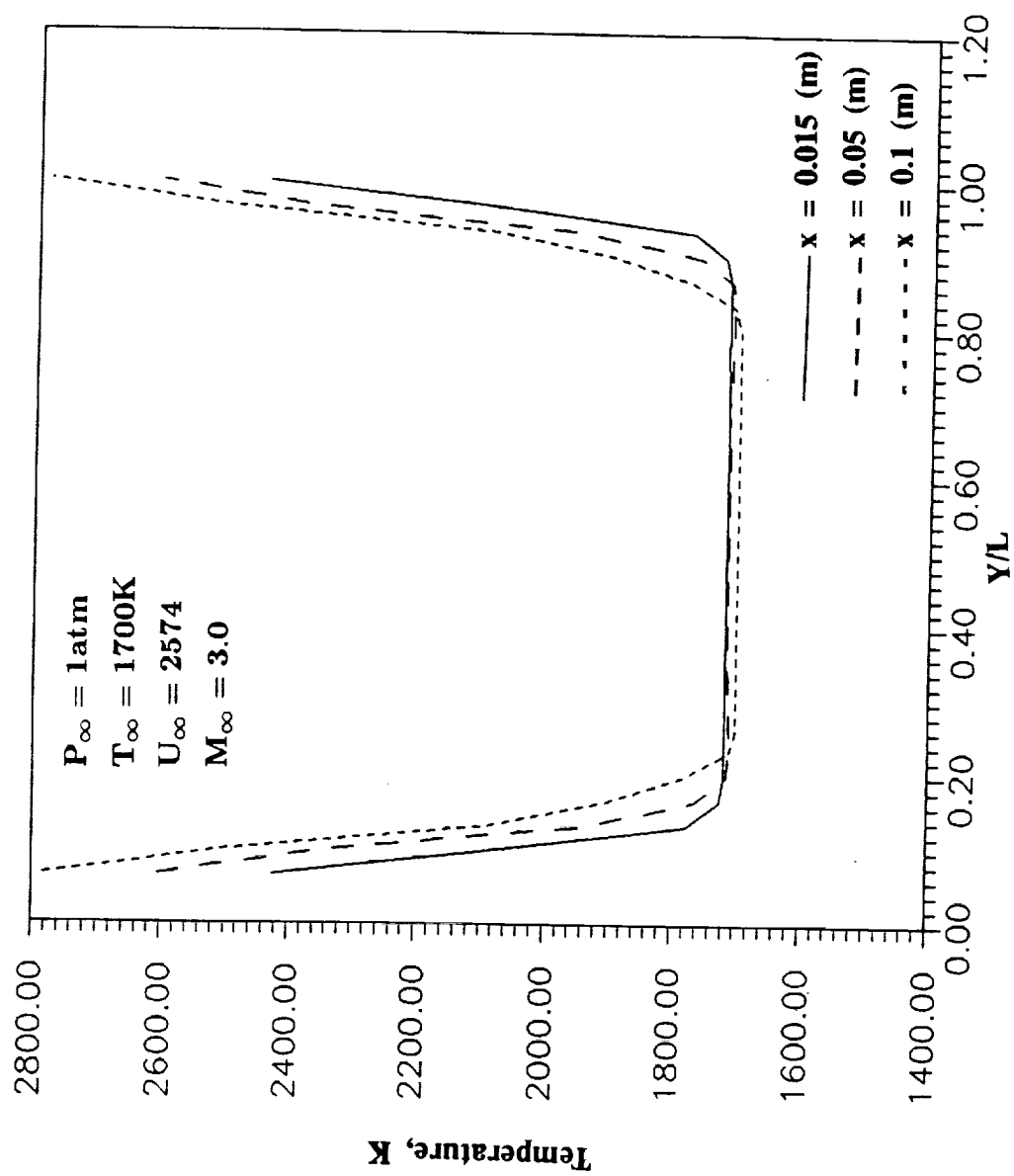


Fig. 5.11 Temperature variation across the channel at various x locations, $M_{\infty} = 3.0$.

boundary layer interaction, the temperature increases along the flow. The radiative heat transfer result shows the same trend as Fig. 5.4

In order to investigate the effect of boundary conditions on the flow, two different boundary conditions were selected. In the first case the temperature of the boundary was maintained constant at a higher value than the free stream temperature and in the second case it was maintained at a lower value. The free stream values were kept the same as before.

Figures 5.12 and 5.13 show the temperature and velocity profile for the constant temperature wall boundary condition with where $T_w = 3000$ K. It seen that the temperature boundary layer is more well developed than is the velocity boundary layer, due to energy transfer from the high temperature wall to the fluid. Figure 5.14 shows the radiative flux for the above condition. It is seen that near the entrance of the channel, due to a high temperature gradient the radiative flux is very high. However, towards the exit, since the flow attains a steady-state value, the temperature is evenly distributed, resulting in the decrease in radiative flux.

Figures 5.15 and 5.16 show the velocity and temperature profile when the wall temperature is kept lower than the free stream temperature ($T_w = 1000$ K). In this case, an opposite trend is seen. Figure 5.17 shows the radiative flux for the above case. The result shows the same trend as before. Since there is change in the direction of heat flow, the radiative flux changes sign.

The influence of radiative interactions in chemically reacting supersonic internal flows was investigated by considering the physical model shown in Fig. 2.5. The specific problem considered is the supersonic flow of premixed hydrogen and air with an equivalence ratio of unity in a channel with a compression corner on the lower boundary.

PAGE _____ INTENTIONALLY BLANK

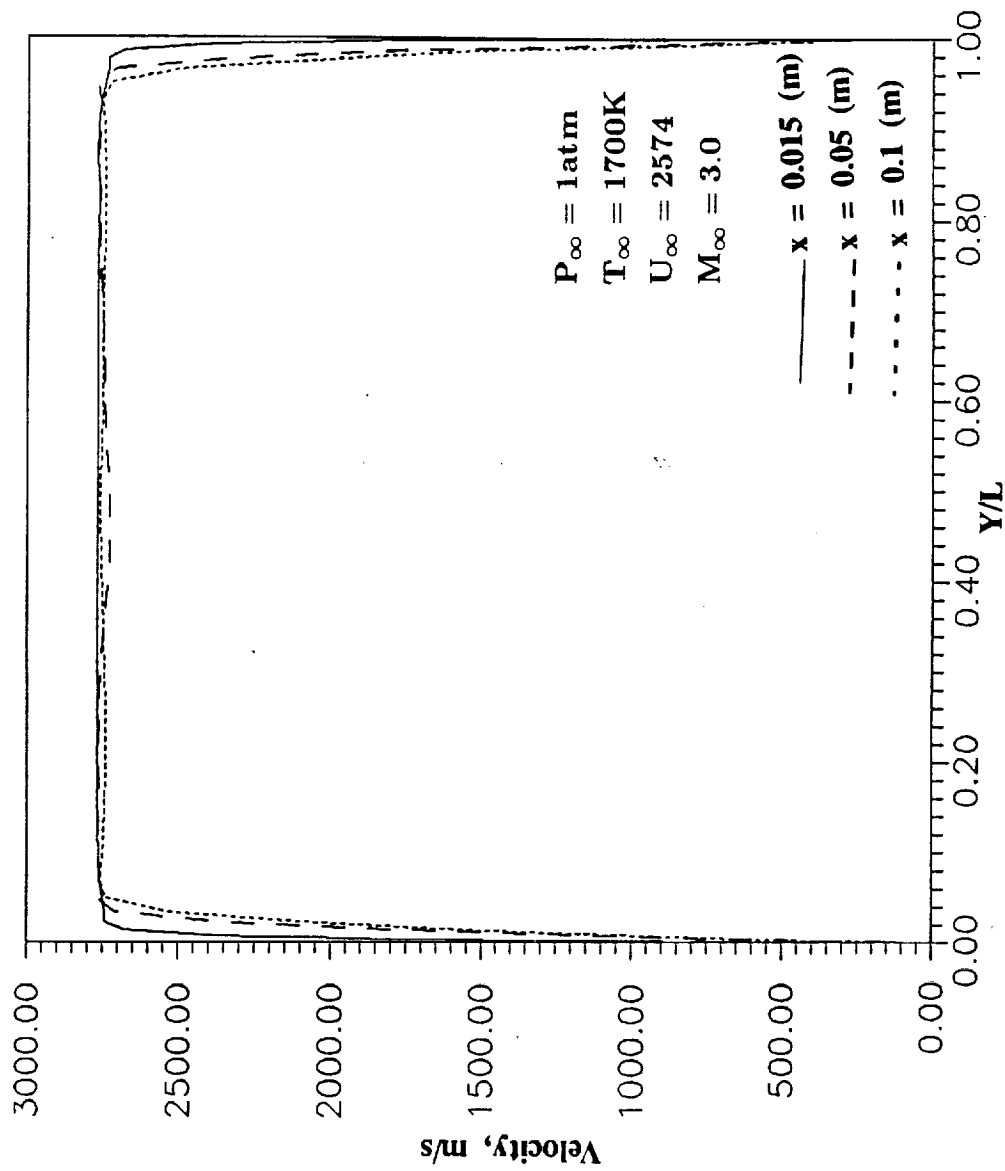


Fig. 5.12 Variation of axial velocity across the channel at various x locations, $M_{\infty} = 3.0$, $T_w = 3000 \text{ K}$.

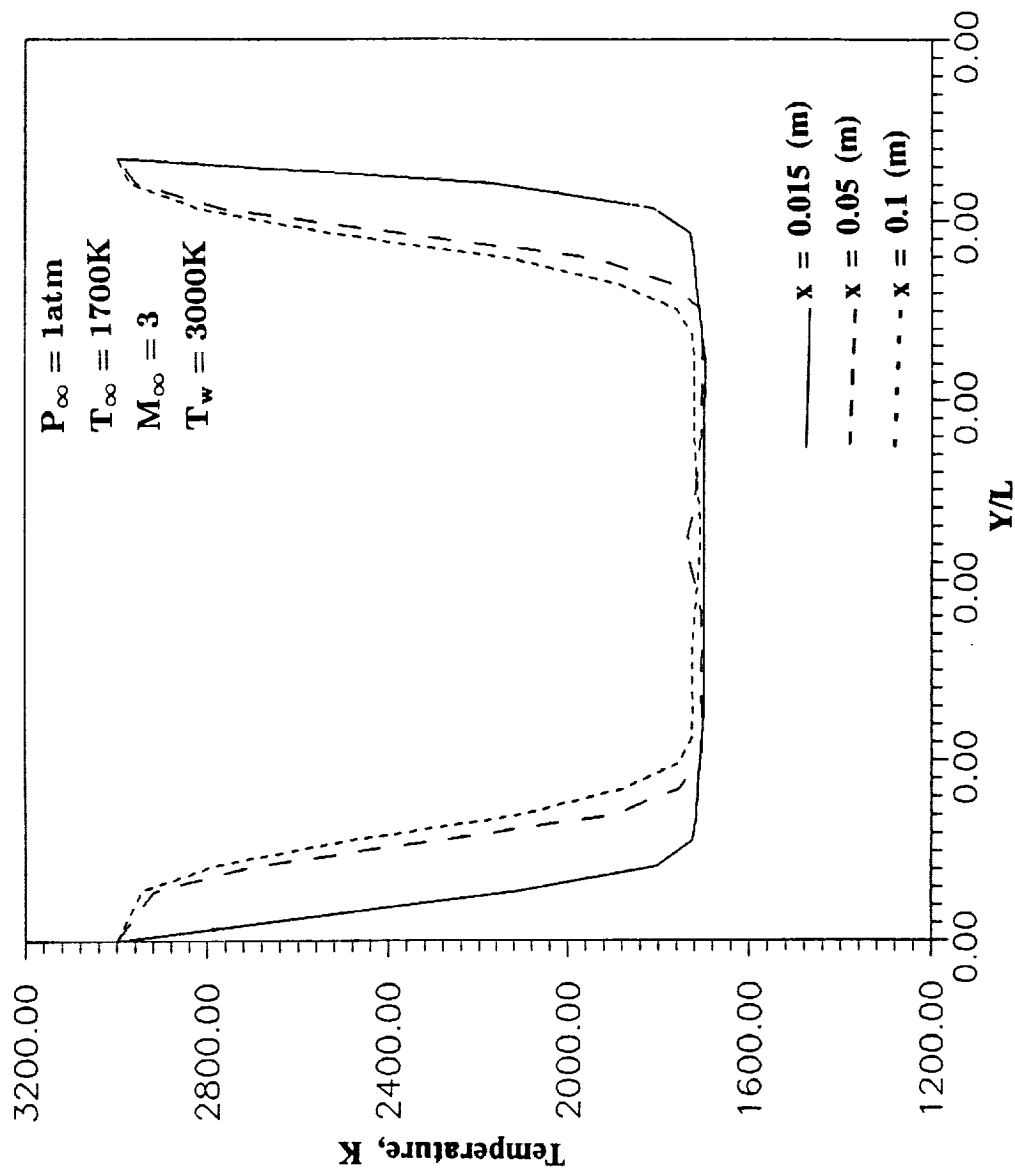


Fig. 5.13 Temperature variation across the channel at various x locations, $M_{\infty} = 3.0$.

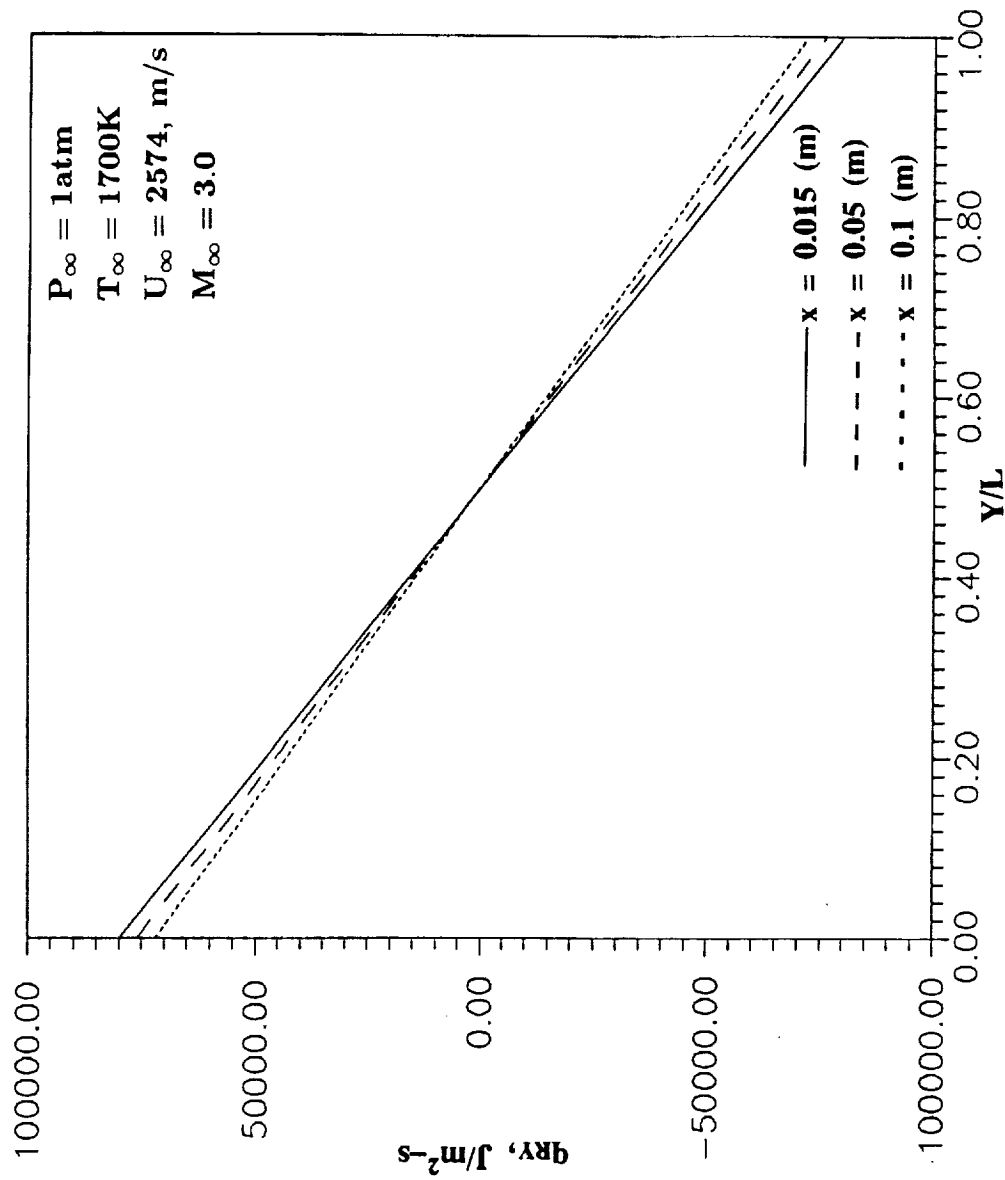


Fig. 5.14 Variation of q_{ry} with y for different x locations, $M_{\infty} = 3.0$, $T_w = 3000 \text{ K}$.

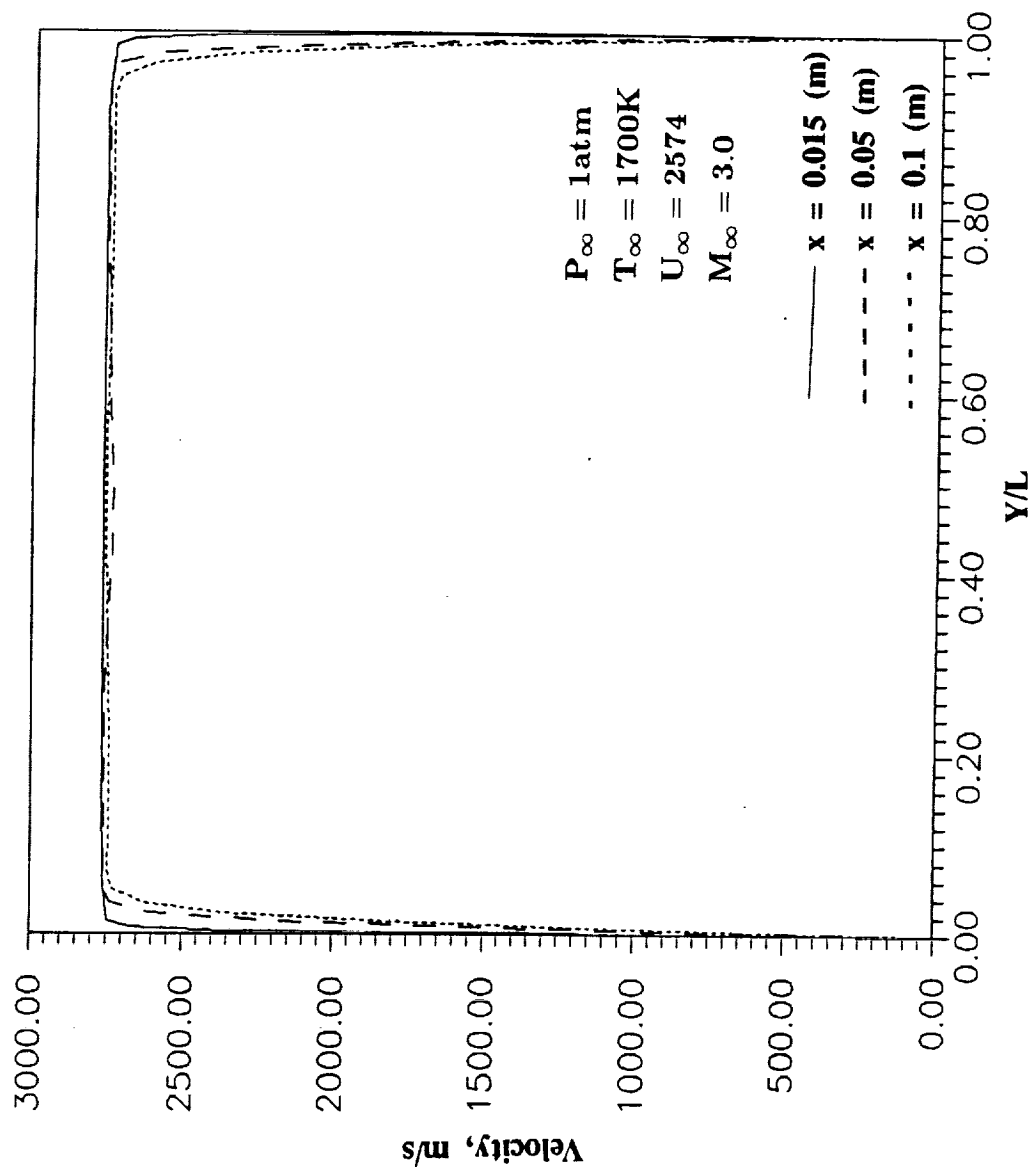


Fig. 5.15 Variation of axial velocity across the channel at various x locations, $M_{\infty} = 3.0$, $T_w = 1000 \text{ K}$.

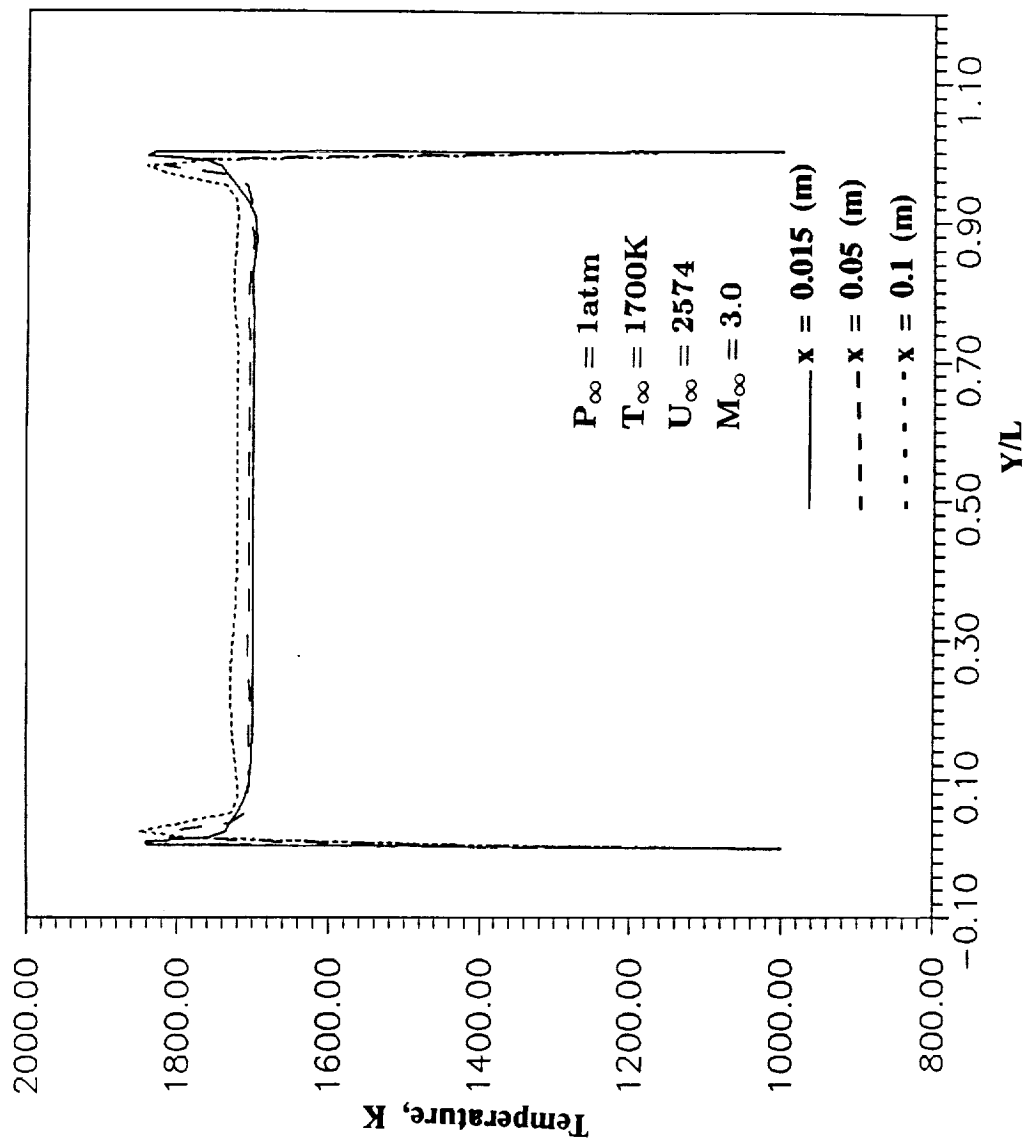


Fig. 5.16 Temperature variation across the channel at various x locations, $M_{\infty} = 3.0$.

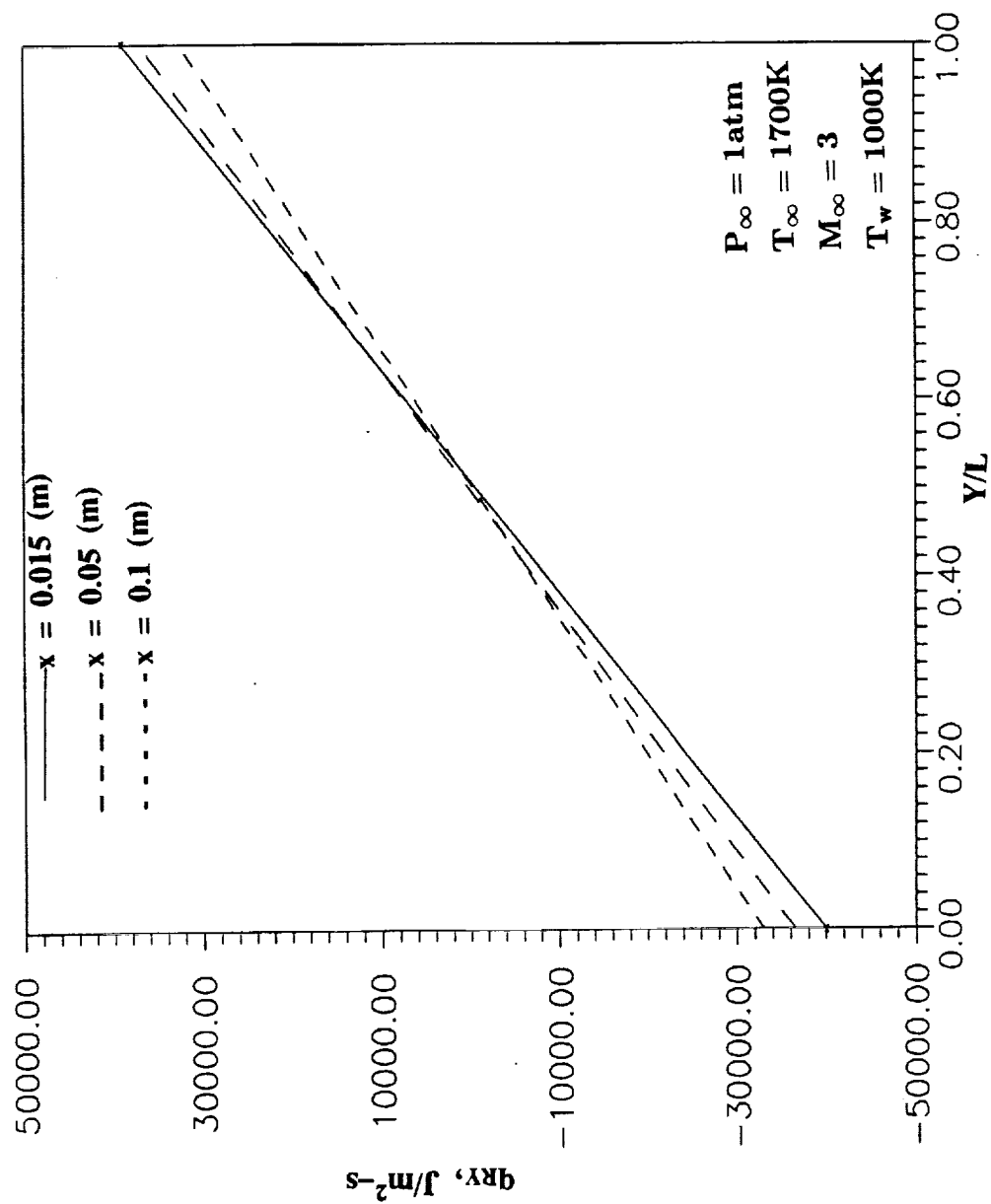


Fig. 5.17 Variation of q_{RY} with y for different x locations, $M_{\infty} = 3.0$.

The physical dimensions considered for obtaining results are $L=2$ cm, $x_1=1$ cm, $x_2=2$ cm, $L_x=x_1+x_2=3$ cm, and $\alpha=10^\circ$. The inlet conditions, which are representative of the scramjet operating conditions, are $P=1$ atm, $T=900$ K and $M=3.0$. The flow is ignited by the shock from the compression corner. The flowfield for this problem has been investigated by several researchers [25–29], where different models have been used. Influence of radiative interactions was investigated in [25] by considering a simple two step model. Recently a [28], comparative study of the flow field was conducted using three chemistry models (see Table 2.1). It was found that significant amount of radiation participating species are produced by the 35–step chemistry model. Complete discussion of the use of the three chemistry models with and without radiation are provided in [28]. Selected results obtained by using the 18–step chemistry model are presented here to demonstrate the influence of radiative interactions.

The computed results for the 18–step chemistry model are presented in Figs. 5.18–5.22, both with and without radiative interactions. The results were obtained using a 31×31 grid; this was found to be an appropriate grid for the model. The variations in temperature, pressure, and species concentration along the x-coordinate are shown for a y-location of 0.025 cm from the lower wall. The shock occurs at about $x/L_x=1/3$, and it was noted in [28] that the 35–step chemistry model predicts the ignition time accurately.

The variation in temperature and pressure is shown in Figs. 5.18 and 5.19, respectively. The temperature is seen to increase uniformly along the channel (Fig. 5.18) and there is a significant increase in pressure after the shock (Fig. 5.19). The strong fluctuation in pressure after the main shock is attributed to reflection of weak shocks from the boundaries.

Variation in species production are shown in Figs. 5.20–5.22. At moderate

PAGE _____ INTENTIONALLY BLANK

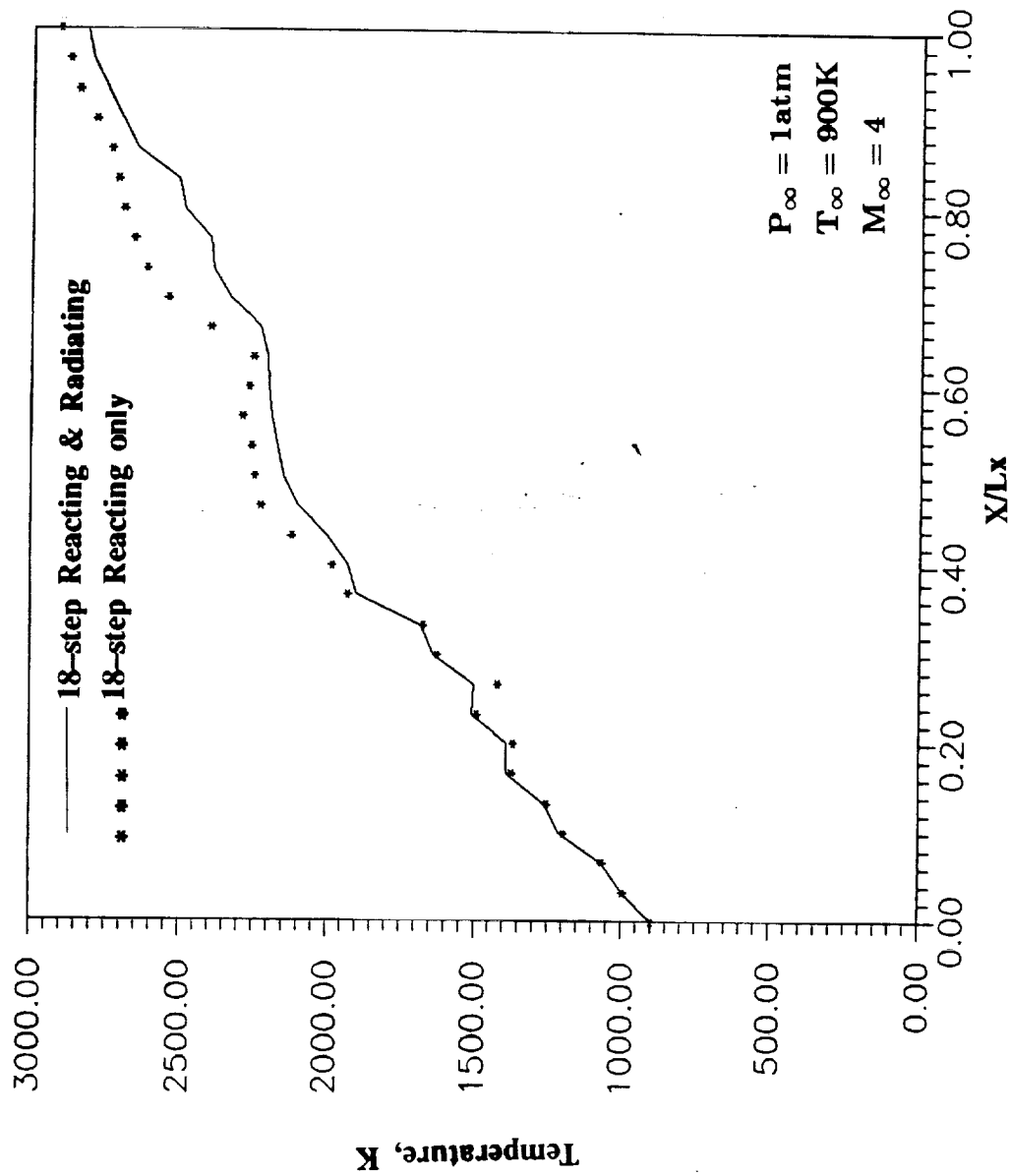


Fig. 5.18 Temperature variation with x for reacting, and reacting and radiating flows.

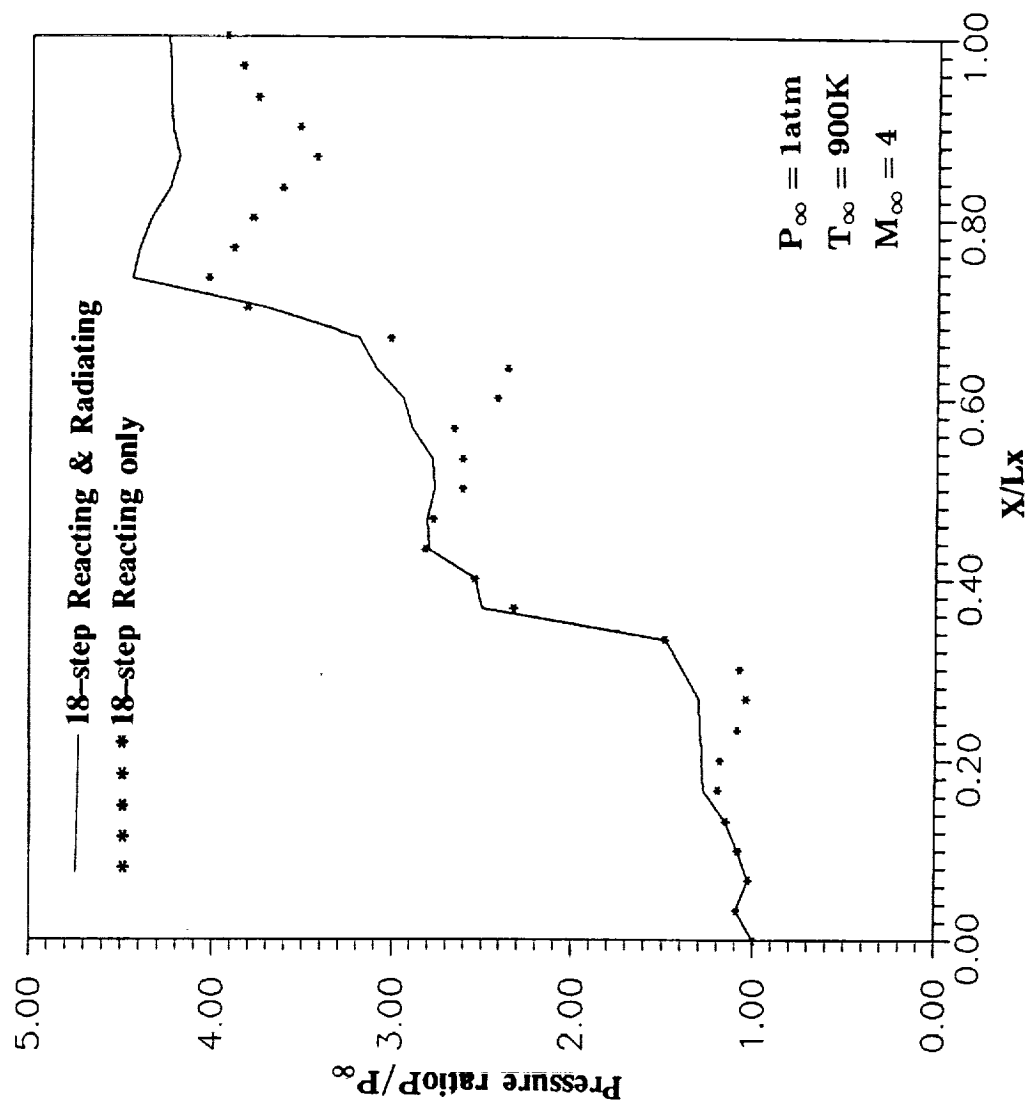


Fig. 5.19 Pressure variation with x for reacting, and reacting and radiating flows.

temperatures, symmetric molecular species such as O_2 and H_2 do not participate in the radiative process. Consequently, under the physical conditions of the problem, mass fractions of O_2 and H_2 are not influenced by the radiative interaction (Fig. 5.20). The concentration of O_2 and H_2 decreases in the downstream regions as these species react to form H_2O and OH . A slight decrease in the production of both H_2O and OH is noted after the shock due to radiative interactions. In the case of reacting flows without radiation, the ignition is seen to take place at $x/L_x=0.37$ indicating a longer ignition delay [28]. However, for the reacting and radiating case, the ignition is seen to occur at $x/L_x=0.33$. This demonstrates that the effect of radiative interaction is to nullify the difference in the ignition delay.

The results of radiative heat transfer by three chemistry models were compared in [28], and these are presented here for the sake of completeness. The results for the normal radiative flux presented in Fig. 5.23 demonstrate that radiative interactions increase rapidly after the shock. The three models are seen to predict the same general trend. The results of streamwise radiative flux illustrated in Fig. 5.24 show that the net q_{RX} decreases towards the end of the channel. This is due to the cancellation of fluxes in the positive and negative x-directions. It is noted that the net radiative transfer is in the negative x-direction. The 18-step and 35-step models are seen to predict significantly higher q_{RX} than does the 2-step model. This is because radiative heat transfer is a strong function of temperature, pressure, and species concentration, which are higher (in the positive x-direction) for the 18-step and 35-step models than for the 2-step model.

FILE INTENTIONALLY BLANK

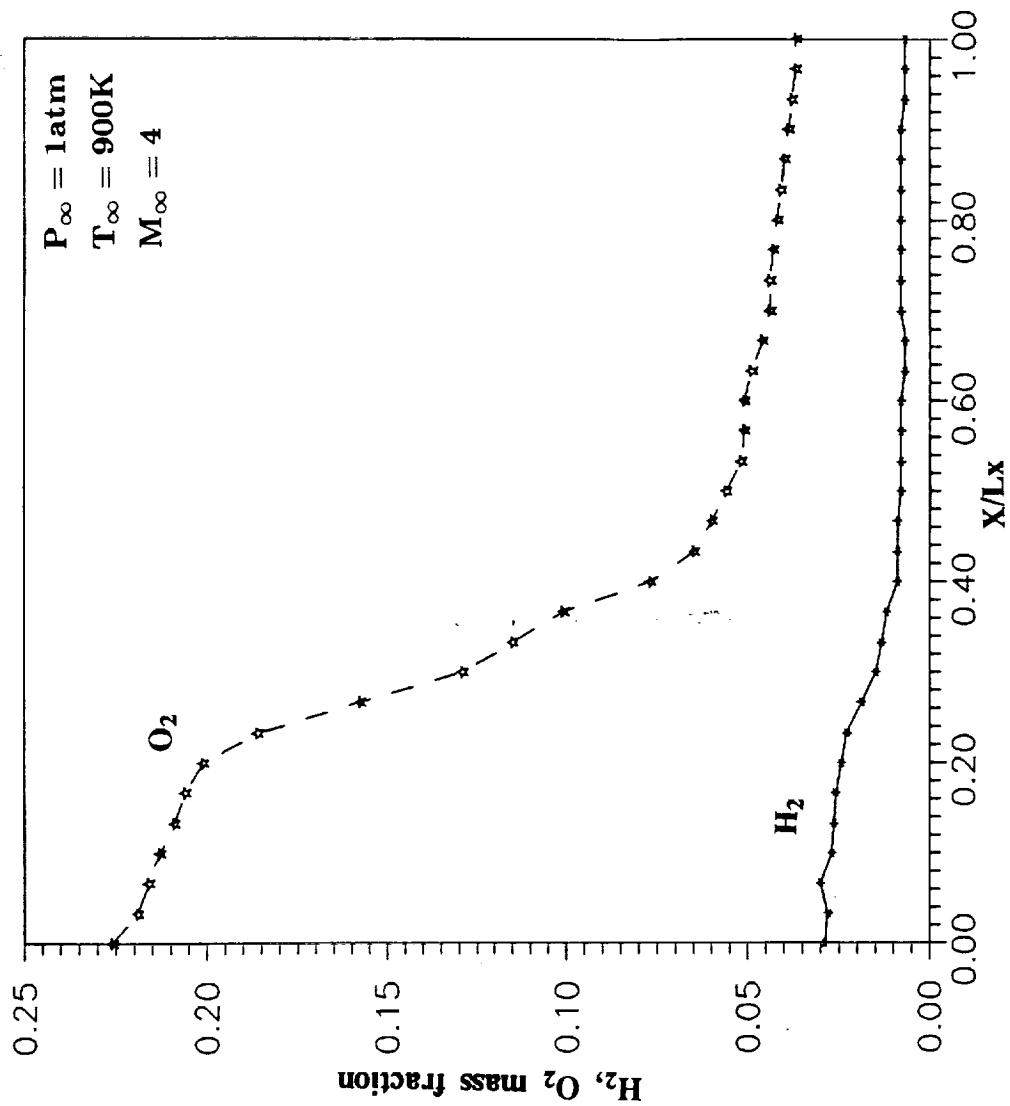


Fig. 5.20 Variation of H_2 , O_2 for reacting flows.

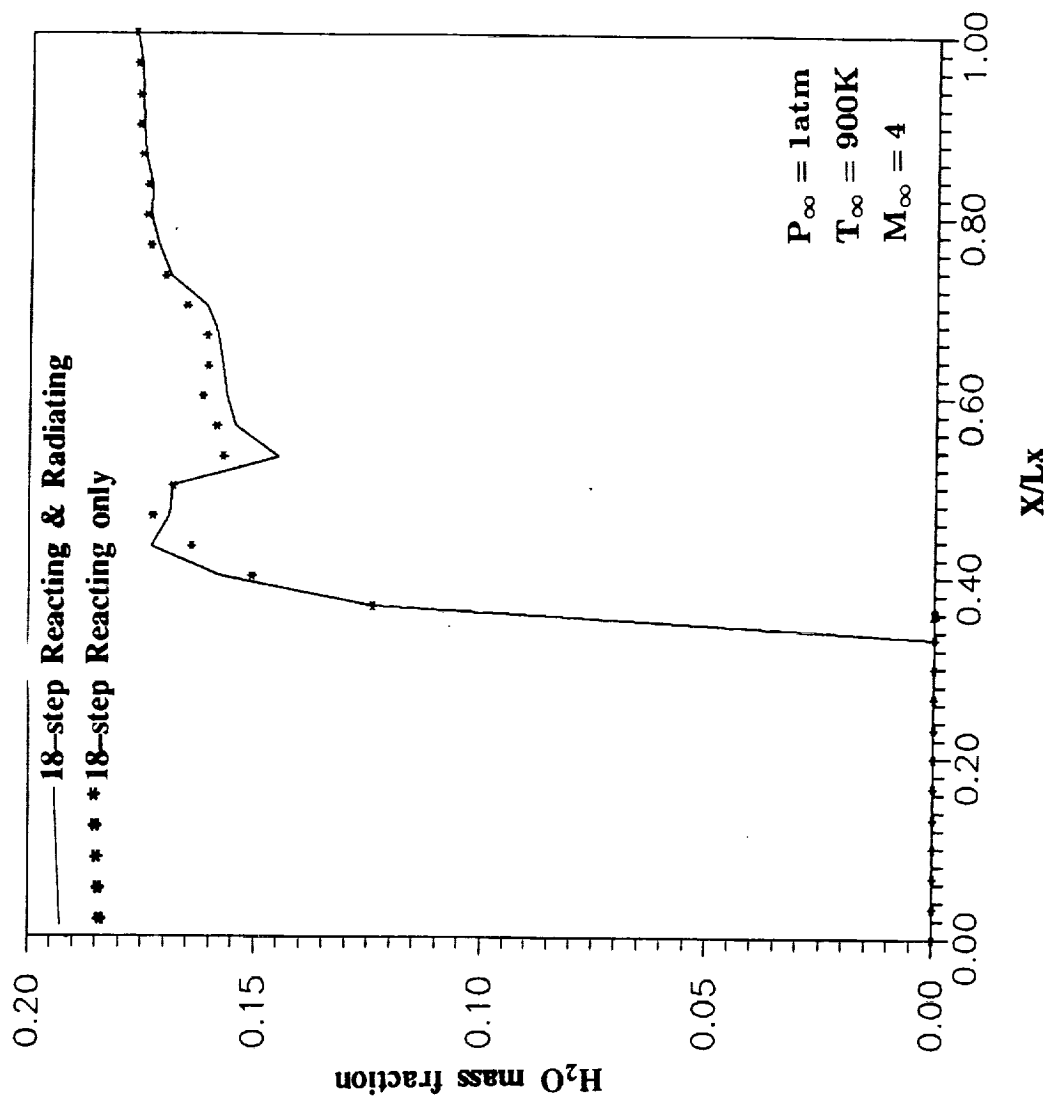


Fig. 5.21 Variation of H_2O mass fraction with x for reacting, and reacting and radiating flows.

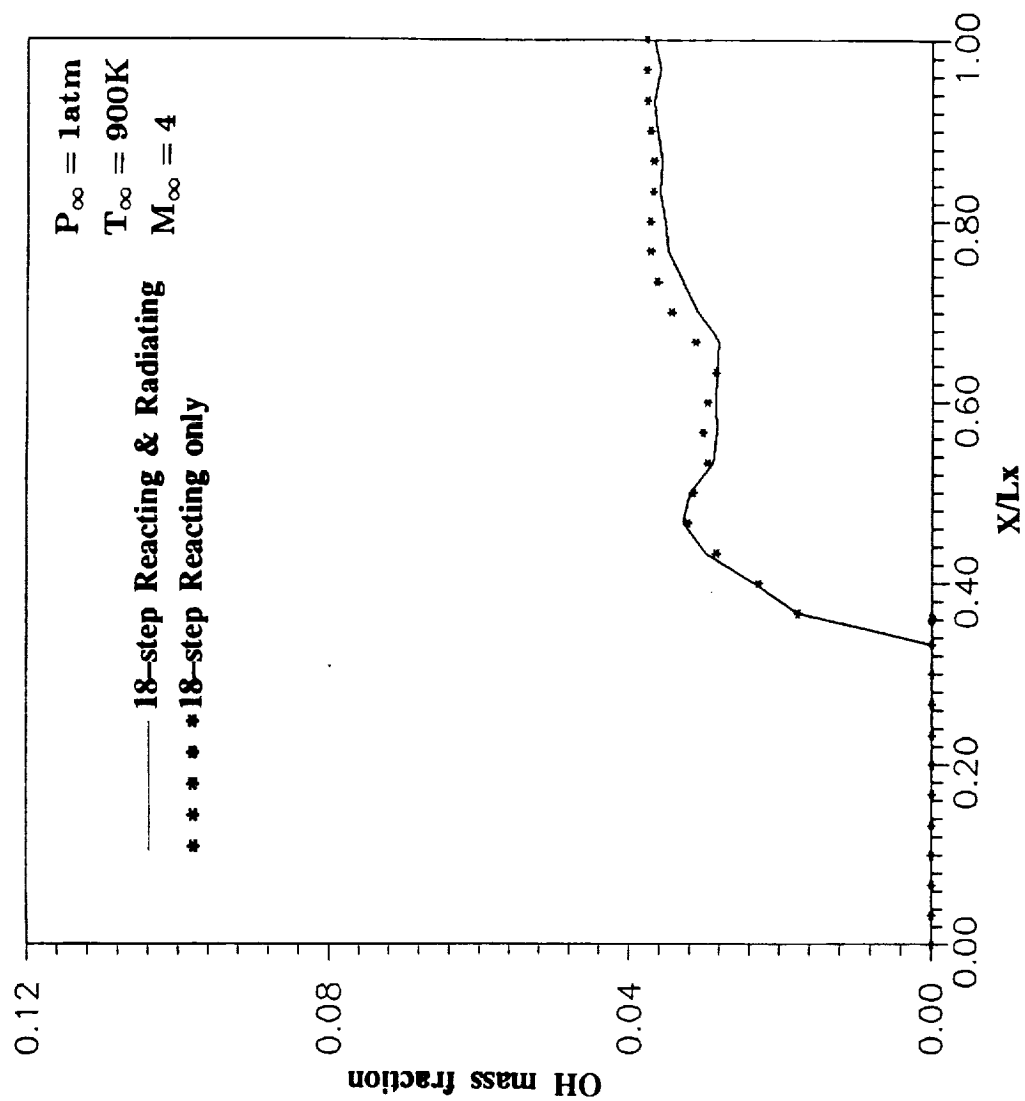


Fig. 5.22 Variation of OH mass fraction with x for reacting, and reacting and radiating flows .

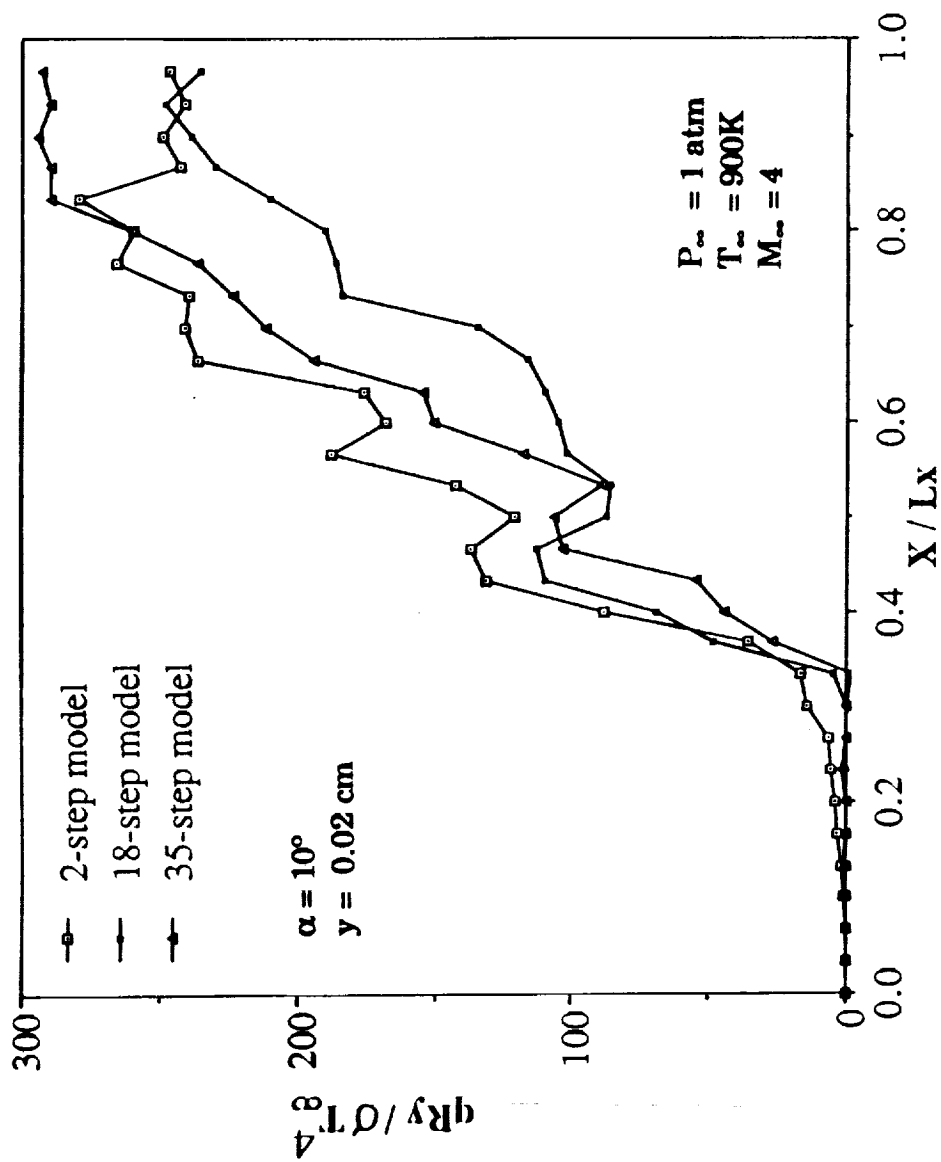


Fig. 5.23 Variation of normal radiative flux with x for three chemistry models.

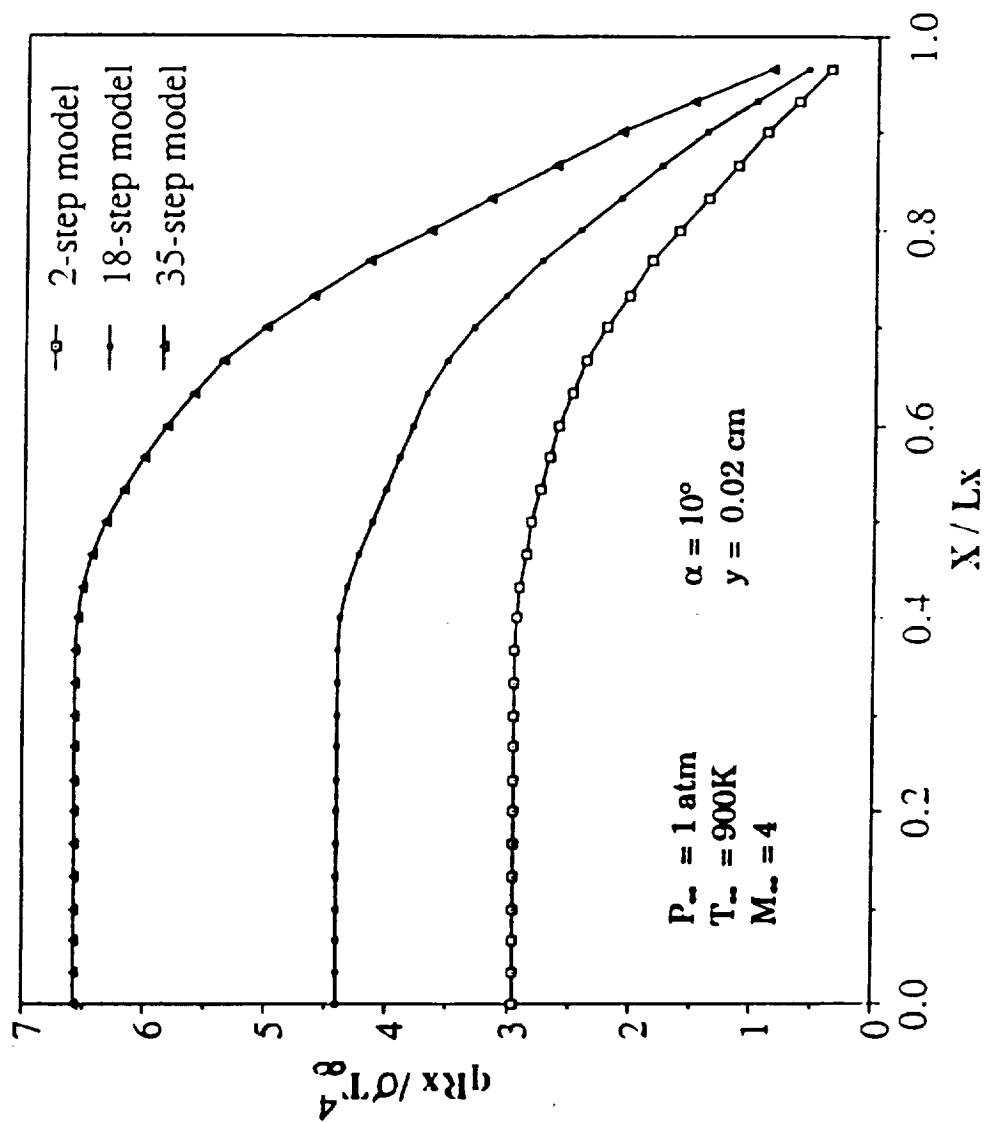


Fig. 5.24 Variation of streamwise radiative flux with x for three chemistry models.

PAGE _____ INTENTIONALLY BLANK

Chapter 6

CONCLUSIONS

The two dimensional Navier–Stokes equations have been used to investigate the influence of radiative energy transfer on the entrance region flow under supersonic flow conditions. In the hypersonic propulsion system, the temperature ranges from one to five thousand degrees Kelvin. In this range, various nonsymmetric molecules become highly radiative participating. One-dimensional radiative flux was included in the energy equation for the solution of nonreacting supersonic flows between parallel plates. Specific results have been obtained for different amounts of H_2O , OH , and NO in combination with air. Results demonstrate that the radiative interaction increases with increase in pressure, temperature, amount of participating species, plate spacing, and Mach number. This can have a significant influence on the overall energy transfer in the system. Most energy, however, is transferred by convection in the flow direction.

The radiative interactions in reacting flows have been investigated by considering the supersonic flow of premixed hydrogen and air in a channel with a 10° compression corner at the lower boundary. The finite rate chemistry model employed is a nine species 18–step model. The results show that the effect of radiative interaction is to nullify the ignition delay i.e., the reacting and radiating flow predicts a more accurate position of the shock. The radiative influence is found to be stronger in the boundary layers, and this is seen to change the temperature, pressure, and species concentration in the flow

direction. Thus radiative heat transfer can have a significant effect on the entire flow field of a hypersonic propulsion system.

Some earlier results obtained during the course of this study were presented at the 29th Aerospace Sciences Meeting in Reno, Nevada, January 7-10, 1991 (AIAA Papers 91-0373 and 91-0572). These are provided in this report as Appendices F and G.

REFERENCES

1. Sparrow, E. M. and Cess, R. D., Radiation Heat Transfer, Brooks/Cole, Belmont, Calif., 1966 and 1970. New Augmented Edition, Hemisphere Publishing Corp., Washington, D.C., 1978.
2. Hottel, H. C. and Sarofim, A. F., Radiative Heat Transfer, McGraw-Hill Book Co., New York, 1967.
3. Siegel, R. and Howell, J. R., Thermal Radiation Heat Transfer, McGraw-Hill Book Co., New York, 1971; Second Edition, 1981.
4. Ozisik, M. N., Radiative Transfer and Interaction with Conduction and Convection, John Wiley & Sons, Inc., New York, 1973.
5. Edwards, D. K., Radiation Heat Transfer Notes, Hemisphere Publishing Corporation, Washington, D.C., 1981.
6. Cess, R. D., "The Interaction of Thermal Radiation with Conduction and Convection Heat Transfer", Advances in Heat Transfer, Vol. 1, Academic Press, New York, 1964.
7. Sparrow, E. M., "Radiation Heat Transfer between Surfaces," Advances in Heat Transfer, Vol. 2, Academic Press, New York, 1965.
8. Viskanta, R., "Radiation Transfer and Interaction of Convection with Radiation Heat Transfer," Advances in Heat transfer, Vol. 3, Academic Press, New York, 1966.
9. Tien, C. L., "Thermal Radiation Properties of Gases," Advances in Heat Transfer, Vol. 5, Academic Press, New York, 1968.
10. Cess, R. D. and Tiwari, S. N., "Infrared Radiative Energy Transfer In Gases," Advances in Heat Transfer, Vol. 8, Academic Press, New York, 1972.
11. Edwards, D. K., "Molecular Gas band Radiation," Advances in Heat Transfer, Vol. 12, Academic Press, New York, 1976.
12. Tiwari, S. N., "Band Model Correlations for Infrared Radiation," Radiative Transfer and Thermal Control (Progress in Astronautics and Aeronautics), Vol. 49, American Institute of Aeronautics and Astronautics, New York, 1976.
13. Tiwari, S. N., "Band Models for Infrared Atmospheric Radiation," Advances in Geophysics, Vol. 20, Academic Press, New York, 1978.

14. Viskanta, R., "Radiation Heat Transfer," Fortschrift der Verfahrenstechnik, Vol. 22A, May 1984, pp. 51-81.
15. Viskanta, R. and Menguc, M. P., "Radiation Heat Transfer In Combustion Systems," Progress in Energy Combustion Sciences, Vol. 13, No. 2, 1987, pp. 97-160.
16. Cess, R. D. and Tiwari, S. N., "Heat Transfer to Laminar Flow of an Absorbing-Emitting Gas Between Parallel Plates," Heat and Mass Transfer-USSR, Vol. 1, May 1968, pp. 229-283.
17. Tiwari, S. N. and Cess, R. D., "Heat Transfer to Laminar Flow of Nongray Gases through a Circular Tube," Applied Scientific Research, Vol.25, No. 3/4, December 1971, pp. 155-170.
18. Tiwari, S. N., "Application of Infrared Band Model Correlations to Nongray Radiation," International Journal of Heat and Mass Transfer, Vol. 20, No. 7, July 1977, pp. 741-751.
19. Tiwari, S. N., "Radiative Interaction in Transient Energy Transfer in Gaseous System," NASA CR-176644, December 1985.
20. Tiwari, S. N. and Singh, D. J., "Interaction of Transient Radiation in Fully Developed Laminar Flow," AIAA Paper No. 86-1521, June 1987.
21. Kumar, A., "Numerical Simulation of Scramjet Inlet Flow Field," NASA TP-25117, May 1986.
22. Drummond, J. P., Hussaini, M. Y. and Zang, T. A., "Spectral Methods for Modelling Supersonic Chemically Reacting Flowfields," AIAA Journal, Vol, 24, No. 9, September 1986, pp. 1461-1467; also Drummond, J.P., "Numerical Simulation of a Supersonic Chemically Reacting Mixing Layers," Ph.D. Dissertation, George Washington University, May 1987.
23. Drummond, J. P., Rogers, R. C. and Hussaini, M. Y., "A Detailed Numerical Model of a Supersonic Reacting Mixing Layer," AIAA Paper No. 86-1427, June 1986.
24. Chitsomboon, T., Kumar, A., Drummond, J. P., and Tiwari, S. N., "Numerical Study of Supersonic Combustion Using a Finite-Rate Chemistry Model," AIAA Paper No. 86-0309, January 1986.
25. Mani, M., Tiwari, S. N., and Drummond, J. P., "Numerical Solution of Chemically Reacting and Radiating Flows," AIAA Paper No. 87-0324, January 1987.
26. Mani, M., Tiwari, S. N., and Drummond, J. P., "Investigation of Two-Dimensional Chemically Reacting and Radiative Supersonic Channel Flows," AIAA Paper 88-0462, January 1988.

27. Mani, M. and Tiwari, S.N., "Investigation of Supersonic Chemically Reacting and Radiating Channel flows," NASA CR-182726, January 1988; also Ph.D. Dissertation by M. Mani, Old Dominion University, May 1988.
28. Chandrasekhar, R., Tiwari, S. N., and Drummond, J. P., "Radiative Interactions in a Hydrogen-Fueled Supersonic Combustor," AIAA Paper No. 91-0373, January 1991.
29. Tiwari, S. N., Chandrasekhar, R., and Thomas, A. M., "Investigation of Radiative Interaction in Chemically Reacting Supersonic Internal Flows," AIAA Paper No. 91-0572, January 1991.
30. Martin, J. K. and Hwuang, C. C., "Combined Radiant and Convective Heat Transfer to Laminar Steam Flow between Gray Parallel Plates with Uniform Heat Flux," Journal of Quantitative Spectroscopy and Radiative Transfer, Vol 15, 1975, pp. 1701-1081.
31. Viskanta, R., "Heat Transfer in a Radiating Fluid With Slug Flow in a Parallel Plate Channel," Applied Scientific Research, Section A, Vol.13, No. 4-5, February 1964, pp. 291-311
32. Kobiyama, M., Taniguchi, H., and Saito, T., "The Numerical Analysis of Heat Transfer Combined with Radiation and Convection," Japanese Society of Mechanical Engineers, Vol. 22 No. 167, May 1979, pp. 707-1414.
33. Im, K. H. and Alluwalia, R. K., "Combined Convection and Radiation in Rectangular Ducts," International Journal of Heat and Mass Transfer, Vol. 27, No. 2, 1984, pp. 221-231.
34. Tiwari, S. N., Singh, D. J. and Trivadi, P. A., "Radiative Interactions in Laminar Incompressible and Compressible Internal Flows," AIAA Paper No. 90-0134, January 1990.
35. Soufiani, A. and Taine, J., "Application of Statistical Narrow Band Model to Coupled Radiation and Convection at High Temperature," International Journal of Heat and Mass Transfer, Vol.30, No.3, March 1987, pp.437-447.
36. Rogers, R. C. and Schnexnayder, C. J., Jr., "Chemical Kinetic Analysis of Hydrogen-Air Ignition and Reaction Time," NASA TP-1856, 1981.
37. Rogers, R. C. and Chinitz, W., "Using a Global Hydrogen-Air Model in Turbulent Reacting Flow Calculations," AIAA Journal, Vol. 21, No. 4, April 1983.
38. Frankel, S. H., Drummond, J. P. and Hassan, H. A., "A Hybrid Reynolds Average/PDF Closure Model for Supersonic Turbulent Combustion," AIAA Paper No. 90-1573, July 1990.

39. Wilkins, J. H., The Algebraic Eigenvalue Problem, Oxford University Press, Oxford, England, 1965, pp. 233-236.
40. Stalnaker, J. F., Robinson, M. A., Spradley, L. W., Kurzius, S. C., and Theores, D., "Development of the General Interpolants Methods for the CYBER 200 Series of Computer," Report TR-0867354, Lockheed-Huntsville Research Engg. Center, Huntsville, Alabama, October 1983.
41. Patch, R., "Effective Absorption Coefficient for Radiant Energy Transport in Nongray Nonscattering gases," Journal of Quantitative Spectroscopy and Radiative Transfer, Vol. 7, No. 4, July/August 1967, pp. 611-637.
42. Smith, R. E. and Weigel, B. L., "Analytical and Approximate Boundary Fitted Coordinate System For Fluid Flow Simulation," AIAA Paper No. 80-0192, January 1980.
43. MacCormack, R. W., "The Effect of Viscosity in Hypervelocity Impact Cratering," AIAA Paper No. 69-354, May 1969.
44. Bussing, T. R. and Murman, E. M. "A Finite Volume Method For the Calculation of Compressible Chemically Reacting Flows," AIAA Paper No. 85-0331, January 1985.
45. Householder, A. S. The Theory of Matrices in Numerical Solution Analysis, Dover Publication, New York, 1964, pp. 122-140.
46. Carpenter, M. H., "A generalized Chemistry Version Of Spark," NASA CR-4196, December 1989.

APPENDICES

2000 INTENTIONALLY BLANK

APPENDIX A

DERIVATION OF THE CONDUCTION HEAT FLUX TERM

The derivation of the conduction heat flux terms is obtained directly from Ref. 27. To simplify Eq. (2-3a) and Eq. (2-3b), the Lewis number is assumed to be unity. This simplification is carried out in detail for Eq. (2-3a) and the same is applied to Eq. (2-3b). Using the expression for the thermal diffusivity (α) and Lewis number (L_e), Eq. (2-3a) can be expressed as

$$\alpha = \frac{\kappa}{\rho \bar{C}_p}$$

$$L_e = \frac{\alpha}{D} \quad (A-1)$$

$$q_{cy} = -\rho D \left(L_e \bar{C}_p \frac{\partial t}{\partial y} + \sum_{i=1}^m \frac{\partial f_i}{\partial y} h_i \right)$$

Defining the binary diffusion coefficient D in terms of the Prandtl and Lewis number Eq.(A-1) can be expressed as

$$P_r = \frac{\nu}{\alpha}$$

$$D = \frac{\alpha}{L_e} = \frac{\nu}{P_r L_e} = \frac{\mu}{\rho P_r L_e} \quad (A-2)$$

$$q_{cy} = -\frac{\mu}{P_r} \left[\bar{C}_p \frac{\partial T}{\partial y} + \sum_{i=1}^m \frac{\partial f_i}{\partial y} h_i \right]$$

where

$$\bar{C}_p = \sum_{i=1}^m f_i C_{p_i}$$

The static enthalpy of the mixture is given by the relation

$$h = \sum_{i=1}^m \left[h_i^0 + \int_0^T C_{p_i} d\eta \right] f_i \quad (A-3)$$

It should be noted that η is a dummy variable employed to evaluate the sensible enthalpy. Using the Leibnitz formula Eq. (A-3) is differentiated to obtain

$$\begin{aligned} \frac{\partial h}{\partial y} = & \sum_{i=1}^m \left[h_i^0 + \int_0^T C_{p_i}(\eta) d\eta \right] \frac{\partial f_i}{\partial y} + f_i \frac{\partial h_i^0}{\partial y} \\ & + f_i \int_0^T \frac{\partial C_{p_i}(\eta)}{\partial \eta} d\eta + f_i C_{p_i}(T) \frac{\partial T}{\partial y} \end{aligned} \quad (A-4)$$

The coefficient on the right hand side is equal to h_i and the second and third terms are identical to zero, therefore, Eq.(A-4) reduces to

$$\begin{aligned} \frac{\partial h}{\partial y} &= \sum_{i=1}^m \left[h_i \frac{\partial f_i}{\partial y} + f_i C_{p_i} \frac{\partial T}{\partial y} \right] \\ \text{Or} \\ \frac{\partial h}{\partial y} &= \sum_{i=1}^m h_i \frac{\partial f_i}{\partial y} + C_p \frac{\partial T}{\partial y} \end{aligned} \quad (A-5)$$

Substituting Eq. (A-5) into Eq. (A-2) q_{cy} is expressed as

$$\begin{aligned} q_{cy} &= -\frac{\mu}{P_r} \frac{\partial h}{\partial y} \\ \text{Or} \\ q_{cy} &= \frac{\gamma \mu}{P_r} \frac{\partial e}{\partial y} \end{aligned} \quad (A-6)$$

APPENDIX B

RADIATIVE FLUX EVALUATION FOR THE PSEUDO GRAY MODEL

Most of the materials in this appendix are also taken from Ref. 27. This appendix shows the discretization and evaluation of the radiative flux for the y - direction. The same thing can be applied in the streamwise direction. Equations (3-31) and (3-32) in the y - direction are written as follows

$$\frac{d^2 q_r(y)}{dy^2} - \frac{9}{4} \kappa^2(y) q_r(y) = 3\kappa(y) \frac{de(y)}{dy} \quad (B-1)$$

$$\kappa(y) \left(\frac{1}{\epsilon_1} - \frac{1}{2} \right) q_r(y) |_{y=0} - \frac{1}{3} \frac{dq_r(y)}{dy} |_{y=0} = 0 \quad (B-2)$$

$$\kappa(y) \left(\frac{1}{\epsilon_2} - \frac{1}{2} \right) q_r(y) |_{y=L} - \frac{1}{3} \frac{dq_r(y)}{dy} |_{y=L} = 0 \quad (B-3)$$

The above equations is discretized by central differencing . The second derivative of q_r in the physical domain is discretized as

$$\frac{d^2 q_r}{dy^2} |_j = \frac{2}{\Delta y_j (1 + \beta_j)} \left[\frac{q_{j+1} - q_j}{\beta_j \Delta y_j} - \frac{q_j - q_{j-1}}{\Delta y_j} \right] \quad (B-4)$$

where

$$\Delta y_j = y_j - y_{j-1} \quad \text{and} \quad \beta_j = \frac{y_{j+1} - y_j}{y_j - y_{j-1}}$$

Equation (B-4) in discrete forms are written as

$$\begin{aligned} & \frac{2}{\Delta^2 y_j (1 + \beta_j)} q_{j-1} - \left[\frac{2}{\Delta y_j (1 + \beta_j)} \left(\frac{1}{\beta_j \Delta y_j} + \frac{1}{\Delta y_j} \right) + \frac{9}{4} \kappa_j^2 \right] q_j \\ & + \frac{2}{\Delta y_j^2 (1 + \beta_j) \beta_j} q_{j+1} = 1.5 \kappa_j \left[\frac{e_{j+1} - e_j}{\beta_j \Delta y_j} + \frac{e_j - e_{j-1}}{\Delta y_j} \right] \end{aligned} \quad (B-5)$$

$$\left[\kappa_1 \left(\frac{1}{\epsilon_1} - \frac{1}{2} \right) + \frac{1}{3 \Delta y_1} \right] q_1 - \frac{1}{3 \Delta y_1} q_2 = 0 \quad (B-6)$$

$$-\frac{1}{3 \Delta y_j} q_{j-1} + \left[\left(\frac{1}{\epsilon_2} - \frac{1}{2} \right) \kappa_j + \frac{1}{3 \Delta y_j} \right] q_j = 0$$

The above can be written in matrix form as

$$\begin{array}{cccccc} A & B & 0 & \dots & 0 & q_{r_1} & R_1 \\ C & A & B & 0 & \dots & 0 & R_2 \\ & & 0 & C & A & B & q_{r_{j-1}} = \\ 0 & \dots & 0 & C & A & & q_{r_j} & R_j \end{array} \quad (B-7)$$

where

$$A_{1,1} = \kappa_1 \left(\frac{1}{\epsilon_1} - \frac{1}{2} \right) + \frac{1}{3 \Delta y_1}$$

$$A_{ij} = - \left[\frac{2}{\Delta y_j (1 + \beta_j)} \left(\frac{1}{\beta_j \Delta y_j} + \frac{1}{\Delta y_j} \right) - \frac{9}{4} \kappa_j^2 \right] ; \quad j = 2, j-1$$

$$A_{ij} = \kappa_j \left(\frac{1}{\epsilon_1} - \frac{1}{2} \right) + \frac{1}{3 \Delta y_j}$$

$$B_{1,2} = - \frac{1}{3 \Delta y_1}$$

$$B_{ij} = \frac{2}{\Delta y_j^2 (1 + \beta_j) \beta_j} \quad ; \quad j = 3, j$$

$$C_{ij} = \frac{2}{\Delta y_j^2 (1 + \beta_j)} \quad ; \quad j = 2, j - 2$$

$$C_{ij-1} = -\frac{1}{3\Delta y_j}$$

$$R_1 = 0$$

$$R_j = 1.5\kappa_j \left[\frac{e_{j+1} - e_j}{\beta_j \Delta y_j} + \frac{e_j - e_{j-1}}{\Delta y_j} \right] \quad ; \quad j = 2, j - 1$$

$$R_j = 0$$

The tridiagonal matrix on the left hand side of Eq. (B-7) is solved efficiently by thomas algorithm

For a circular tube the differential form of radiative flux equation is given by

$$\frac{d}{dr} \left[\frac{1}{r} \frac{d}{dr} (rq_r) \right] - \frac{9}{4} \kappa^2 q_r = 3\kappa \frac{de}{dy} \quad (B-8)$$

$$\kappa(y) \left(\frac{1}{\epsilon_1} - \frac{1}{2} \right) q_r|_{y=0} - \frac{1}{3} \left[\frac{1}{r} \frac{d}{dr} (rq_r) \right] |_{y=0} = 0 \quad (B-9)$$

$$\kappa(y) \left(\frac{1}{\epsilon_2} - \frac{1}{2} \right) q_r|_{y=L} + \frac{1}{3} \left[\frac{1}{r} \frac{d}{dr} (rq_r) \right] |_{y=L} = 0$$

Differentiating Eq. (B-8) we get ,

$$\frac{d^2 q_r}{dr^2} + \frac{1}{r} \frac{dq_r}{dr} - \left(\frac{q_r}{r^2} + \frac{9}{4} \kappa^2 q_r \right) = 3\kappa \frac{de}{dy} \quad (B-10)$$

Eu. (B-10) along with boundary conditions (B-9) are discretized to give,

We know by central difference that

$$\begin{aligned}\frac{d^2 q_r}{dy^2} &= \frac{2}{\Delta y_j (1 + \beta_j)} \left[\frac{q_{j+1} - q_j}{\beta_j \Delta y_j} - \frac{q_j - q_{j-1}}{\Delta y_j} \right] \\ \frac{de}{dr} &= \frac{1}{2} \left[\frac{e_{j+1} - e_j}{\beta_j \Delta y_j} + \frac{e_j - e_{j-1}}{\Delta y_j} \right] \\ \frac{dq}{dr} &= \frac{1}{2} \left[\frac{q_{j+1} - q_j}{\beta_j \Delta y_j} + \frac{q_j - q_{j-1}}{\Delta y_j} \right]\end{aligned}\tag{B-11}$$

where

$$\Delta y_j = y_j - y_{j-1}$$

$$\beta_j = \frac{y_{j+1} - y_j}{y_j - y_{j-1}}$$

Substituting Eqs. (B-11), into (B-10) we get ,

$$\begin{aligned}& \frac{2}{\Delta y_j (1 + \beta_j)} \left[\frac{q_{j+1} - q_j}{\beta_j \Delta y_j} - \frac{q_j - q_{j-1}}{\Delta y_j} \right] - \left(\frac{9}{4} \kappa^2 + \frac{1}{y^2} \right) q_j = \\ & 1.5 \kappa_j \left(\frac{e_{j+1} - e_j}{\beta_j \Delta y_j} + \frac{e_j - e_{j-1}}{\Delta y_j} \right) - \frac{1}{2r} \left(\frac{q_{j+1} - q_j}{\beta_j \Delta y_j} + \frac{q_j - q_{j-1}}{\Delta y_j} \right)\end{aligned}\tag{B-12}$$

taking q_{j+1} , q_j , q_{j-1} on one side we get,

$$\begin{aligned}& \left[\frac{2}{\Delta y^2 (1 + \beta_j) \beta_j} + \frac{1}{2y \beta_j \Delta y_j} \right] q_{j+1} - \left[\frac{2}{\Delta y_j (1 + \beta_j)} \left(\frac{1}{\beta_j \Delta y_j} + \frac{1}{\Delta y_j} \right) + \frac{9}{4} \kappa^2 + \frac{1}{y^2} \right] q_j \\ & - \frac{1}{2} \left[\frac{1}{\beta_j \Delta y_j} - \frac{1}{\Delta y_j} \right] q_j + \left(\frac{2}{\Delta y_j (1 + \beta_j)} - \frac{1}{2y \Delta y_j} \right) q_{j-1} = 1.5 \kappa_j \left(\frac{e_{j+1} - e_j}{\beta_j \Delta y_j} + \frac{e_j - e_{j-1}}{\Delta y_j} \right)\end{aligned}\tag{B-13}$$

This along with the two boundary condition form a tridiagonal system which can be efficiently solved by the Thomas algorithm

PAGE _____ INTENTIONALLY BLANK

APPENDIX C

EXPONENTIAL KERNAL APPROXIMATION

The Integro - differential governing equation for radiative flux for parallel plate geometry, gray non-scattering medium with black bounding surfaces is given by

$$q_r(y) = e_{1\omega} - e_{2\omega} + \frac{3}{2} \int_0^y F_{1\omega}(t) \kappa_\omega \exp \left[-\frac{3}{2} \kappa_\omega (t - y) \right] dt$$
(C-1)

$$- \frac{3}{2} \int_y^L F_{2\omega}(t) \kappa_\omega \exp \left[-\frac{3}{2} \kappa_\omega (t - y) \right] dt$$

or it can also be written as

$$q_r(y) = 2\sigma T_1^4 F_2(y) - 2\sigma T_2^4 F_2(L - y) + 2\sigma \int_0^y T^4(t) \kappa_\omega F_1(y - t) dt$$
(C-2)

$$- 2\sigma \int_y^L T^4(t) \kappa_\omega F_1(t - y) dt$$

For Exponential Kernal approximation let

$$F_1(t) = \frac{3}{4} \kappa_\omega e^{-\frac{3}{2}t} \quad ; \quad F_2(t) = \frac{1}{2} \kappa_\omega e^{-\frac{3}{2}t}$$
(C-3)

Substituting Eq. (C-3) into Eq. (C-2) we get

$$q_r(y) = \sigma T_1^4 e^{-\frac{3}{2}\kappa_\omega y} - \sigma T_2^4 e^{-\frac{3}{2}\kappa_\omega(L-y)} + \frac{3}{2}\kappa_\omega \left\{ \left[\int_0^y T^4(t) e^{-\frac{3}{2}\kappa_\omega(y-t)} dt \right] - \left[\int_y^L T^4(t) e^{-\frac{3}{2}\kappa_\omega(t-y)} dt \right] \right\} \quad (C-4)$$

or

$$q_r(y) = F(y) + \lambda \left\{ \int_0^y T^4(t) e^{-\beta(y-t)} dt - \int_y^L T^4(t) e^{-\beta(t-y)} dt \right\}$$

where

$$F(y) = \sigma T_1^4 e^{-\beta y} - \sigma T_2^4 e^{-\beta(L-y)}$$

$$\beta = \frac{3}{2}\kappa_\omega \quad ; \quad \lambda = \beta\sigma = \frac{3}{2}\kappa_\omega\sigma$$

differentiating Eq. (C-4)

$$\begin{aligned} \frac{dq_r}{dy} = \frac{dF}{dy} + \lambda \left\{ \left[T^4(y) - 0 + \int_0^y T^4(t) e^{-\beta(y-t)} (-\beta) dt \right] \right. \\ \left. - \left[0 - T^4(y) + \int_y^L T^4(t) e^{-\beta(t-y)} (\beta) dt \right] \right\} \end{aligned} \quad (C-5)$$

Simplifying we get ;

$$\begin{aligned}
\frac{dq_r}{dy} &= \frac{dF}{dy} + 2\lambda T^4(y) + \lambda\beta \left\{ - \int_0^y T^4(t) e^{-\beta(y-t)} dt - \int_y^L T^4(t) e^{-\beta(t-y)} dt \right\} \\
&= \frac{dF}{dy} + 2\lambda T^4(y) - \beta\lambda \left\{ \int_0^y T^4(t) e^{-\beta(y-t)} dt + \int_y^L T^4(t) e^{-\beta(t-y)} dt \right\}
\end{aligned}
\tag{C-6}$$

where

$$\beta\lambda = \beta^2\sigma = \frac{9}{4}\sigma$$

Differentiating once again we get ;

$$\begin{aligned}
\frac{d^2q}{dy^2} &= \frac{d^2F}{dy^2} + 2\lambda \frac{dT^4}{dy} \beta\lambda \left\{ \left[T^4(y) - 0 + \int_0^y T^4(t) e^{-\beta(y-t)} (-\beta) dt \right] \right. \\
&\quad \left. + \left[0 - T^4(y) + \int_y^L T^4(t) e^{-\beta(t-y)} (+\beta) dt \right] \right\}
\end{aligned}
\tag{C-7}$$

Simplifying Eq. (C-7) results in,

$$\frac{d^2q_r}{dy^2} = \frac{d^2F}{dy^2} + 2\lambda \frac{dT^4}{dy} + \beta\lambda \left\{ \beta \int_0^y T^4(t) e^{-\beta(y-t)} dt - \beta \int_y^L T^4(t) e^{-\beta(t-y)} dt \right\}
\tag{C-8}$$

Eliminating the integrals between Eq. (C-8), one obtains

$$\begin{aligned} \frac{d^2 q_r}{dy^2} &= \frac{d^2 F}{dy^2} + 2\lambda \frac{dT^4}{dy} + \beta^2 [q_r(y) - F(y)] \\ \text{or} \\ \frac{d^2 q_r}{dy^2} - \beta^2 q_r(y) &= 2\lambda \frac{dT^4}{dy} + \frac{d^2 F}{dy^2} - \beta^2 F(y) \end{aligned} \quad (C-9)$$

For the specific case

$$F(y) = \sigma T_1^4 e^{-\beta y} - \sigma T_2^4 e^{-\beta(L-y)} ; \quad \beta = \frac{3}{2} \kappa_\omega$$

$$\frac{dF}{dy} = -\beta \sigma T_1^4 e^{-\beta y} - \sigma \beta T_2^4 e^{-\beta(L-y)} \quad (C-10)$$

$$\frac{d^2 F}{dy^2} = \beta^2 \sigma T_1^4 e^{-\beta y} - \beta^2 \sigma T_2^4 e^{-\beta(L-y)}$$

Thus

$$\frac{d^2 F}{dy^2} - \beta^2 F(y) = 0 \quad (C-11)$$

therefore the governing becomes

$$\frac{1}{\kappa_\omega^2} \frac{d^2 q_r(y)}{dy^2} - \frac{9}{4} q_r(y) = 3 \frac{\sigma}{\kappa_\omega} \frac{dT^4}{dy} \quad (C-12)$$

Since $e = \sigma T^4$

$$\frac{1}{\kappa_\omega^2} \frac{d^2 q_r(y)}{dy^2} - \frac{9}{4} q_r(y) = \frac{1}{\kappa_\omega} \frac{de(y)}{dy} \quad (C-13)$$

APPENDIX D

COMPONENTS OF THE JACOBIAN MATRIX

The material presented in this appendix is taken directly from Ref. 27. In this appendix, the species matrix in the left hand side bracket of Eq. (4-9) is evaluated. The source term is a function of density, temperature and various species. In evaluating $\frac{\partial H}{\partial t}$, the density and temperature dependency is neglected for computational efficiency. The components of the Jacobian matrix are as follows :

$$H_i = \dot{W}_i = \dot{C}_i M_i$$

$$C_i = (\rho f_i / m_i) \times 10^{-3} \frac{\text{gm} - \text{mol}}{\text{cm}^3}$$

$$\frac{\partial \dot{W}_{O_2}}{\partial U_{O_2}} = -K_{f_1} C_{H_2}$$

$$\frac{\partial \dot{W}_{O_2}}{\partial U_{H_2O}} = 0 \quad (D-1)$$

$$\frac{\partial \dot{W}_{O_2}}{\partial U_{H_2}} = -K_{f_1} C_{O_2}$$

$$\frac{\partial \dot{W}_{O_2}}{\partial U_{OH}} = 2K_{b_1} \frac{M_{O_2}}{M_{OH}} C_{OH}$$

$$\frac{\partial \dot{W}_{H_2}}{\partial U_{O_2}} = -K_{f_1} \frac{M_{H_2}}{M_{O_2}} C_{H_2}$$

$$\frac{\partial \dot{W}_{H_2}}{\partial U_{H_2}} = -K_{f_1} C_{O_2} - K_{f_2} C_{OH}^2$$

$$\frac{\partial \dot{W}_{H_2}}{\partial U_{H_2O}} = 2K_{b_2} \frac{M_{H_2}}{M_{H_2O}} C_{H_2O}$$

$$\frac{\partial \dot{W}_{H_2}}{\partial U_{OH}} = 2K_{b_1} \frac{M_{H_2}}{M_{OH}} C_{OH} - 2K_{f_2} \frac{M_{H_2}}{M_{OH}} C_{OH} C_{H_2}$$

$$\frac{\partial \dot{W}_{H_2O}}{\partial U_{O_2}} = 0$$

$$\frac{\partial \dot{W}_{H_2O}}{\partial U_{H_2O}} = -4K_{b_2} C_{H_2O}$$

$$\frac{\partial \dot{W}_{H_2O}}{\partial U_{H_2}} = 2K_{f_2} \frac{M_{H_2O}}{M_{H_2}} C_{OH}^2$$

(D-2)

$$\frac{\partial \dot{W}_{H_2O}}{\partial U_{OH}} = 4K_{f_2} \frac{M_{H_2O}}{M_{H_2}} C_{OH} C_{H_2}$$

$$\frac{\partial \dot{W}_{OH}}{\partial U_{O_2}} = 2K_{f_2} \frac{M_{OH}}{M_{O_2}} C_{H_2}$$

$$\frac{\partial \dot{W}_{OH}}{\partial U_{H_2O}} = 4K_{b_2} \frac{M_{OH}}{M_{H_2O}} C_{H_2O}$$

$$\frac{\partial \dot{W}_{OH}}{\partial U_{H_2}} = 2K_{f_1} \frac{M_{OH}}{M_{H_2}} C_{O_2} - 2K_{f_2} \frac{M_{OH}}{M_{H_2}} C_{OH}^2$$

$$\frac{\partial \dot{W}_{OH}}{\partial U_{OH}} = -4K_{b_2} C_{OH} - 4K_{F_2} C_{OH} C_{H_2}$$

APPENDIX E

PROGRAM FOR THE CALCULATION OF PLANCK MEAN ABSORPTION COEFFICIENT

```
c*****
c Program To Calculate Kappa ( Kp ) For different gases
c Provision is made for calculating Kp for H2O, OH, NO
c Various combination of these gases can be taken and Kp
c can be determined
c*****

      Program Kappa

      parameter(ix=31,iy=31,iq=12,is=9,ip=10,im=8,ir=18)

      common/rad/omega(7),sk1(ix,iy),sk2(ix,iy),phi7(ix,iy),
&eo(ix,iy,7),co2(ix,iy,7),rkpt(ix,iy),
&ao(ix,iy,7),uc(ix,iy,5),rkp(ix,iy,7),cc(52,52),
&aa(52,52),bb(52,52),b2(ix,iy,5),et(ix,iy),btn(ix,iy),
&psp(ix,iy,is),rsp(5),dd(52,52),qrx(ix,iy),qry(ix,iy),
&rkpt1(ix,iy),rkpt2(ix,iy),phiv(ix,iy,is),fn(ix,iy,is)

      dimension cstop(ix,iy)

      dimension irror(100,2),an(31,31),bn(31,31),cn(31,31)

      dimension dn(31,31),r(31,31),pn(31,31),rhon(31,31)
```

```

integer bt1, bt2, bt3, bt4
open(unit=26, file='trash')
do 1 izz=1, 31
  r(izz, 1)=8314.34
  btn(izz, 1)=izz*150
  fn(izz, 1, 1)=0.0
  fn(izz, 1, 2)=0.0
  fn(izz, 1, 3)=0.99
  fn(izz, 1, 4)=0.00
  fn(izz, 1, 5)=0.0
  fn(izz, 1, 6)=0.0
  fn(izz, 1, 7)=0.00
  fn(izz, 1, 8)=0.00
  fn(izz, 1, ncs)=0.01
  pn(izz, 1)=101325.
  rhon(izz, 1)=pn(izz, 1)/(r(izz, 1)*btn(izz, 1))
1 continue
  nnx=ix
  nn=iy
  nxpl=ix-1
  nypl=iy-1
  ixj=ix
  iyj=iy
  izz=31
  nxpl = nnx+1

```

```

        nyp1 = nny+1

c
c-----initialize omega (wave no. for planck's formula)
c-----at band center
c

        omega(1) = 500.
        omega(2) = 1600.
        omega(3) = 3750.
        omega(4) = 5350.
        omega(5) = 7250.
        omega(6) = 3570.
        omega(7) = 1876
        soh = 110. * 10000./101325.

c
c-----initializing for band absorption
c

        eh = 6.625e-27
        c = 2.998e+10
        urk = 1.380e-16
        gg1 = 3652.
        g2 = 1595.
        g3 = 3756.
        c1 = 3.1415926 * 2. * eh * (c**2.)
        c2 = eh * c/urk
        v1 = 1.

```

```

v2 = 0.
v3 = 1.
epsi = 1.
depsi = 1./epsi
do 88890 izz=1,ixj
sk1(izz,1) = (btn(izz,1)/300.)**0.5
sk2(izz,1) = (300./(btn(izz,1)))**1.5
b2(izz,1,1) = .073/sk1(izz,1)
b2(izz,1,2) = .130/sk1(izz,1)
b2(izz,1,3) = .145/sk1(izz,1)
b2(izz,1,4) = .118/sk1(izz,1)
b2(izz,1,5) = .201/sk1(izz,1)
88890 continue
do 88960 izz=1,ixj
phi7(izz,1) = (btn(izz,1)/100.)**(-0.5)
phi7(izz,1) = -17.6 * phi7(izz,1)
phi7(izz,1) = exp(phi7(izz,1))
88960 continue
do 88990 izz=1,ixj
phiv(izz,1,1) = (-eh*c*gg1)/(btn(izz,1)*urk)
phiv(izz,1,1) = exp(phiv(izz,1,1))
phiv(izz,1,1) = 1.-phiv(izz,1,1)
88990 continue
do 89020 izz=1,ixj
phiv(izz,1,2) = (-eh*c*g2)/(btn(izz,1)*urk)

```

```

        phiv(izz,1,2) = exp(phiv(izz,1,2))
        phiv(izz,1,2) = 1.-phiv(izz,1,2)
89020 continue
        do 89050 izz=1,ixj
            phiv(izz,1,3) = (-eh*c*g3)/(btn(izz,1)*urk)
            phiv(izz,1,3) = exp(phiv(izz,1,3))
            phiv(izz,1,3) = 1.-phiv(izz,1,3)
89050 continue
c
c-----calculate denominator of phi-101
c
        do 89080 izz=1,ixj
            phiv(izz,1,1) = (phiv(izz,1,1) * phiv(izz,1,2)
            &* phiv(izz,1,3))
89080 continue
c
c-----calculate numerator of phi-101
c
        do 89090 izz=1,ixj
            phiv(izz,1,2) = (-eh*c*(v1*gg1+v2*g2+v3*g3))/
            &(btn(izz,1)*urk)
            phiv(izz,1,2) = exp(phiv(izz,1,2))
            phiv(izz,1,2) = 1.-phiv(izz,1,2)
89090 continue
c

```

c-----calculate phi-101

c

do 89120 izz=1,ixj

phiv(izz,1,3) = phiv(izz,1,2)/phiv(izz,1,1)

89120 continue

do 2 k=1,7

do 89130 izz=1,ixj

eo(izz,1,k) = c2 * omega(k) /btn(izz,1)

eo(izz,1,k) = exp(eo(izz,1,k))

eo(izz,1,k) = c1 * (omega(k)**3.)/(eo(izz,1,k)-1.)

eo(izz,1,k) = eo(izz,1,k) * 1.0e-05

89130 continue

2 continue

do 89170 izz=1,ixj

co2(izz,1,1) = 771. * sk2(izz,1) * phi7(izz,1)

co2(izz,1,2) = 3.35 * sk2(izz,1)

co2(izz,1,3) = 1.52 * sk2(izz,1)

co2(izz,1,4) = 0.276 * sk2(izz,1) * phiv(izz,1,3)

co2(izz,1,5) = .230 * sk2(izz,1) * phiv(izz,1,3)

89170 continue

c

c-----unit change

c

do 9 k=1,5

do 89220 izz=1,ixj

```

        co2(izz,1,k) = (100./101325.) * co2(izz,1,k)
        co2(izz,1,k) = co2(izz,1,k)
89220 continue
      9 continue
        izz = izz
        do 89230 izz=1,ixj
          if(.not.(fn(izz+1,2,3).le.0.)) go to 89230
          fn(izz+1,2,3) = 0.0001
89230 continue
        izz = izz
        do 89240 izz=1,ixj
          psp(izz,1,3) = rhon(izz,1)*fn(izz,1,3)*r(izz,1)
          & *btn(izz,1)
          psp(izz,1,3) = 1.
          psp(izz,1,4) = rhon(izz,1)*fn(izz,1,4)*r(izz,1)
          & *btn(izz,1)
          psp(izz,1,5) = rhon(izz,1)*fn(izz,1,8)*r(izz,1)
          & *btn(izz,1)
89240 continue
      c
      c-----calculate  ao
      c
        do 89260 izz=1,ixj
          ao(izz,1,1) = 49.4 * sk1(izz,1)
          ao(izz,1,2) = 90.1 * sk1(izz,1)

```

```

        ao(izz,1,3) = 112.6 * sk1(izz,1)
        ao(izz,1,4) = 79.7 * sk1(izz,1)
        ao(izz,1,5) = 79.7 * sk1(izz,1)
89260 continue
c
c-----change unit
c
        do 4 k=1,5
        do 89310 izz=1,ixj
        ao(izz,1,k) = ao(izz,1,k) * 100.
        ao(izz,1,k) = ao(izz,1,k)
89310 continue
        4 continue
c
c-----Calculating Kp for various gases and their combination
c
        do 89320 izz=1,ixj
        et(izz,1) = 5.668e-05*btn(izz,1)**4.
        rkpt(izz,1) = 0.
89320 continue
        do 3 k=1,5
        do 89340 izz=1,ixj
        co2(izz,1,6)=110.*300./(10*btn(izz,1))
        ao(izz,1,6)=1.
        co2(izz,1,7)=132.*300./(10.*btn(izz,1))

```



```

      ao(izz,1,7)=1.
      rkpt(izz,1,k) = eo(izz,1,k)*ao(izz,1,k)*co2(izz,1,k)
      rkpt(izz,1) = rkpt(izz,1) + rkpt(izz,1,k)
      rkpt1(izz,1)=eo(izz,1,6)*ao(izz,1,6)*co2(izz,1,6)
      rkpt2(izz,1)=eo(izz,1,7)*ao(izz,1,7)*co2(izz,1,7)
89340 continue
      3 continue
      do 89360 izz=1,ixj
      rkpt(izz,1) = rkpt(izz,1)*psp(izz,1,3)/et(izz,1)
      rkpt1(izz,1) = rkpt1(izz,1)*psp(izz,1,4)/et(izz,1)
      rkpt2(izz,1) = rkpt2(izz,1)*psp(izz,1,5)/et(izz,1)
      rkpt(izz,1)=rkpt(izz,1)+rkpt2(izz,1)
      write(26,20)btn(izz,1),rkpt(izz,1)
      20 format(2x,f10.4,2x,e20.6)
89360 continue
      stop
      end

```

PAGE _____ INTENTIONALLY BLANK



AIAA-91-0373

Radiative Interactions in a Hydrogen-Fueled Supersonic Combustor

R. Chandrasekhar and S. N. Tiwari,
Old Dominion University,
Norfolk, VA

J. P. Drummond,
NASA Langley Research Center,
Hampton, VA

29th Aerospace Sciences Meeting

January 7-10, 1991/Reno, Nevada

~~INTENTIONALLY BLANK~~

RADIATIVE INTERACTIONS IN A HYDROGEN-FUELED SUPERSONIC COMBUSTOR

R. Chandrasekhar* and S. N. Tiwari†
Old Dominion University, Norfolk, VA 23529-0247
and

J. P. Drummond‡
NASA-Langley Research Center, Hampton, VA 23665

Abstract

The two-dimensional, elliptic Navier-Stokes equations are used to investigate supersonic flows with finite-rate chemistry and radiation, for hydrogen-air systems. The chemistry source term in the species equation is treated implicitly to alleviate the stiffness associated with fast reactions. The explicit, unsplit MacCormack finite-difference scheme is used to advance the governing equations in time, until convergence is achieved. The specific problem considered is the premixed flow in a channel with a ten-degree compression ramp. Three different chemistry models are used, accounting for increasing number of reactions and participating species. Two chemistry models assume nitrogen as inert, while the third model accounts for nitrogen reactions and NO_x formation. The tangent slab approximation is used in the radiative flux formulation. A pseudo-gray model is used to represent the absorption-emission characteristics of the participating species. Results obtained for specific conditions indicate that the radiative interactions vary substantially, depending on reactions involving HO_2 and NO species, and that this can have a significant influence on the flowfield.

Nomenclature

A band absorptance, m^{-1}
 A_w band width parameter, m^{-1}
 C_j concentration of the j^{th} species, $\text{kg-mole}/\text{m}^3$
 C_p constant pressure specific heat, $\text{J}/\text{kg-K}$
 C_w correlation parameter, $(\text{N}/\text{m}^2)^{-1}\text{m}^{-1}$
 E total internal energy
 e_w Planck's function
 f_j mass fraction of j^{th} species
 H total enthalpy, J/kg
 h static enthalpy, J/kg
 k thermal conductivity

k_b backward rate constant
 k_f forward rate constant
 P pressure, N/m^2
 P_j partial pressure of j^{th} species
 q_R total radiative flux
 R gas constant
 S integrated band intensity, $(\text{N}/\text{m}^2)^{-1}\text{m}^{-2}$
 T temperature, K
 u, v velocity in x - and y - directions, m/s
 \dot{w}_j production rate of j^{th} species, $\text{kg}/\text{m}^3\text{-s}$
 x, y physical coordinates
 γ ratio of specific heats
 κ_p Planck mean absorption coefficient
 λ second coefficient of viscosity, wavelength
 μ dynamic viscosity, $\text{kg}/\text{m-s}$
 ξ, η computational coordinates
 ρ density
 σ Stefan - Boltzmann constant
 τ shear stress
 ϕ equivalence ratio
 ω wave number, m^{-1}

Introduction

In recent years there has been a renewed interest in the development of a hypersonic transatmospheric aerospace vehicle capable of flying at sub-orbital speeds. A hydrogen-fueled supersonic combustion ramjet (scramjet) engine is a strong candidate for propelling such a vehicle. For a better understanding of the complex flowfield in different regions of the engine, both experimental and computational techniques are employed. Several computer programs have been developed [1-4] and applied to gain more insight into the problem involving the flow in the various sections of the scramjet module.

The combustion of hydrogen and air in the scramjet combustor results in absorbing-emitting gases such as water vapor and hydroxyl radicals. Existence of such gases makes the study of radiation heat transfer an important issue. There are several models available in the literature to represent the absorption-emission characteristics of molecular gases [5-10]. One- and two-dimensional radiative heat transfer equations for various flow and combustion related problems are available [11-19]. In earlier studies [16,18,19], both pseudo-gray and nongray gas models were employed to evaluate radiative heat transfer for chemically reacting supersonic

* Graduate Research Assistant, Department of Mechanical Engineering and Mechanics. Student Member AIAA.

† Eminent Professor, Department of Mechanical Engineering and Mechanics. Associate Fellow AIAA.

‡ Senior Research Scientist, Theoretical Flow Physics Branch, Fluid Mechanics Division. Associate Fellow AIAA.

Copyright © 1990 by the American Institute of Aeronautics and Astronautics, Inc. All rights reserved.

flow. Results of both models were compared and the pseudo-gray model was found to be computationally more efficient.

Considerable work has been carried out in the past decade to model the chemical kinetic mechanism of the hydrogen-air system. A most complete model would involve some 60 reaction paths [20], rendering numerical solution very difficult, if not impossible. A two-step chemistry model, has been used for computing supersonic combustion [4, 16, 18, 19]. This model has only four species and two reaction paths, and is useful for preliminary studies. However, there are several limitations to this model, such as ignition-phase inaccuracy (i.e. a much shorter ignition delay) and also, overprediction of flame temperature and longer reaction times. Recent improvements in this area include a 8-species, 14-reaction model [21] and a 9-species, 18-reaction model [2, 22]. While none of these aforementioned models account for nitrogen reactions (assuming nitrogen as inert), recent developments in this area include a 15-species, 35-reaction model which accounts for NO_x formation and other nitrogen reactions in the hydrogen-air system [22].

The objectives of the present study are to extend the radiative heat transfer formulation used with the global two-step chemistry model [18, 19], to the more complete models namely the 9-species, 18-reaction model as well as the 15-species, 35-reaction model. The effect of radiative heat transfer in both transverse and streamwise directions is investigated. The finite-difference method using the explicit, unsplit MacCormack scheme [23] is used to solve the governing equations.

The flowfield in the combustor is represented by the Navier-Stokes equations and by the appropriate species continuity equations [2, 3]. Incorporation of the finite-rate chemistry models into the fluid dynamic equations can create a set of stiff differential equations. Stiffness is due to a disparity in the time scales of the governing equations. In the time accurate solution, after the fast transients have decayed and the solutions are changing slowly, taking a larger time step is more efficient. But explicit methods still require small time steps to maintain stability. One way around this problem is to use a fully implicit method. However, this requires the inversion of a block multi-diagonal system of algebraic equations, which is also computationally expensive. The use of a semi-implicit technique, suggested by several investigators [24-26], provides an alternative to the above problems. This method treats the source term (which is the cause of the stiffness) implicitly, and solves the remaining terms explicitly.

Basic Governing Equations

The physical model for analyzing the flowfield in a supersonic combustor is described by the Navier-

Stokes and species continuity equations. For two-dimensional flows, these equations are expressed in physical coordinates as,

$$\frac{\partial U}{\partial t} + \frac{\partial F}{\partial x} + \frac{\partial G}{\partial y} + H = 0 \quad (1)$$

where vectors U , F , G and H are written as,

$$U = \begin{bmatrix} \rho \\ \rho u \\ \rho v \\ \rho E \\ \rho f_j \end{bmatrix}$$

$$F = \begin{bmatrix} \rho u \\ \rho u^2 + p + \tau_{xx} \\ \rho uv + \tau_{xy} \\ (\rho E + p)u + \tau_{xx}u + \tau_{xy}v + q_{cx} + q_{Rx} \\ \rho u f_j - \rho D \frac{\partial f_j}{\partial x} \end{bmatrix}$$

$$G = \begin{bmatrix} \rho v \\ \rho uv + \tau_{yx} \\ \rho v^2 + p + \tau_{yy} \\ (\rho E + p)v + \tau_{xy}v + \tau_{yy}v + q_{cy} + q_{Ry} \\ \rho v f_j - \rho D \frac{\partial f_j}{\partial y} \end{bmatrix}$$

$$H = \begin{bmatrix} 0 \\ 0 \\ 0 \\ 0 \\ -\dot{w}_j \end{bmatrix}$$

The viscous stress tensors in the F and G terms are given as,

$$\tau_{xx} = -\lambda \left(\frac{\partial u}{\partial x} + \frac{\partial v}{\partial y} \right) - 2\mu \frac{\partial u}{\partial x} \quad (2a)$$

$$\tau_{xy} = -\mu \left(\frac{\partial u}{\partial x} + \frac{\partial v}{\partial y} \right) \quad (2b)$$

$$\tau_{yy} = -\lambda \left(\frac{\partial u}{\partial x} + \frac{\partial v}{\partial y} \right) - 2\mu \frac{\partial v}{\partial y} \quad (2c)$$

where $\lambda = -\frac{2}{3}\mu$. The quantities q_{cx} and q_{cy} in the F and G terms are the components of the conduction heat flux and are expressed as

$$q_{cx} = -k \frac{\partial T}{\partial x}$$

$$q_{cy} = -k \frac{\partial T}{\partial y} \quad (3)$$

The molecular viscosity μ is evaluated from the Sutherland's formula. The total internal energy E in Eq. (2) is given by

$$E = -\frac{p}{\rho} + \frac{u^2 + v^2}{2} + \sum_{j=1}^m h_j f_j \quad (4)$$

Specific relations are needed for the chemistry and radiative flux terms. These are discussed in the following sections.

Chemistry and Thermodynamic Model

Chemical reaction rate expressions are usually determined by summing the contributions from each relevant reaction path to obtain the total rate of change of each species. Each path is governed by a law of mass action expression in which the rate constants can be determined from a temperature dependent Arrhenius expression. The reaction mechanism is expressed in a general form as

$$\sum_{j=1}^{ns} \gamma'_{ij} C_j \xrightleftharpoons[k_{b,i}]{k_{f,i}} \sum_{j=1}^{ns} \gamma''_{ij} C_j, \quad i = 1, nr \quad (5)$$

where ns = number of species and nr = number of reactions. The chemistry source terms \dot{w}_j in Eq. (1) are obtained, on a mass basis, by multiplying the molar changes and corresponding molecular weight as

$$\dot{w}_j = M_j C_j = M_j \sum_{i=1}^{nr} (\gamma''_{ij} - \gamma'_{ij}) \left[k_{f,i} \prod_{m=1}^{ns} C_m^{\gamma'_{im}} \right] \left[-k_{b,i} \prod_{m=1}^{ns} C_m^{\gamma''_{im}} \right], \quad j = 1, ns \quad (6)$$

The reaction rate constants $k_{f,i}$ and $k_{b,i}$ appearing in Eqs. (5) and (6) are determined from an Arrhenius rate expression as

$$k_{f,i} = A_i T^N \exp\left(-\frac{E_i}{RT}\right) \quad (7)$$

where,

$$k_{b,i} = \frac{k_{f,i}}{K_{eq,i}} \quad (8)$$

$$K_{eq,i} = \left(\frac{1}{RT}\right)^{\Delta n} \exp\left(\frac{-\Delta G_{R,i}}{RT}\right) \quad (9)$$

The coefficients A , N and E appearing in Eq. (7) are given in Table 1. The term Δn in Eq. (9) denotes the difference in the number of moles of reactants and products.

The Gibbs energy term in Eq. (9) is calculated as

$$\Delta G_{R,i} = \sum_{j=1}^{ns} \gamma''_{ij} g_j - \sum_{j=1}^{ns} \gamma'_{ij} g_j, \quad j = 1, nr \quad (10)$$

$$\frac{g_j}{R} = A_j(T - \ln T) + \frac{B_j}{2} T^2 + \frac{C_j}{6} T^3 + \frac{D_j}{12} T^4 + \frac{E_j}{20} T^5 + F_j + G_j T \quad (11)$$

The gas constant for the mixture is evaluated by a mass-weighted summation over all species as

$$\bar{R} = \sum_{j=1} f_j R_j \quad (12)$$

$$P = \rho \bar{R} T \quad (13)$$

Radiation Transfer Model

Evaluation of the energy equation presented in Eq. (1) requires an appropriate expression for the radiative flux term, q_R . Therefore, a suitable radiative transport model is needed. Various models are available in the literature to represent the absorption-emission characteristics of the molecular species [10]. The equations of radiative transport are expressed generally in integro-differential forms. The integration involves both the frequency spectrum and physical coordinates. In many realistic three-dimensional physical problems, the complexity of the radiative transport equations can be reduced by introduction of the tangent-slab approximation. This approximation treats the gas layer as a one-dimensional slab in evaluation of the radiative flux (Fig. 1).

Detailed derivations of radiative flux equations for gray as well as nongray radiation have been carried out previously [15, 19]. For a multiband gaseous system, the nongray radiative flux in the normal direction is expressed as

$$q_R(y) = e_1 - e_2 + \sum_{i=1}^n A_i \left\{ \int_0^y \left[\frac{de_{\omega_i}(z)}{dz} \right] x \right. \\ \left. \tilde{A}_i \left[\frac{3}{2} \frac{u_{0i}}{L} (y - z) \right] dz + \right. \\ \left. + \int_y^L \left[\frac{de_{\omega_i}(z)}{dz} \right] \tilde{A}_i \left[\frac{3}{2} \frac{u_{0i}}{L} (z - y) \right] dz \right\} \quad (14)$$

The information on the band absorptance \tilde{A}_i and other quantities is available in the cited references.

For a gray medium, the spectral absorption coefficient κ_ω is independent of the wave number, and an expression for the radiative flux is obtained as [5, 16, 19]

$$q_R(y) = e_1 - e_2 + \frac{3}{2} \left\{ \int_0^y [e(z) - e_1] e^{-\frac{3u(y-z)}{2L} \kappa dz} \right. \\ \left. - \int_y^L [e(z) - e_2] e^{-\frac{3u(y-z)}{2L} \kappa dz} \right\} \quad (15)$$

It is computationally more efficient to use Eq. (15) in the general energy equation than Eq. (14). This is because by differentiating Eq. (15) twice (using the Leibnitz formula) the integrals are eliminated and the following inhomogenous ordinary differential equation is obtained :

$$\frac{1}{\kappa^2} \frac{d^2 q_R(y)}{dy^2} - \frac{9}{4} q_R(y) = \frac{3}{\kappa} \frac{de(y)}{dy} \quad (16)$$

The solution of Eq. (16) requires two boundary conditions which are given for non-black diffuse surfaces as [5]

$$\left(\frac{1}{\epsilon_1} - \frac{1}{2} \right) [q_R(y)]_{y=0} - \frac{1}{3\kappa} \left[\frac{dq_R}{dy} \right]_{y=0} = 0 \quad (17a)$$

$$\left(\frac{1}{\epsilon_2} - \frac{1}{2} \right) [q_R(y)]_{y=L} + \frac{1}{3\kappa} \left[\frac{dq_R}{dy} \right]_{y=L} = 0 \quad (17b)$$

For black surfaces $\epsilon_1 = \epsilon_2 = 1$ and Eqs. (17) reduce to simpler forms.

An appropriate model for a gray gas absorption coefficient is required in Eqs. (15) — (17). This is represented by the Planck mean absorption coefficient, which is expressed for a multi-band system as [5, 19]

$$\kappa = \kappa_P = \frac{P_j}{\sigma T^4(y)} \sum_{i=1}^n e_{\omega_i}(T) S_i(T) \quad (18)$$

It should be noted that κ_P is a function of the temperature and the partial pressures P_j of the species.

Method of Solution

The governing equations are transformed from the physical domain (x, y) to a computational domain (ξ, η) , using an algebraic grid generation technique similar to the one used by Smith and Weigel [27]. In the computational domain, Eq. (1) is expressed as

$$\frac{\partial \hat{U}}{\partial t} + \frac{\partial \hat{F}}{\partial \xi} + \frac{\partial \hat{G}}{\partial \eta} + \hat{H} = 0 \quad (19)$$

where

$$\begin{aligned} \hat{U} &= UJ, \quad \hat{F} = Fy_\eta - Gx_\eta \\ \hat{G} &= Gx_\xi - Fy_\xi, \quad \hat{H} = HJ \\ J &= x_\xi y_\eta - y_\xi x_\eta \end{aligned} \quad (20)$$

Once the temporal discretization has been performed, the resulting system is spatially differenced using the explicit, unsplit MacCormack predictor-corrector scheme [23]. This results in a spatially and temporally discrete, simultaneous system of equations at each grid point [25, 26]. Each simultaneous system is solved, subject to initial and boundary conditions, by using

the Householder technique [28, 29]. At the supersonic inflow boundary, all flow quantities are specified as freestream conditions. At the supersonic outflow boundary, non-reflective boundary conditions are used, i.e. all flow quantities are extrapolated from interior grid points. The upper and lower boundaries are treated as solid walls. This implies a non-slip boundary condition (i.e. zero velocities). The wall temperature and pressure are extrapolated from interior grid points. Initial conditions are obtained by specifying freestream conditions throughout the flowfield. The resulting set of equations is marched in time, until convergence is achieved. The details of the radiative flux formulation and method of solution are available in [19].

Results and Discussion

Based on the theory and computational procedures described previously, an algorithm has been developed to solve the two-dimensional Navier-Stokes equations for chemically reacting and radiating supersonic flows. The extent of radiative heat transfer in supersonic flows undergoing hydrogen-air chemical reactions, has been investigated using three chemical kinetics models, accounting for increasing number of reactions and participating species. For the temperature range considered in this study, the important radiating species are OH and H₂O. The gray gas formulations are based on the Planck mean absorption coefficient which accounts for the detailed information on different molecular bands. The radiative fluxes have been computed using this 'pseudo-gray' formulation. The justification for using this model is provided in [19].

The specific problem considered is the supersonic flow of premixed hydrogen and air (stoichiometric equivalence ratio $\phi = 1.0$) in a channel with a compression corner on the lower boundary (Fig. 2). The physical dimensions considered for obtaining results are $L = 2$ cm., $X_1 = 1$ cm., $X_2 = 2$ cm., $L_x = X_1 + X_2 = 3$ cm., and $\alpha = 10$ degrees. The flow is ignited by the shock from the compression corner. The inlet conditions which are representative of scramjet operating conditions, are $P_\infty = 1.0$ atm., $T_\infty = 900$ K and $M_\infty = 4.0$. This same flow has been computed by several CFD research groups [4, 18, 19, 21] as a benchmark case.

Figures 3–6 show the computed results using a 31×31 grid, for temperature and pressure as well as H₂O and OH species mass fractions, varying along x at the location $y = 0.02$ cm from the lower wall (boundary layer region). Figures 3 and 4 show the temperature and pressure profiles predicted by the three chemistry models. The temperatures in the boundary layer show a gradual increase (Fig. 3). The pressure profiles are plotted at $y = 0.13$ cm. (inviscid region) and show a sharp increase due to the shock (Fig. 4). The ignition-phase inaccuracies of the three chemistry models can

be seen in Figs. 5 and 6. The shock is occurring after $x / L_x = 0.3$. However, the 2-step model predicts ignition before the shock (shorter ignition delay) due to the high temperature in the boundary layer. On the other hand, the 18-step model predicts a longer ignition delay, at $x / L_x = 0.37$ (Fig. 5). The 35-step model's prediction of ignition delay appears to be an average of the other two models. Although the three models do not differ much in prediction of temperature and pressure profiles, they do differ significantly in predictions of species productions (Figs. 5, 6).

In order to resolve this discrepancy, a grid sensitivity study was carried out to examine whether the grid size affects the flow predictions. The results of three grid distributions 11×31 , 31×31 and 61×31 are shown in Fig. 7, and it appears that the 31×31 grid is sufficient for the present study.

The reason for the varying predictions of species production by the three models was further examined and the results are shown in Figs. 8 and 9. Figure 8 shows that the Reaction No. 8 in Table 1 is critical in determining the extent of chemical heat release and H_2O production. Reaction No. 8 deals with production of HO_2 radical. This reaction is absent from the 2-step model, while it is common to both the 18-step and 35-step models. Figure 8 shows that the 35-step model experiences nearly a 30% drop in temperature at the channel exit, when the rate of Reaction No. 8 is reduced by a factor of 1000 (effectively cutting off the production of the HO_2 radical). In contrast, the 18-step model shows a 15% drop in temperature, when subjected to the same reduction in rate of Reaction No. 8. This shows that the Reaction No. 8 controls the overall H_2O production occurring in Reaction Nos. 9-18 (Table 1). Due to the high temperatures (~ 3000 K) in the flowfield, there is a pool of highly reactive free radicals like H, O, etc. The HO_2 radical is converted to the very reactive OH radical, by the free radicals (Reaction Nos. 11 and 12). This establishes the HO_2 radical as a very important species in promoting flame propagation in hydrogen-air flames. A similar study has been carried out in [30]. Since the 2-step model does not have the HO_2 radical, it predicts lesser amounts of OH and H_2O .

It was necessary to determine the reason for the higher sensitivity of the 35-step model to the HO_2 radical, as compared to the 18-step model. Figure 9 shows that the Reaction Nos. 21 and 23 in Table 1 are critical in determining the extent of chemical heat release and H_2O production. Reaction Nos. 21 and 23 deal with production of the NO radical. These reactions are absent from the 2-step and 18-step models, whereas they play an important role in the 35-step model. Figure 9 shows that the 35-step model undergoes a 30% reduction in temperature, when the rates of Reaction Nos. 21 and 23 are reduced by a factor of 1000 (ef-

fectively cutting off the production of the NO radical). This is nearly the same reduction caused by reducing the rate of Reaction No. 8 by a factor of 1000. Due to the high temperatures in the flowfield, the usually inert nitrogen dissociates into the highly reactive N free radical. This free radical N is then oxidized in Reaction Nos. 21 and 23, thereby producing the NO radical. This NO radical converts the HO_2 radical into the highly reactive OH radical, through Reaction No. 29. This confirms that the NO radical is a very important species for flame propagation in a hydrogen-fueled supersonic combustor. Since the 35-step model has the NO radical, it predicts higher amounts of OH and H_2O than the 18-step model.

Based on the above understanding of the chemical kinetics of supersonic hydrogen-air flames, the radiative interactions were examined. Figure 10 shows the profiles of the normalized streamwise radiative flux q_{Rx} predicted by the three chemistry models, along the location $y = 0.02$ cm. from the lower wall. The q_{Rx} flux reduces towards the end of the channel due to cancellation of fluxes in positive and negative directions. It is seen from Fig. 10 that the 18-step and 35-step models predict significantly higher amounts (50% more and 100% more, respectively) of q_{Rx} than the 2-step model. This is because radiative heat transfer is a strong function of temperature, pressure and species concentrations. So the larger values of radiative fluxes are caused by higher amounts of H_2O concentrations, which in turn, depend on reactions involving HO_2 and NO species.

Figure 11 shows the variations of the normal radiative flux q_{Ry} along x , at the location $y = 0.02$ cm. These do not appear to vary significantly between the three chemistry models. However, in all three cases, the q_{Ry} value increases rapidly after the shock.

Figures 12-15 show the computed results for reacting flows with and without radiation, for the three chemistry models. It is seen that the 2-step model shows only slight effect of radiative interaction, as compared to the 18-step and 35-step models. The 18-step and 35-step models predict lower temperature and lower H_2O and OH concentrations after the shock. This is because of the q_{Rx} flux, which reduces the total energy. Comparison of results in Figs. 12-15 shows that the 35-step model exhibits stronger effect of radiative interactions, than the other two models.

For reacting flows without radiation, it was seen from Figs. 5 and 6 that the 18-step model had a longer ignition delay (ignition at $x / L_x = 0.37$), while the 35-step model had a shorter ignition delay (ignition at $x / L_x = 0.27$). Another effect of radiative interactions, seen in Fig. 14, is to nullify this difference in predictions of ignition delay. For both 18-step and 35-step models, with radiation, the ignition is seen to occur at

the same point, $x / L_x = 0.33$. No such effect is seen on the ignition characteristics of the 2-step model.

Conclusions

The two-dimensional, spatially elliptic Navier-Stokes equations have been used to obtain solutions for supersonic flows undergoing finite-rate chemical reactions along with radiative interactions. The specific problem considered is of the premixed flow in a channel with a ten-degree compression ramp. The inlet conditions used in the present study correspond to typical flow conditions of a scramjet engine. Three different chemistry models were used for parametric studies, accounting for increasing number of reactions and participating species. It is seen that the radiative interactions vary significantly, depending particularly on chemical reactions involving HO_2 and NO species. These reactions have a substantial effect on the flow-field, with regard to H_2O concentration, temperature and pressure. Also, it is observed that the difference in the ignition delays of two chemistry models involving HO_2 reactions is nullified as a result of radiative interaction. The results also show that the streamwise radiative flux reduces the temperature and concentration of species. This effect is a strong function of the amount of H_2O species concentration.

Acknowledgements

This work was supported by the NASA Langley Research Center through grants NAG-1-363 and NAG-1-423. The authors are grateful to Dr. M. H. Carpenter of NASA-LaRC, for providing details of the 35-step chemistry model.

References

1. Kumar, A., "Numerical Simulation of Scramjet Inlet Flowfield," NASA TP-25117, May 1986.
2. Drummond, J. P., Hussaini, M. Y. and Zang, T. A., "Spectral Methods for Modelling Supersonic Chemically Reacting Flowfields," *AIAA Journal*, Vol. 24, No. 9, September 1986, pp. 1461-1467; also Drummond, J. P., "Numerical Simulation of Supersonic Chemically Reacting Mixing Layers," Ph.D. Dissertation, George Washington University, May 1987.
3. Drummond, J. P., Rogers, R. C. and Hussaini, M. Y., "A Detailed Numerical Model of a Supersonic Reacting Mixing Layer," AIAA Paper No. 86-1427, June 1986.
4. Chitsomboon, T., Kumar, A., Drummond, J. P. and Tiwari, S. N., "Numerical Study of Supersonic Combustion Using a Finite-Rate Chemistry Model," AIAA Paper 86-0309, January 1986.
5. Sparrow, E. M. and Cess, R. D., "Radiation Heat Transfer," Brooks/Cole, Belmont, CA, 1966 and 1970. New Augmented Edition, Hemisphere Publ. Corp. Washington, D.C., 1978.
6. Tien, C. L., "Thermal Radiation Properties of Gases," *Advances in Heat Transfer*, Vol. 5, Academic Press, New York, 1968.
7. Cess, R. D. and Tiwari, S. N., "Infrared Radiative Energy Transfer in Gases," *Advances in Heat Transfer*, Vol. 8, Academic Press, New York, 1972.
8. Edwards, D. K., "Molecular Gas Band Radiation," *Advances in Heat Transfer*, Vol. 12, Academic Press, New York, 1976.
9. Tiwari, S. N., "Band Models and Correlations for Infrared Radiation," *Radiative Transfer and Thermal Control* (Progress in Aeronautics and Astronautics, Vol. 49), American Institute of Aeronautics and Astronautics, New York, 1979.
10. Tiwari, S. N., "Models for Infrared Atmospheric Radiation," *Advances in Geophysics*, Vol. 20, Academic Press, New York, 1978, pp. 1-85.
11. Tsai, S.S. and Chan, S. H., "Multi-Dimensional Radiative Transfer in Non-Gray Gases-General Formulation and the Bulk Radiative Exchange Approximation," *Journal of Heat Transfer*, Vol. 100, August 1978.
12. Chung, T.J. and Kim, J. Y., "Two-Dimensional Combined Mode Heat Transfer by Conduction, Convection and Radiation in Emitting, Absorbing and Scattering Media-Solution By Finite Elements," *Journal of Heat Transfer*, Vol. 106, pp. 448-452, May 1984.
13. Im, K.H. Ahluwalia, R. K., "Combined Convection and Radiation in Rectangular Duct," *International Journal of Heat and Mass Transfer*, Vol. 27, pp. 221-231, 1984.
14. Soufiani, A. and Taine, J., "Application of Statistical Narrow-Band Models to Coupled Radiation and Convection at High Temperature," *International Journal of Heat and Mass Transfer*, Vol. 30, No. 3, pp. 437-447, 1987.
15. Tiwari, S. N., "Radiative Interaction in Transient Energy Transfer in Gaseous Systems," NASA CR-176644, December 1985.
16. Mani, M., Tiwari, S. N. and Drummond, J. P., "Numerical Solution of Chemically Reacting and Radiating Flows," AIAA Paper 87-0324, January, 1987.
17. Tiwari, S. N. and Singh, D. J., "Interaction of Transient Radiation in Fully Developed Laminar Flow," AIAA Paper 86-1521, June 1987.
18. Mani, M., Tiwari, S. N. and Drummond, J. P., "Investigation of Two-Dimensional Chemically Reacting and Radiative Supersonic Channel Flows," AIAA Paper 88-0462, January 1988.
19. Mani, M. and Tiwari, S. N., "Investigation of Supersonic Chemically Reacting and Radiating Channel Flow," NASA CR-182726, January 1988; also Ph.D. Dissertation by M. Mani, Old Dominion University, May 1988.
20. Rogers, R. C. and Shnexnayder, C. J., Jr., "Chemical Kinetic Analysis of Hydrogen-Air Ignition and reaction Time," NASA TP-1856, 1981.

21. Shuen, S. J. and Yoon, S., "Numerical Study of Chemically Reacting Flows Using a Lower-Upper Symmetric Successive Overrelaxation Scheme," AIAA Journal, Vol. 27, No. 12, December 1989.
22. Carpenter, M. H., "A Generalized Chemistry Version of SPARK," NASA CR-4196, December 1988.
23. McCormack, R. W., "The Effect of Viscosity in Hypervelocity Impact Cratering," AIAA Paper 69-354, May, 1969.
24. Smoot, L. D., Hecker, W. C. and Williams, G. A., "Prediction of Propagating Methane-Air Flames," Combustion and Flame, Vol. 26, 1976.
25. Stalnaker, J. F., Robinson, M. A., Spradley, L. W., Kurzius, S. C. and Theores, D., "Development of the General Interpolants Methods for the CYBER 200 series of Computers," Report TR-0867354, Lockheed-Huntsville Research Engg. Center, Huntsville, Alabama, October 1983.

26. Bussing, T. R. and Murman, E. M., "A Finite Volume Method for the Calculation of Compressible Chemically Reacting Flows," AIAA Paper 85-0331, January 1985.
27. Smith, R. E. and Weigel, B. L., "Analytical and Approximation Boundary Fitted Coordinates System for Fluid Flow Simulation," AIAA Paper 80-0192, January 1980.
28. Wilkins, J. H., The Algebraic Eigenvalue Problem, Oxford University Press, Oxford, England, 1965, pp. 233-236.
29. Householder, A. S., The Theory of Matrices in Numerical Solution Analysis, Dover Publication, New York, 1964, pp. 122-140.
30. Jachimowski, C. J., "An Analytical Study of the Hydrogen-Air Reaction Mechanism with Application to Scramjet Combustion," NASA TP-2791, February 1988.

Table 1. Hydrogen-Air Combustion Mechanism (22)

REACTION	A(moles)	N(cm ³)	E(calories/gm-mole)
** following reactions constitute the 18-step model **			
(1) $O_2 + H_2 \leftrightarrow OH + OH$	1.70×10^{13}	0	48150
(2) $O_2 + H \leftrightarrow OH + O$	1.42×10^{14}	0	16400
(3) $H_2 + OH \leftrightarrow H_2O + H$	3.16×10^7	1.8	3030
(4) $H_2 + O \leftrightarrow OH + H$	2.07×10^{14}	0	13750
(5) $OH + OH \leftrightarrow H_2O + O$	5.50×10^{13}	0	7000
(6) $H + OH + M \leftrightarrow H_2O + M$	2.21×10^{22}	-2.0	0
(7) $H + H + M \leftrightarrow H_2 + M$	6.53×10^{17}	-1.0	0
(8) $H + O_2 + M \leftrightarrow HO_2 + M$	3.20×10^{18}	-1.0	0
(9) $OH + HO_2 \leftrightarrow O_2 + H_2O$	5.00×10^{13}	0	1000
(10) $H + HO_2 \leftrightarrow H_2 + O_2$	2.53×10^{13}	0	700
(11) $H + HO_2 \leftrightarrow OH + OH$	1.99×10^{14}	0	1800
(12) $O + HO_2 \leftrightarrow O_2 + OH$	5.00×10^{13}	0	1000
(13) $HO_2 + HO_2 \leftrightarrow O_2 + H_2O_2$	1.99×10^{12}	0	0
(14) $H_2 + HO_2 \leftrightarrow H + H_2O_2$	3.01×10^{11}	0	18700
(15) $OH + H_2O_2 \leftrightarrow H_2O + HO_2$	1.02×10^{13}	0	1900
(16) $H + H_2O_2 \leftrightarrow H_2O + OH$	5.00×10^{14}	0	10000
(17) $O + H_2O_2 \leftrightarrow OH + HO_2$	1.99×10^{13}	0	5900
(18) $H_2O_2 + M \leftrightarrow OH + OH + M$	1.21×10^{17}	0	45500
** remaining reactions complete the 35-step model **			
(19) $O_2 + M \leftrightarrow O + O + M$	2.75×10^{19}	-1.0	118700
(20) $N_2 + M \leftrightarrow N + N + M$	3.70×10^{21}	-1.6	225000
(21) $N + O_2 \leftrightarrow O + NO$	6.40×10^9	1.0	6300
(22) $N + NO \leftrightarrow O + N_2$	1.60×10^{13}	0	0
(23) $N + OH \leftrightarrow H + NO$	6.30×10^{11}	0.5	0
(24) $H + NO + M \leftrightarrow HNO + M$	5.40×10^{15}	0	-600
(25) $H + HNO \leftrightarrow H_2 + NO$	4.80×10^{12}	0	0
(26) $O + HNO \leftrightarrow OH + NO$	5.00×10^{11}	0.5	0
(27) $OH + HNO \leftrightarrow H_2O + NO$	3.60×10^{13}	0	0
(28) $HO_2 + HNO \leftrightarrow H_2O_2 + NO$	2.00×10^{12}	0	0
(29) $HO_2 + NO \leftrightarrow OH + NO_2$	3.43×10^{12}	0	-260
(30) $H + NO_2 \leftrightarrow OH + NO$	3.50×10^{14}	0	1500
(31) $O + NO_2 \leftrightarrow O_2 + NO$	1.00×10^{13}	0	600
(32) $NO_2 + M \leftrightarrow O + NO + M$	1.16×10^{16}	0	66000
(33) $M + OH + NO \leftrightarrow HNO_2 + M$	5.60×10^{15}	0	-1700
(34) $M + OH + NO_2 \leftrightarrow HNO_3 + M$	3.00×10^{15}	0	-3800
(35) $OH + HNO_2 \leftrightarrow H_2O + NO_2$	1.60×10^{12}	0	0
** following reactions constitute the global 2-step model [4, 16, 18, 19] **			
(1'') $H_2 + O_2 \leftrightarrow 2 OH$	11.4×10^{17}	-10.0	4865
(2'') $2 OH + H_2 \leftrightarrow 2 H_2O$	2.50×10^{14}	-13.0	42500

PAGE _____ INTENTIONALLY BLANK

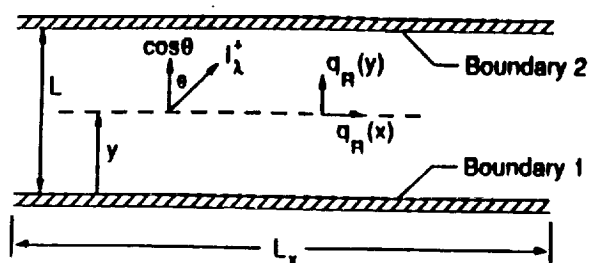


Fig. 1 Plane radiating layer between parallel boundaries

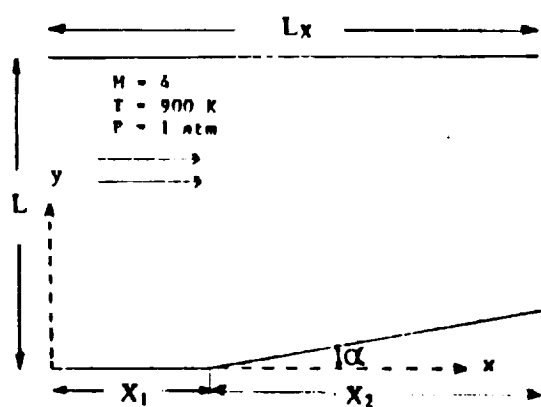


Fig. 2 Geometry for the premixed H_2 -Air reacting flow

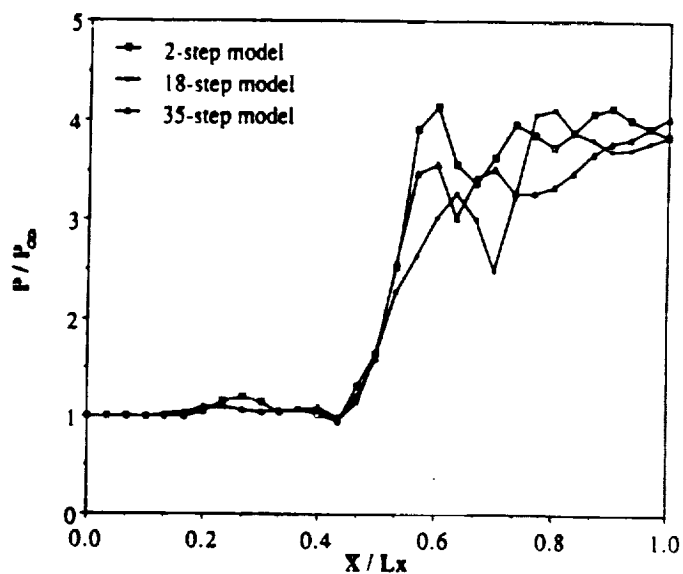


Fig. 4 Pressure profiles ($y = 0.13$ cm.)

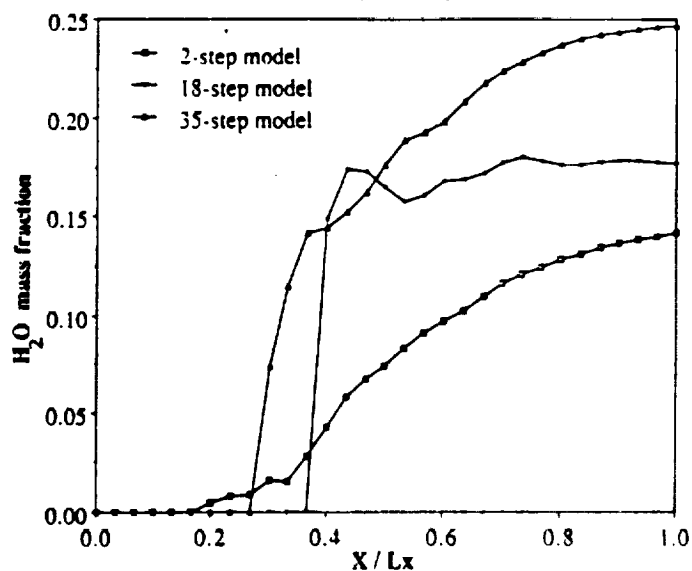


Fig. 5 H_2O mass fraction profiles

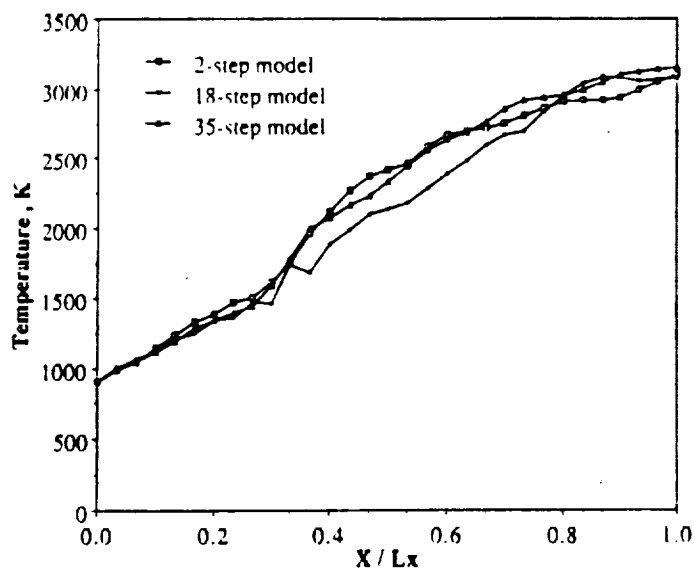


Fig. 3 Temperature profiles

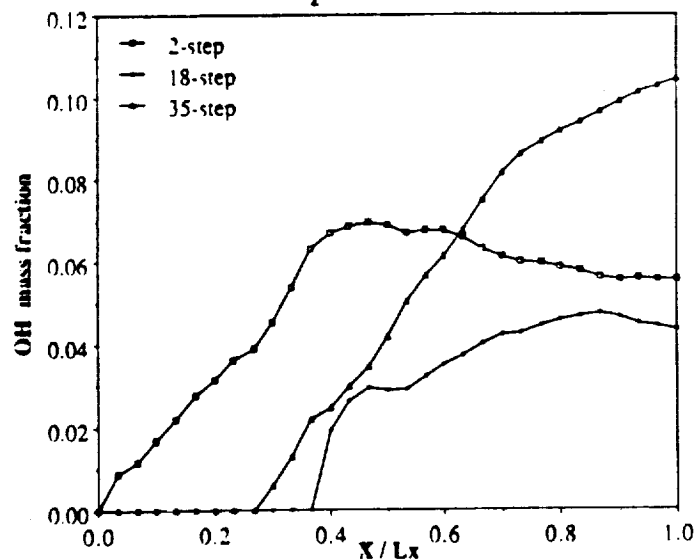


Fig. 6 OH mass fraction profiles

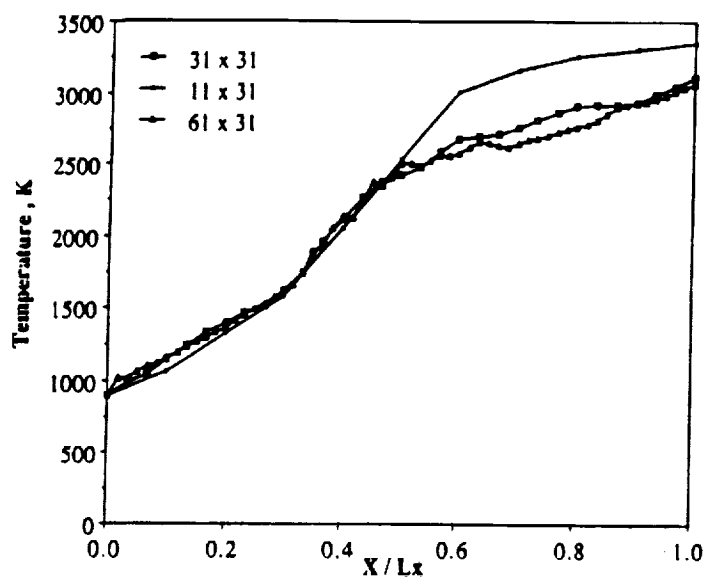


Fig. 7 Grid sensitivity results

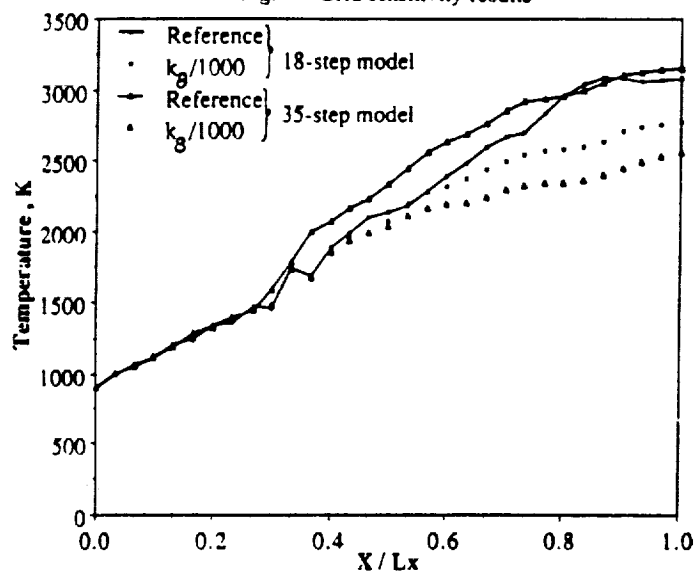


Fig. 8 Effect of reaction rates

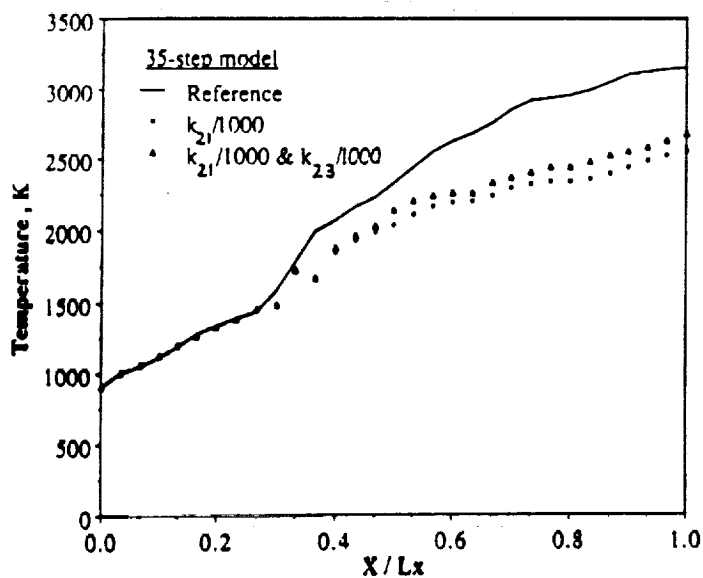


Fig. 9 Effect of NO and HO₂ reactions

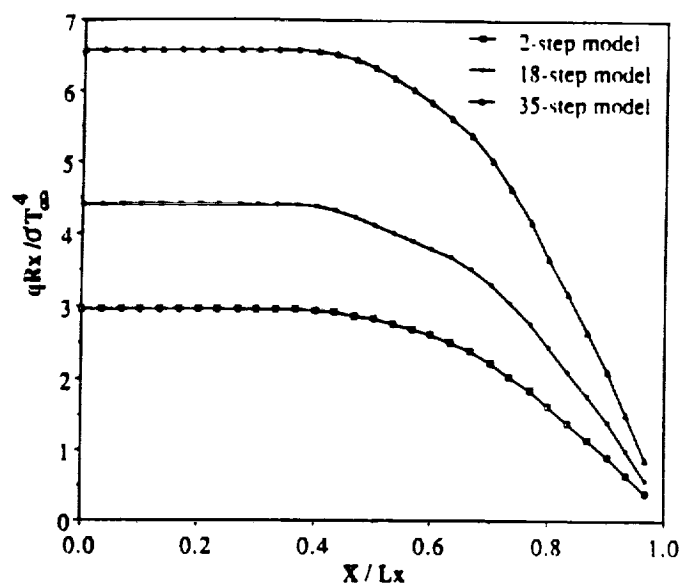


Fig. 10 Profiles of streamwise radiative flux

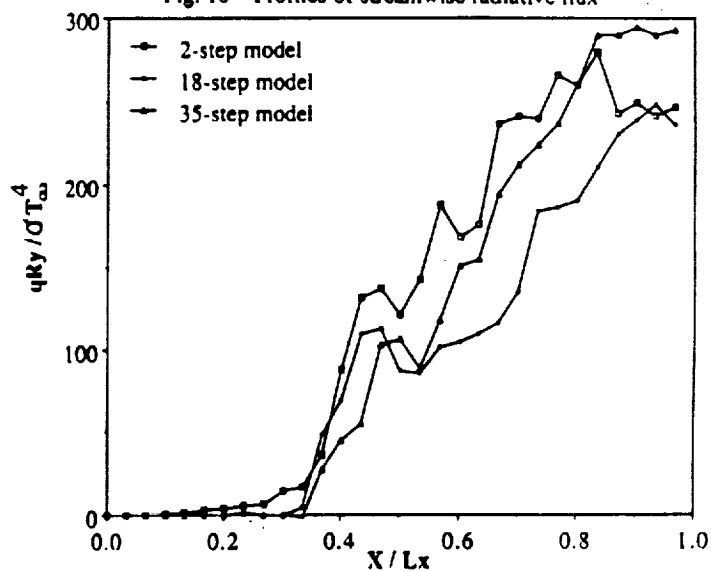


Fig. 11 Profiles of normal radiative flux

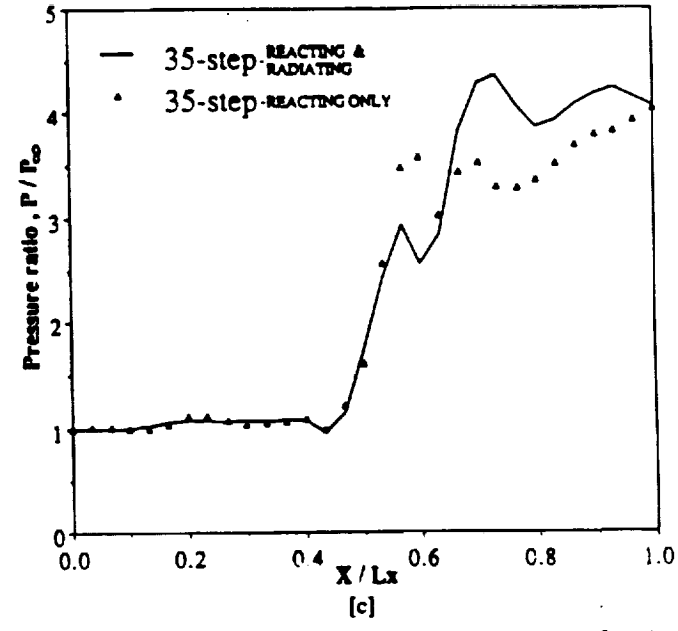
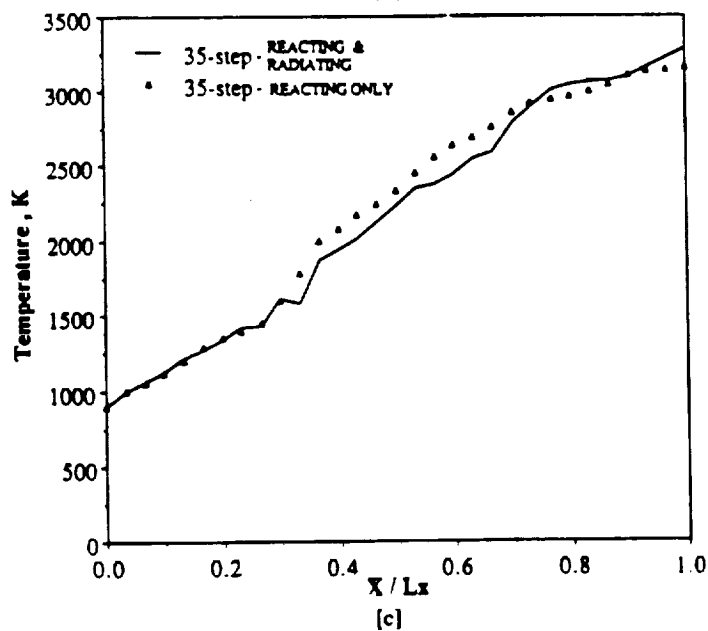
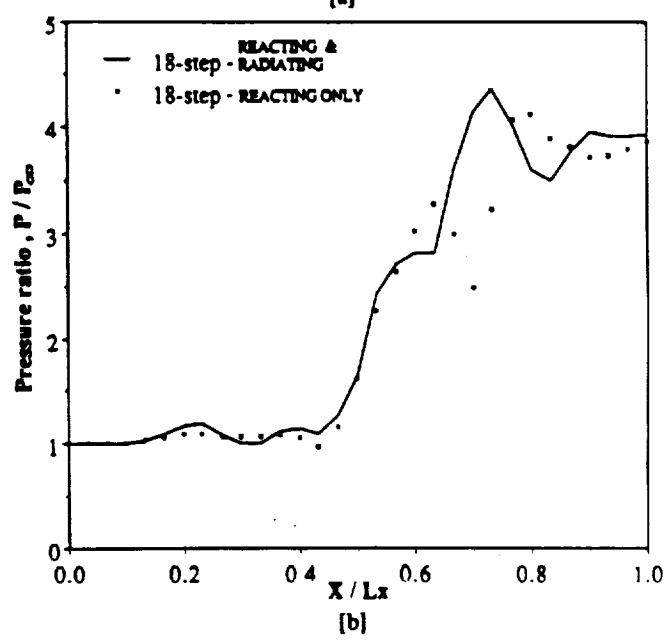
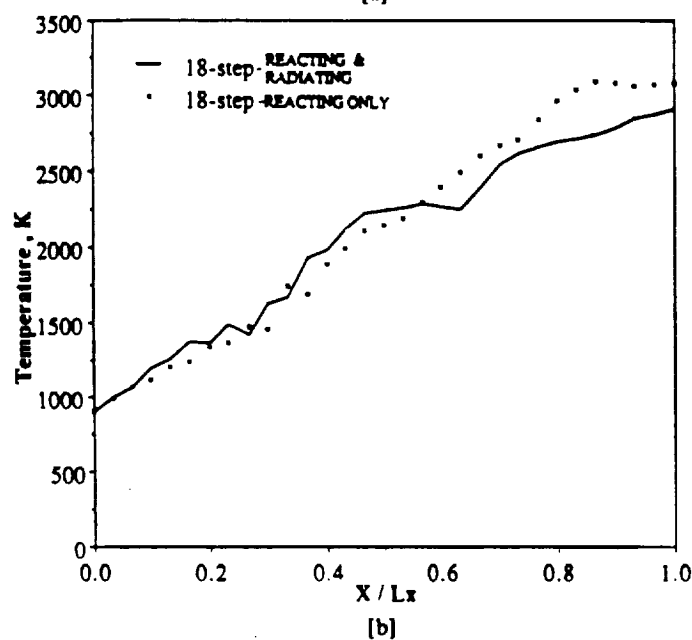
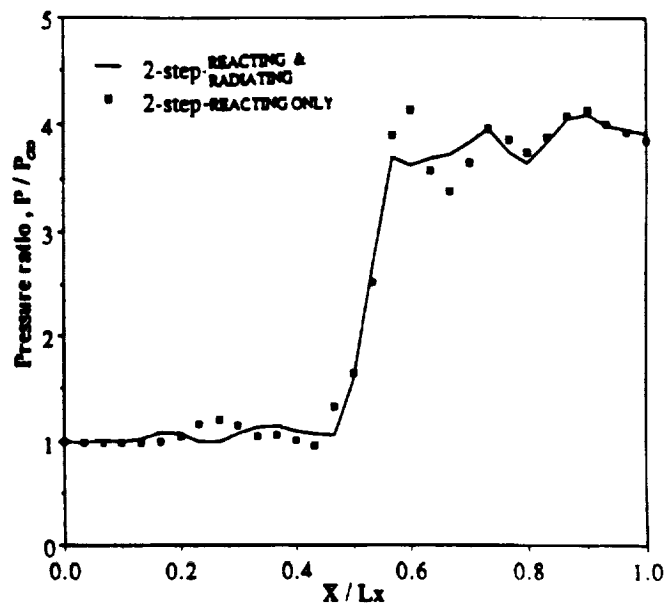
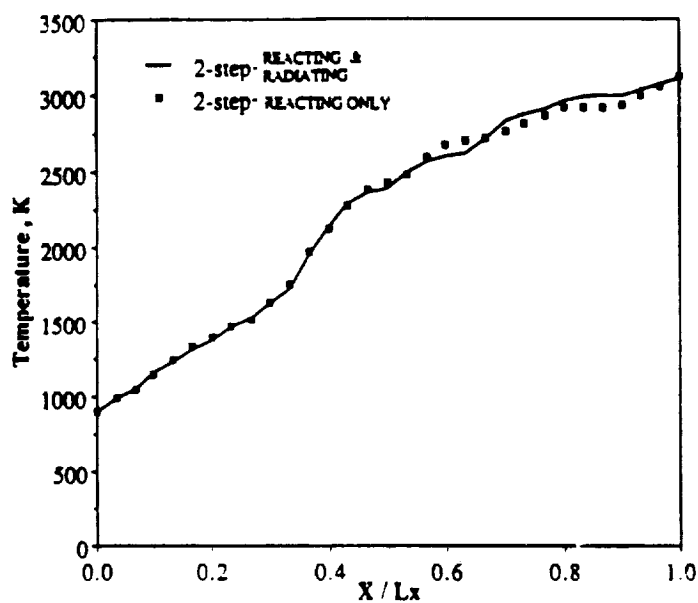


Fig. 12 Radiation effects on temperature profiles

Fig. 13 Radiation effects on pressure profiles ($y = 0.13$ cm)

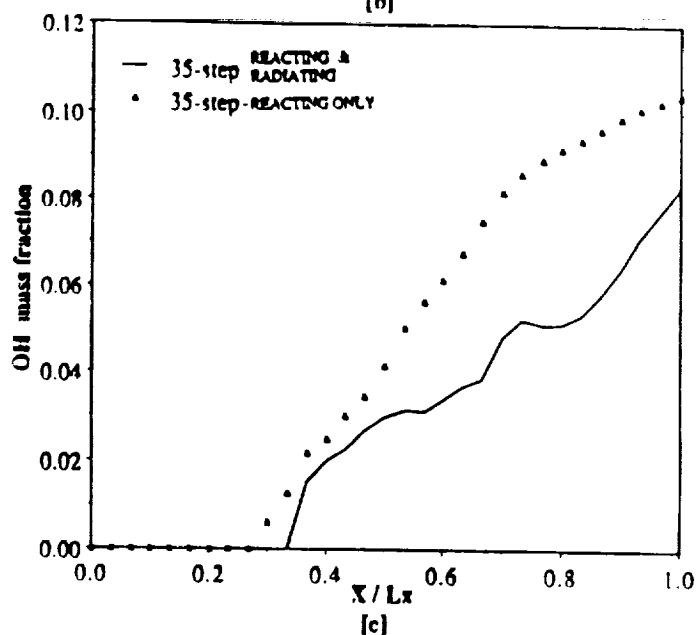
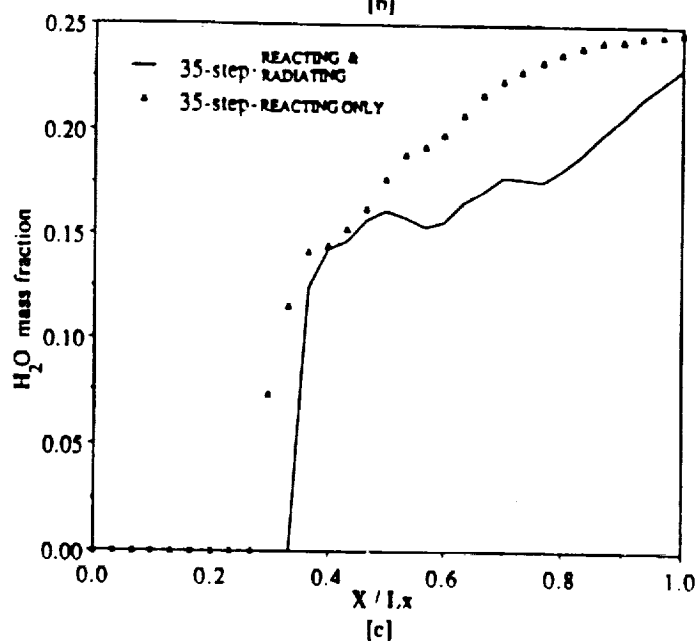
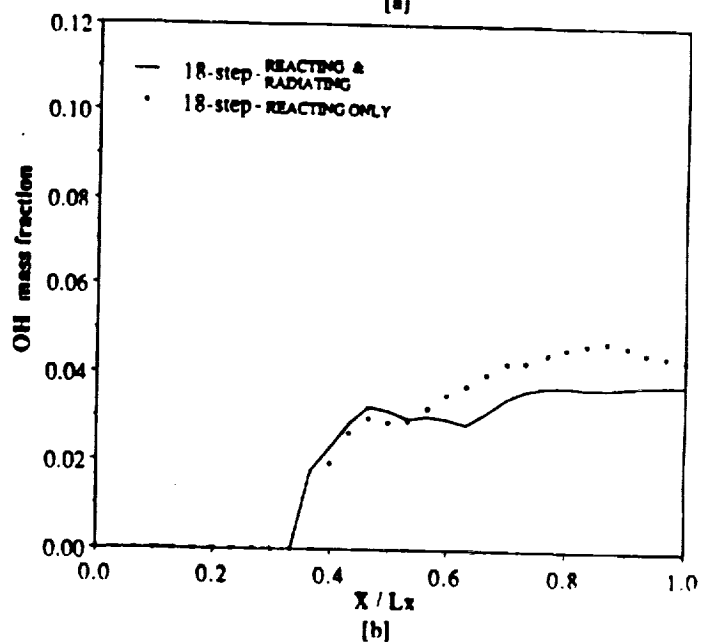
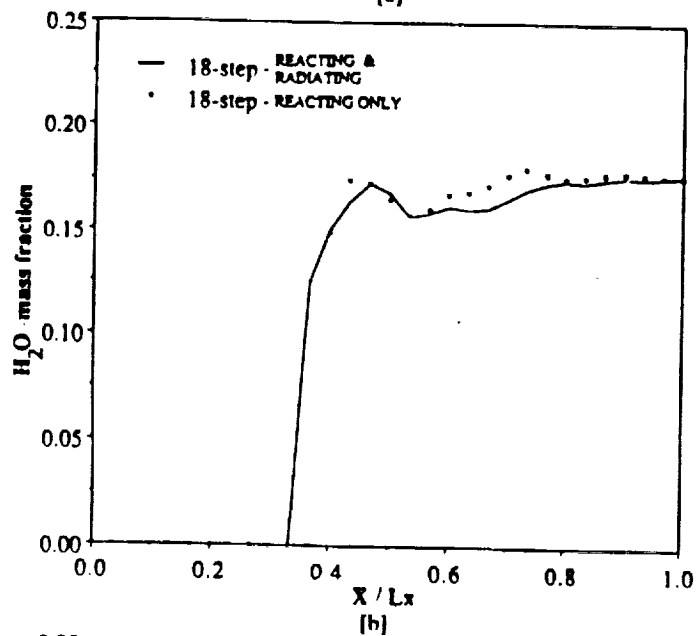
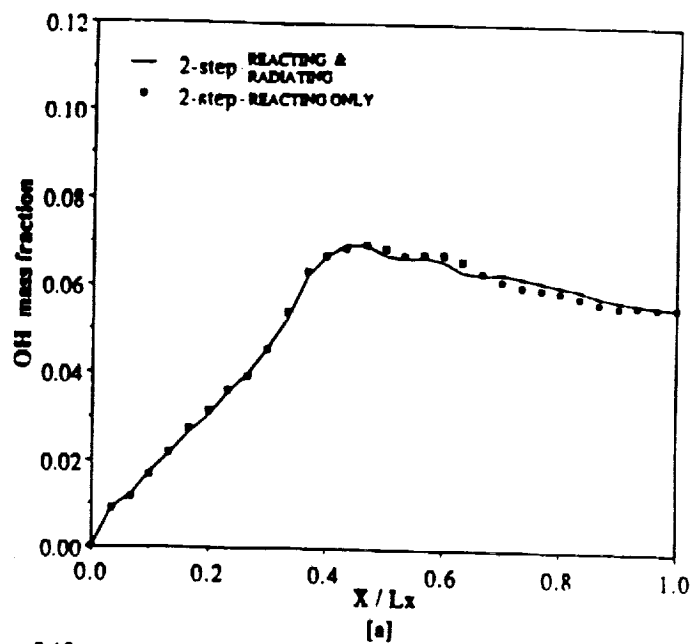
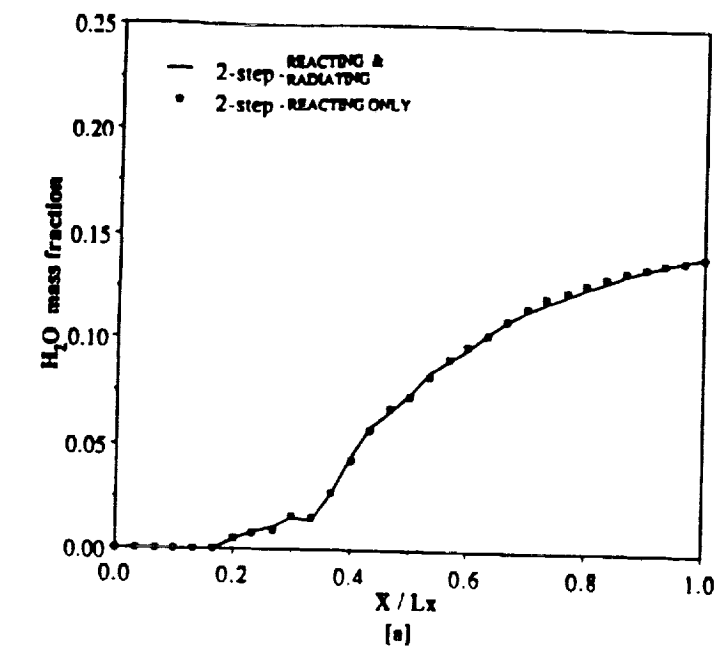


Fig. 14 Radiation effects on H_2O profiles

Fig. 15 Radiation effects on OH profiles



AIAA-91-0572

**INVESTIGATION OF RADIATIVE INTERACTIONS
IN CHEMICALLY REACTING SUPERSONIC
INTERNAL FLOWS**

S. N. Tiwari, R. Chandrasekhar, and A. M. Thomas
Old Dominion University
Norfolk, VA

J. P. Drummond
NASA Langley Research Center
Hampton, VA

29th Aerospace Sciences Meeting

January 7-10, 1991/Reno, Nevada

PAGE INTENTIONALLY BLANK

INVESTIGATION OF RADIATIVE INTERACTIONS IN CHEMICALLY REACTING SUPERSONIC INTERNAL FLOWS

S. N. Tiwari¹, R. Chandrasekhar², and A.M. Thomas³
Old Dominion University, Norfolk, Virginia 23529-0247

and

J.P. Drummond⁴
NASA Langley Research Center, Hampton, Virginia 23665-5225

Abstract

Analyses and numerical procedures are presented to investigate the radiative interactions of absorbing-emitting species in chemically reacting supersonic flow in various ducts. Specific attention is directed in investigating the radiative contributions of H_2O , OH , and NO under realistic physical and flow conditions. The radiative interactions in reacting flows are investigated by considering the supersonic flow of premixed hydrogen and air in a channel with a compression corner at the lower boundary. The results indicate that radiation can have significant influence on the flowfield and species production depending on the chemistry model employed.

Nomenclature

A	band absorptance, m^{-1}
A_0	band width parameter, m^{-1}
C_j	concentration of the j^{th} species, $kg\text{-mole}/m^3$
e_ω	Planck's function
E	total internal energy
f_j	mass fraction of j^{th} species
h	static enthalpy, J/kg
k	thermal conductivity, $J/m\text{-s-k}$

¹ Eminent Professor, Dept. of Mechanical Engineering and Mechanics. AIAA Associate Fellow

² Graduate Research Assistant, Dept. of Mechanical Engineering and Mechanics. AIAA Student Member

³ Graduate Research Assistant, Dept. of Mechanical Engineering and Mechanics.

⁴ Research Scientists, Theoretical Flow Physics Branch, Fluid Mechanics Division. AIAA Associate Fellow.

k_b	backward rate constant
k_f	forward rate constant
P	pressure, N/m^2
P_j	partial pressure of j^{th} species
Q_R	total radiative heat flux, J/m^2-s
$Q_{R\omega}$	spectral radiative heat flux, J/m^3-s
R	gas constant, $J/kg-K$
S	integrated band intensity, $(N/m^2)^{-1}m^{-2}$
T	temperature, K
u, v	velocity in x- and y-direction, m/s
\dot{w}_j	production rate of j^{th} species, kg/m^3-s
x, y	physical coordinates
κ_ω	spectral absorption coefficient, m^{-1}
κ_p	Planck mean absorption coefficient
λ	second coefficient of viscosity ^(also) wave length, m
μ	dynamic viscosity (laminar flow), $kg/m-s$
ξ, η	computational coordinates
ρ	density
σ	Stefan-Boltzmann constant, $erg/S-cm^2-K^4$
τ	shear stress
ϕ	equivalence ratio
ω	wave number, m^{-1}

Introduction

There is a renewed interest in investigating various aspects of radiative energy transfer in participating mediums. Radiative interactions become important in many engineering problems involving high temperature gases. Recent interest lies in the areas of design of high pressure combustion chambers and high enthalpy nozzles, entry and reentry phenomena, hypersonic propulsion, and defence oriented research.

Basic formulations on radiative energy transfer in participating mediums are available in standard references [1–5]. The review articles presented in [6–15] are useful in understanding the radiative properties of participating species and the nature of nongray radiation. The validity of radiative transfer analyses depends upon the accuracy with which absorption-emission and scattering characteristics of participating species are modeled. There are several models available to represent the absorption-emission characteristics of molecular species and these are reviewed in [12, 13]. These models have been used to investigate radiative interactions in several duct flows [16–29].

The purpose of this study is to investigate the effect of radiative heat transfer in chemically reacting supersonic flow in various ducts under different physical and flow conditions. This provides essential information for investigating the effect of radiative interactions in the combustor of a supersonic combustion ramjet (scramjet) engine. This hydrogen-fueled engine is proposed for propelling transatmospheric hypersonic vehicles. Several basic codes have been developed to compute the flowfield in a scramjet engine [21–24]. The combustion of hydrogen and air results in absorbing-emitting gases such as H_2O , OH , and NO . Specific attention, therefore, is directed in investigating the radiative contributions of these gases under realistic conditions. In essence, the present effort is a continuing of the earlier work conducted in this area of research [25–27]. Extensive literature survey is provided in the cited references. A comparison of different chemistry models used in investigating radiative interactions is presented in [28].

Basic Governing Equations

The physical problem considered to investigate the effect of radiative interactions in supersonic flow are two-dimensional laminar flow between two parallel plates (Fig. 1a) and within a circular tube (Fig. 1b). Another geometry is considered to study the effect of shocks and chemical reactions on the radiative heat transfer and this consists of a channel with a compression-expansion ramp (Fig. 1c). The governing equations and boundary conditions are provided here for all physical problems considered in this study.

The physical problem considered for basic understanding of radiative interaction in supersonic flows is two-dimensional variable property laminar flow between two parallel plates. For this model, two-dimensional Navier-Stokes equations in fully conservative form are used to describe the flow field. These equations, in physical domain, can be written as [27,29]

$$\frac{\partial U}{\partial t} + \frac{\partial F}{\partial x} + \frac{\partial G}{\partial y} + H = 0 \quad (1)$$

where vectors U , F , G and H are written as

$$U = \begin{bmatrix} \rho \\ \rho u \\ \rho v \\ \rho E \\ \rho f_j \end{bmatrix}$$

$$F = \begin{bmatrix} \rho u \\ \rho u^2 + p + \tau_{xx} \\ \rho uv + \tau_{xy} \\ (\rho E + p)u + \tau_{xx}u + \tau_{xy}v + q_{cx} + q_{Rx} \\ \rho u f_j - \rho l \frac{\partial f_j}{\partial x} \end{bmatrix}$$

$$G = \begin{bmatrix} \rho v \\ \rho uv + \tau_{yx} \\ \rho v^2 + p + \tau_{yy} \\ (\rho E + p)v + \tau_{yy}v + \tau_{xy}u + q_{cy} + q_{Ry} \\ \rho v f_j - \rho D \frac{\partial f_j}{\partial y} \end{bmatrix}$$

$$H = \begin{bmatrix} 0 \\ 0 \\ 0 \\ 0 \\ -\dot{w}_j \end{bmatrix}$$

The viscous stress terms appearing in the definitions of F and G are given in [27]. The relations for conduction heat transfer in x and y directions are given by

$$q_{Cx} = -k \frac{\partial T}{\partial x}, \quad q_{Cy} = -k \frac{\partial T}{\partial y} \quad (2)$$

The terms q_{Rx} and q_{Ry} represent radiative fluxes in x and y directions, respectively; expressions for these are provided in the next section. The total energy flux in a given direction is given by the corresponding last term in the definitions of F or G . Consequently, this formulation involves all kinds of energy interaction including frictional (aerodynamic) heating. The coefficient of viscosity is evaluated by using the Sutherland's formula and the coefficient of thermal conductivity is calculated by using a constant value of the Prandtl number. The total internal energy E appearing in U , F , and G is given by

$$E = P/\rho + \frac{u^2 + v^2}{2} + \sum_{i=1}^m h_i f_i \quad (3)$$

Equation (1) can be used to obtain solutions for all kinds of compressible flows. However, boundary conditions and numerical procedures for different flows are quite different. For supersonic flows the inflow conditions are specified and outflow conditions are obtained by extrapolation. The boundary conditions used along the surfaces are $u=0$, $v=0$, $\partial P/\partial y = 0$, and $T=T_w$.

The governing equations and boundary conditions for the supersonic flow through a channel with a compression-expansion ramp is essentially the same as for the parallel plate geometry. However, a strong shock is produced at the compression corner and the flow becomes highly reacting from the beginning of the x_2 -coordinate. (Fig. 1c).

The basic governing equations for chemically reacting compressible flow through a circular tube can be written as [29,30]

$$\frac{\partial U}{\partial t} + \frac{\partial F}{\partial x} + \frac{1}{y} \frac{\partial}{\partial y} (yG) = \Pi/y \quad (4)$$

where x and y represent the streamwise and radial coordinates, respectively. In Fig. 1b, the radial coordinate is denoted by r . Thus, both r and y notations are used to represent the radial coordinate for the circular geometry. The definitions of vectors U , F , and G in Eq. (4) are same as given in Eq. (1) and vector H is expressed as

$$H = [0 \quad 0 \quad p + \tau_{\theta\theta} \quad 0 \quad y \quad \dot{w}_j] \quad (5)$$

For the circular tube geometry, the viscous terms appearing in Eq. (1) are given by

$$\tau_{xx} = -\lambda \left(\frac{\partial u}{\partial x} + \frac{\partial u}{\partial y} + \frac{u}{y} \right) - 2\mu \frac{\partial u}{\partial x} \quad (6a)$$

$$\tau_{yy} = -\lambda \left(\frac{\partial u}{\partial x} + \frac{\partial u}{\partial y} + \frac{v}{y} \right) - 2\mu \frac{\partial v}{\partial y} \quad (6b)$$

$$\tau_{xy} = -\mu \left(\frac{\partial u}{\partial y} + \frac{\partial v}{\partial x} \right) \quad (6c)$$

$$\tau_{\theta\theta} = -\lambda \left(\frac{\partial u}{\partial x} + \frac{\partial u}{\partial y} + \frac{v}{y} \right) - 2\mu \frac{v}{y} \quad (6d)$$

The boundary conditions for the circular tube geometry are similar to the parallel plate geometry.

Radiative Transfer Models

Evaluation of the energy equation presented in Eqs. (1) and (4) requires an appropriate expression for the net radiative flux in each direction. A suitable radiative transport model is needed to represent the true nature of participating species and transfer processes. In this section, a brief discussion of various absorption models is given and essential equations for the radiative flux are presented.

Absorption Models

Several models are available in the literature to represent the absorption-emission characteristics of molecular species. The total band absorptance of a vibration-rotation band is given by

$$A = \int_{-\infty}^{\infty} [1 - \exp(-\kappa_{\omega} X)] d(\omega - \omega_o) \quad (7)$$

where κ_{ω} is the volumetric absorption coefficient, ω is the wave number, ω_o is the wave number at the band center, $X = Py$ is the pressure path length, and the limits of integration are over the entire band pass. Various models are used to obtain the relation for A in Eq. (7).

The gray gas model is probably the simplest model to employ in radiative transfer analyses. In this model, the absorption coefficients is assumed to be independent of frequency, i. e., κ_{ω} is not a function of ω . A convenient model to represent the average absorption coefficient of a gray gas is the Planck mean absorption coefficient κ_p which is defined as [1]

$$\kappa_p = \int_0^{\infty} \kappa_{\omega} e_{b\omega}(T) d\omega / e_b(T) \quad (8a)$$

For a multiband gaseous system, this is expressed as

$$\kappa_p = [P_j / (\sigma T^4)] \sum_i^n e_{\omega_i}(T) S_i(T) \quad (8b)$$

where P_j is the partial pressure of j th species in a gaseous mixture, $e_{\omega_i}(T)$ is the Planck function evaluated at the i th band center, and $S_i(T)$ is the integrated band intensity of the i th band.

As defined in Eq. (8), κ_p is a property of the medium. When κ_p is evaluated at the temperature of the gas, it is actually a mean emission coefficient and it becomes equal to the actual mean absorption coefficient only for the conditions of equilibrium radiation field. For a nonuniform temperature field, the mean absorption coefficient used for the optically thin radiation is the modified Planck mean absorption coefficient which for black bounding surfaces is defined as [1,9]

$$\kappa_m(T, T_w) = \left[\int_0^{\infty} \kappa_{\omega}(T) e_{b\omega}(T_w) d\omega \right] / e_b(T_w) \quad (9a)$$

Note that κ_m is a function of both the gas temperature and the wall temperature. An approximate relation between κ_p and κ_m is available for infrared radiation as [1]

$$\kappa_m(T, T_w) = \kappa_p(T_w)(T_w/T) \quad (9b)$$

This expression is usually employed in gray gas radiative energy transfer analyses.

Several other models for the mean absorption coefficient are available in the literature [1,31]. Since these models account for detailed spectral information of molecular bands, this approach of radiative formulation is referred to as the "pseudo-gray formulation." The gray gas formulation for radiative transport is very useful in parametric studies.

There are several nongray models available in the literature to represent the absorption-emission characteristics of vibration-rotation bands. These are classified generally in four classes, (1) line-by-line (LBL) models, (2) narrow band models, (3) wide band models, and (4) band model correlations. A complete discussion on usefulness and application of these models is provided in [12, 13]. For many engineering applications, wide band model correlations provide quite accurate results. The most commonly used wide band model correlations are due to Edwards [5, 11] and Tien and Lowder [9]. The Tien and Lowder correlation for the total band absorptance is a continuous correlation and is given by the relation

$$\bar{A}(u, \beta) = A(u, \beta)/A_o = \ln\{uf(t)[(u+2)/(u+2f(t))] + 1\} \quad (10)$$

where

$$f(t) = 2.94[1 - \exp(-2.60t)], t = \beta/2$$

and $u = SX/A_o$ is the nondimensional path length, $\beta = 2\pi\gamma/d$ is the line structure parameter, γ is the line half width, S is the integrated band intensity, and A_o is the band width parameter. Equation (10) provides accurate results for pressures higher than 0.5 atmosphere [12, 13].

Spectral properties and correlation quantities for various radiation participating species are available in [5, 9, 11]. These are useful in gray as well as nongray radiative formulations.

Radiative Flux Equations

For many engineering and astrophysical applications, the radiative transfer equations are formulated assuming one-dimensional planar systems. For diffuse nonreflecting boundaries and in absence of scattering, the expression for the spectral radiative flux in the normal direction is given by [1, 19]

$$q_{R\omega}(y) = e_{1\omega} - e_{2\omega} + \frac{3}{2} \int_0^y F_{1\omega}(z) \kappa_\omega \exp\left[-\frac{3}{2} \kappa_\omega(z-y)\right] dz - \frac{3}{2} \int_y^L F_{2\omega}(z) \kappa_\omega \exp\left[-\frac{3}{2} \kappa_\omega(z-y)\right] dz \quad (11)$$

where

$$F_\omega(z) = e_\omega(z) - e_{1\omega}, F_{2\omega}(z) = e_2(z) - e_{2\omega}$$

It should be pointed out that the exponential kernel approximation has been used in obtaining Eq. (11). The total radiative flux in a given direction is expressed as

$$q_R = \int_0^\infty q_{R\omega} d\omega \quad (12)$$

A combination of Eqs. (11) and (12) provides a proper form of total radiative flux equation for obtaining nongray solutions of molecular species. Any convenient absorption model can be used to obtain nongray results.

For a gray medium, Eq. (11) reduces to a simpler form and upon differentiating the resulting equation twice, the integrals are eliminated and there is obtained a nonhomogeneous ordinary differential equation as [1, 16, 27]

$$\frac{1}{\kappa^2} \frac{d^2 q_R(y)}{dy^2} - \frac{9}{4} q_R(y) = \frac{3}{\kappa} \frac{de(y)}{dy} \quad (13)$$

where $\kappa = \kappa_p$. Equation (13) is a second order differential equation and, therefore, requires two boundary conditions. For nonblack diffuse surfaces, these are given as

$$\left(\frac{1}{\epsilon_1} - \frac{1}{2}\right)[q_R(y)]_{y=0} - \frac{1}{3\kappa} \left[\frac{dq_R}{dy}\right]_{y=0} = 0 \quad (14a)$$

$$\left(\frac{1}{\epsilon_2} - \frac{1}{2}\right)[q_R(y)]_{y=L} - \frac{1}{3\kappa} \left[\frac{dq_R}{dy}\right]_{y=L} = 0 \quad (14b)$$

Equation (13) along with boundary conditions can be used to obtain the energy equation for gray gas radiative interaction. For black walls and $T_1 = T_2$, the boundary conditions for Eq. (13) become

$$q_R(1/2) = 0, \frac{3}{2}q_R(0) = \frac{1}{\tau_o} (dq_R/d\xi)_{\xi=0}, \quad \tau_o = \kappa L, \xi = y/L \quad (15)$$

For a black circular tube, the spectral radiative heat flux in the radial direction is given by the expression [17]

$$\begin{aligned} q_{R\omega}(r) = & \frac{4}{\pi} \int_0^{\pi/2} \left\{ \int_{r \sin \gamma}^r F_{\omega}(r') \kappa_{\omega} a \exp \left[-\frac{b \kappa_{\omega}}{\cos \gamma} (r - r') \right] dr' \right. \\ & - \int_r^{r_o} F_{\omega}(r') \kappa_{\omega} a \exp \left[-\frac{b \kappa_{\omega}}{\cos \gamma} (r' - r) \right] dr \\ & \left. + \int_{r \sin \gamma}^{r_o} F_{\omega}(r') \kappa_{\omega} a \exp \left[-\frac{b \kappa_{\omega}}{\cos \gamma} (r + r' - 2r \sin \gamma) \right] dr' \right\} d\gamma \end{aligned} \quad (16)$$

where $F_{\omega}(r') = e_{\omega}(r') - e_{\omega}(T_w)$ and constants a and b have values of unity and $5/4$, respectively. A combination of Eqs. (12) and (16) provides a convenient form of the total radiative flux for nongray analyses.

For a gray medium, the expression for the total radiative flux can be obtained from differential approximation as [1, 17]

$$\frac{d}{dr} \left[\frac{1}{r} \frac{d}{dr} (r q_R) \right] - \frac{9}{4} \kappa^2 q_R = 3\sigma \kappa \frac{dT^4}{dr} \quad (17)$$

For a black tube, the boundary conditions for Eq. (16) are found to be

$$\frac{3}{2} q_R(1) = -\frac{1}{\bar{\tau}_o} \left[\frac{1}{\xi} \frac{d}{d\xi} (\xi q_R) \right]_{\xi=1}, \quad q_R(0) = 0, \quad \bar{\tau}_o = \kappa r_o, \xi = r/r_o \quad (18)$$

Equation (17) is used along with Eq. (18) for general one-dimensional gray gas formulation and analyses.

With certain modifications, the radiative flux equations presented in this section can also be used to investigate the radiative interactions in the flow direction. The procedure for doing this is provided in [27].

Chemistry and Thermodynamic Models

Chemical reaction rate expressions are usually determined by summing the contributions from each relevant reaction route (or path) to obtain the total rate of change of each species. Each path is governed by a law of mass action expression in which the rate constants can be determined from a temperature dependent Arrhenius expression. The reaction mechanism is expressed in a general form as

$$\sum_{j=1}^{ns} \gamma'_{ij} C_j \xrightleftharpoons[k_{bi}]{k_{fi}} \sum_{j=1}^{ns} \gamma''_{ij} C_j, \quad i = 1, \text{ nr} \quad (19)$$

where ns= number of species and nr= number of reactions. The chemistry source terms in Eqs. (1) and (4) are obtained, on a mass basis, by multiplying the molar changes and corresponding molecular weight as

$$\dot{w}_j = M_j C_j = M_j \sum_{i=1}^{nr} (\gamma''_{ij} - \gamma'_{ij}) \left[k_{fi} \prod_{m=1}^{ns} C_m^{\gamma'_{im}} - k_{bi} \prod_{m=1}^{ns} C_m^{\gamma''_{im}} \right] \quad (20)$$

The reaction constants k_{fi} and k_{bi} appearing in Eqs. (19) and (20) are determined from an Arrhenius rate equation given by

$$k_{fi} = A_i T^{N_i} \exp\left(-\frac{E_i}{RT}\right) \quad (21)$$

where

$$k_{bi} = k_{fi}/k_{eqi}, \quad k_{eqi} = \left(\frac{1}{RT}\right)^{\Delta N_i} \exp\left(\frac{-\Delta G_{Ri}}{RT}\right)$$

The coefficients A, N, and E appearing in Eq. (21) are given in Table 1 and the Gibbs energy term ΔG_{Ri} is calculated as

$$\Delta G_{Ri} = \sum_{j=1}^{ns} \gamma''_{ij} g_j - \sum_{j=1}^{ns} \gamma'_{ij} g_j, \quad j = 1, \text{ nr} \quad (22)$$

where

$$\begin{aligned} \frac{g_j}{R} = & A_j(T - \ln T) + \frac{B_j}{2} T^2 + \frac{C_j}{6} T^3 \\ & + \frac{D_j}{12} T^4 + \frac{E_j}{20} T^5 + F_j + G_j T \end{aligned}$$

The gas constant for the mixture is evaluated by a mass-weighted summation over all species as

$$\bar{R} = \sum_{j=1} f_j R_j \quad (23)$$

The equation of state for the mixture is written as

$$P = \rho \bar{R} T \quad (24)$$

Method of Solution

The governing equations are transformed from the physical domain (x, y) to a computational domain (ξ, η) using an algebraic grid generation technique similar to the one used by Smith and Weigel [32]. The grid spacing is kept uniform in the flow direction and compressed near the boundaries in the normal direction. The governing equations, Eqs. (1) and (4), are expressed respectively in the computational domain as

$$\frac{\partial \hat{U}}{\partial t} + \frac{\partial \hat{F}}{\partial \xi} + \frac{\partial \hat{G}}{\partial \eta} + \hat{H} = 0 \quad (25)$$

$$\frac{\partial \hat{U}}{\partial t} + \frac{\partial \hat{F}}{\partial \xi} + \frac{1}{\eta} \frac{\partial}{\partial \eta} (\eta \hat{G}) = \hat{H} / \eta \quad (26)$$

where

$$\hat{U} = UJ, \quad \hat{F} = Fy_\eta - Gx_\eta, \quad \hat{G} = Gx_\xi - Fy_\xi,$$

$$\hat{H} = HJ, \quad J = x_\xi y_\eta - y_\xi x_\eta$$

The temporal discretization procedure for Eqs. (25) and (26) is given in [25-27]. Once this has been performed, the resulting system is spatially differenced using the explicit unsplit MacCormack predictor-corrector scheme [33]. This results in a spatially and temporally discrete, simultaneous system of equations at each grid point [34,35]. Each simultaneous system is solved using the Householder technique [36,37], and is marched in time until convergence is achieved.

The details of gray as well as nongray radiative flux formulations and solution procedure are available in [19,27]. For the gray gas model, the governing equations are discretized using a central difference scheme. The discretization of Eqs. (13) and (17) results, respectively, in

$$\left(\frac{2}{A_j}\right)q_{j-1} - \left[\frac{2}{B_j}\left(\frac{1}{C_j} + \frac{1}{\Delta y_j}\right) + \frac{9}{4}\kappa_j^2\right]q_j + \left(\frac{2}{A_j\beta_j}\right)q_{j+1} = \text{RHS} \quad (28)$$

$$\begin{aligned} &\left(\frac{2}{A_j} + \frac{1}{2y_j C_j}\right)q_{j+1} - \left[\frac{2}{B_j}\left(\frac{1}{C_j} + \frac{1}{\Delta y_j}\right) + \frac{9}{4}\kappa_j^2\right] \\ &+ \frac{1}{y^2} + \frac{1}{2y_j C_j} - \frac{1}{2y_j \Delta y_j}\bigg]q_j + \left(\frac{2}{A_j\beta_j} - \frac{2}{2y_j \Delta y_j}\right)q_{j-1} = \text{RHS} \end{aligned} \quad (29)$$

where

$$A_j = \Delta y_j^2(1 + \beta_j), \quad B_j = \Delta y_j(1 + \beta_j), \quad C_j = \beta_j \Delta y_j, \\ \text{RHS} = 1.5\kappa_j \left[\frac{e_{j+1} - e_j}{\beta_j \Delta y_j} + \frac{e_j - e_{j-1}}{\Delta y_j} \right], \quad \Delta y_j = y_j - y_{j-1}, \quad \beta_j = \frac{y_{j+1} - y_j}{y_j - y_{j-1}}$$

Equations (27) and (28) along with boundary conditions given by Eqs. (15) and (18) form tridiagonal systems of equations which can be solved efficiently by the Thomas algorithm.

In the nongray gas formulation, the divergence of the radiative flux is evaluated using a central differencing scheme and is treated as radiative source term in the energy equation. Since the radiative flux terms involves integral formulation, unlike other flux terms which are only in a differential form, it is uncoupled and treated separately.

Physical Conditions and Data Source

The physical conditions for which specific flowfield analyses and computations are needed are discussed in [21–28]. In this work selected parametric studies have been conducted for certain flow and physical conditions. Radiation participating species considered are H_2O , OH , and NO . Radiative properties of these species are available in [5, 9, 11–13]. Different amounts of these gases, in combination with air, are considered for parametric studies. Essential data for the chemistry model employed are obtained from Refs. 38–40 and these are provided in Table 1.

For basic studies, the physical dimensions considered for the channel are $L=3$ cm and $L_x=10$ cm, and for the circular tube they are $L=D=3$ cm and $L_x=10$ cm. Certain results, however, were obtained also for other dimensions.

Results and Discussion

Based on the theory and computational procedure described in the previous sections, an existing computer code was modified to solve the two-dimensional Navier-Stokes equations for radiating supersonic laminar flows between two parallel black plates. A similar code was developed for radiating supersonic flows in a circular tube. In most cases, the radiative interaction was considered only in the normal direction. Extensive results have been obtained for pure H_2O , OH , and NO as homogeneous participating species, and for different mixtures of these species with air. Selected results are presented and discussed in this section.

For the parallel plate geometry (3 cm x 10 cm), a comparison of the divergence of radiative flux for general (nongray), gray, and their optically thin limit models is presented in Fig. 2 for two different y -locations ($y=0.2$ and 1.5 cm). The inflow conditions for this case are $P_\infty = 1$ atm, $T_\infty = 1,700$ K, $M_\infty = 4.3$, $f_{H_2O} = 0.5$, $f_{O_2} = 0.1$, and $f_{N_2} = 0.4$. The gray formulation is based on the modified Planck mean absorption coefficient which accounts for the detailed information on different molecular bands. The range of optical thickness calculated in [27] was found to be between 0.0003 and 0.4. Thus, for the physical model and inflow conditions considered, the radiative interaction is essentially in the optically thin range. No significant difference in results is observed for the two y -locations. This is a typical characteristic of the optically thin radiation [1,10]. The solution of the gray formulation requires about ten times less computational resources in comparison to the solution of the nongray formulation [27].

As mentioned earlier, the Planck mean absorption coefficient κ_p (or κ_m) is considered to be an optically thin radiation absorption coefficient, although it has been used in other optical ranges as well [1,9]. The appropriate absorption coefficient for the optically thick radiation is the Rosseland mean absorption coefficient κ_R . It has been pointed out in [1] that if the medium is

gray then $\kappa_R = \kappa_P = \kappa$; otherwise $\kappa_P > \kappa_R$. Thus, use of κ_P (or κ_m) in pseudo-gray gas formulation will provide maximum influence of radiative interaction. The κ_P values for H_2O , OH , and NO have been calculated from Eq. (8b) by employing radiative properties available in [5, 9, 11] and these are illustrated in Fig. (3). Figure 3a shows the results of 100% homogeneous species whereas results in Fig. 3b are for different mixtures. The results provide indication of radiative ability of different species at a given temperature. Values of κ_P for other species are available in [1, 9].

The results of supersonic entrance region flow between parallel plates are presented in Figs. 4-10 for different physical and inflow conditions. As mentioned earlier, the basic physical dimensions considered for the channel are $L=3$ cm and $L_x=10$ cm. In most cases, the inflow conditions considered are $P_\infty=1$ atm, $T_\infty=1,700$ K, $U_\infty=2574$ m/s ($M_\infty=3.0$) with varying amounts of radiation participating species in combination with air. Certain variations in physical and inflow conditions are also considered for parametric studies. The chemical reactions are not considered in obtaining the results of Figs. 4-10, and radiative flux results are presented only for the normal direction.

Results for radiative flux are illustrated in Figs. 4 and 5 as a function of the nondimensional y-coordinate. For $P=1$ atm, the results presented in Fig. 4 for different water vapor concentrations indicate that the radiative interaction increases slowly with an increase in the amount of the gas. The results for 50% H_2O are presented in Fig. 5 for two different pressures ($P_\infty=1$ and 3 atm) and x-locations ($x=5$ and 10 cm). It is noted that the increase in pressure has dramatic effects on the radiative interaction.

For a mixture of 50% H_2O in air, the conduction and radiation heat transfer results are compared in Fig. 6 for $P_\infty=3$ atm and for two different x-locations ($x=5$ and 10 cm). The results demonstrate that the conduction heat transfer is restricted to the region near the boundaries and does not change significantly from one x-location to another. The radiative interaction, however, is seen to be important everywhere in the channel, and this can have a significant influence on the entire flowfield.

Comparative results for 100% homogeneous species of H_2O , NO and OH are illustrated in Fig. 7 at the exit plane ($x=10$ cm). As would be expected, the radiative contribution of H_2O (with five bands) is significantly higher than NO and OH . Only the fundamental bands of NO and OH are considered in this study, and it is noted that NO is a better radiating gas in comparison to OH .

For a mixture of 25% H_2O in air, radiative flux for two different plate spacings ($L=3$ and 6 cm) are illustrated in Fig. 8 for two x -locations ($x=5$ and 10 cm). The rate of radiative transfer is a strong function of the amount of the participating species and the pressure path length, PL . consequently, the results for the larger plate spacing indicate significantly higher radiative interactions.

The effect of increased Mach number on the radiative transfer is illustrated in Fig. 9 for pure H_2O and for a mixture of 50% H_2O in air. The results shown are for the exit plane ($x=10$ cm). At higher Mach number, the boundary layer is relatively thinner and the temperature in the boundary layer is significantly higher. This, in turn, results in higher rate of radiative transfer.

For a mixture of 50% H_2O in air, comparative results for the parallel plate channel and the circular tube are presented in Fig. 10 for two x -locations ($x=5$ and 10 cm). The results for the circular tube in general, exhibit the same trend as for the parallel plate geometry. Since the circular geometry provides additional degrees of freedom for radiative interactions [17], the rate of radiative transfer is higher for the tube.

The influence of radiative interactions in chemically reacting supersonic internal flows was investigated by considering the physical model shown in Fig. 1c. The specific problem considered is the supersonic flow of premixed hydrogen and air in a channel with a compression corner on the lower boundary. The physical dimensions considered for obtaining results are $L=2$ cm, $x_1=1$ cm, $x_2=2$ cm, $L_x=x_1+x_2=3$ cm, and $\alpha=10^\circ$. The inlet conditions, which are representative of the scramjet operating condition, are $P=1$ atm, $T=900$ K and $M=4.0$. The flow is ignited by the shock from the compression corner. The flowfield for this problem has been investigated by several researchers [21–28] where different chemistry models have been

used. Influence of radiative interactions was investigated in [25-27] by considering a simple two-step chemistry model. Recently [28], a comparative study of the flowfield was conducted by employing three chemistry models (see Table 1). It was found that significant amount of radiation participating species are produced by the 35-step chemistry model. The results presented in Figs. 3-10 provided essential information on radiative behavior of these species. Complete discussions on use of the three chemistry models with and without radiation are provided in [28]. Selected results are presented here to demonstrate the influence of radiative interactions.

The computed results for the 35-step chemistry model are presented in Figs. 11-14 with and without radiative interactions. The results were obtained by using a 31×31 grid; this was found to be an appropriate grid for the model. The variations in temperature, pressure, and species concentrations along the x-coordinate are shown for a y-location of 0.02 cm from the lower wall. The shock occurs at about $x/L_x = 1/3$, and it is noted that the 35-step chemistry model predicts the ignition time accurately. The temperature is seen to increase uniformly along the channel (Fig. 11) and there is a significant increase in pressure after the shock (Fig. 12). Results of Figs. 13 and 14 show that significant amounts of radiation participating species H_2O and OH are produced after the shock. The effect of radiative interaction is to lower the amount of species production due to radiative transfer in the x-direction.

The results of radiative transfer by the three chemistry models are compared in Figs. 15 and 16 at $y = 0.02$ cm. The results for the normal radiative flux presented in Fig. 15 demonstrate that radiative interactions increase rapidly after the shock. The three models are seen to predict the same general trend. The results of streamwise radiative flux illustrated in Fig. 16 show that the net q_{Rx} decreases towards the end of the channel. This is due to cancellation of fluxes in the positive and negative x-directions. It is noted that the net radiative transfer is in the negative x-direction. The 18-step and 35-step models are seen to predict significantly higher q_{Rx} than the 2-step model. This is because radiative heat transfer is a strong function of temperature, pressure and species concentration which are higher (in the positive x-direction) for the 18-step and 35-step models than the 2-step model.

Conclusions

Two-dimensional compressible Navier-Stokes equations have been used to investigate the influence of radiative energy transfer on the entrance region flow under supersonic flow conditions. Computational procedures have been developed to incorporate gray as well as nongray formulations for radiative flux in the general governing equations. Specific results have been obtained for different amounts of H_2O , OH and NO in combination with air. Results demonstrate that the radiative interaction increases with an increase in pressure, temperature and the amount of participating species. This can have a significant influence on the overall energy transfer in the system. Most energy, however, is transferred by convection in the flow direction. The radiative interactions in reacting flows have been investigated by considering the supersonic flow of premixed hydrogen and air in a channel with a compression corner at the lower boundary. Depending upon the chemistry model employed, the radiative interaction is seen to change significantly the temperature, pressure and species concentration in the flow direction.

Acknowledgments

This work was supported by the NASA Langley Research Center through Grants NAG-1-363 and NAG 1-423. The authors are indebted to Drs. D.J. Singh and M.H. Carpenter for their assistance during the course of this study.

References

1. Sparrow, E. M. and Cess, R. D., Radiation Heat Transfer, Brooks/Cole, Belmont, Calif., 1966 and 1970. New Augmented Edition, Hemisphere Publishing Corp., Washington, D.C., 1978.
2. Hottel, H. C. and Sarofim, A. F., Radiative Transfer, McGraw-Hill Book Co., New York, 1967.
3. Siegel, R. and Howell, J. R., Thermal Radiation Heat Transfer, McGraw-Hill Book Co., New York, 1971; Second Edition, 1981.
4. Ozisik, M. N., Radiative Transfer and Interaction with Conduction and Convection, John Wiley & Sons, Inc., New York, 1973.

5. Edwards, D. K., Radiation Heat Transfer Notes, Hemisphere Publishing Corporation, Washington, D.C., 1981.
6. Cess, R., "The Interaction of Thermal Radiation with Conduction and Convection Heat Transfer," Advances in Heat Transfer, Vol. 1, Academic Press, New York, 1964.
7. Sparrow, M., "Radiation Heat Transfer between Surfaces," Advances in Heat Transfer, Vol. 2, Academic Press, New York, 1965.
8. Viskanta, R., "Radiation Transfer and Interaction of Convection with Radiation Heat Transfer," Advances in Heat Transfer, Vol. 3, Academic Press, New York, 1966.
9. Tien, C. L., "Thermal Radiation Properties of Gases," Advances in Heat Transfer, Vol. 5, Academic Press, New York, 1968.
10. Cess, R. and Tiwari, S. N., "Infrared Radiative Energy Transfer in Gases," Advances in Heat Transfer, Vol. 8, Academic Press, New York, 1972.
11. Edwards, D. K., "Molecular Gas Band Radiation," Advances in Heat Transfer, Vol. 12, Academic Press, New York, 1976.
12. Tiwari, S. N., "Band Models and Correlations for Infrared Radiation," Radiative Transfer and Thermal Control (Progress in Astronautics and Aeronautics), Vol. 49, American Institute of Aeronautics and Astronautics, New York, 1976.
13. Tiwari, S. N., "Models for Infrared Atmospheric Radiation," Advances in Geophysics, Vol. 20, Academic Press, New York, 1978.
14. Viskanta, R., "Radiation Heat Transfer," Fortschrift der Verfahrenstechnik, Vol. 22A, 1984, pp. 51-81.
15. Viskanta, R. and Menguc, M. P., "Radiation Heat Transfer in Combustion Systems," Progress in Energy Combustion Sciences, Vol. 13, 1987, pp. 97-160.
16. Cess, R. D. and Tiwari, S. N., "Heat Transfer to Laminar Flow of an Absorbing-Emitting Gas Between Parallel Plates," Heat and Mass Transfer-USSR, Vol. 1, May 1968, pp. 229-283.
17. Tiwari, S. N. and Cess, R. D., "Heat Transfer to Laminar Flow of Nongray Gases Through a Circular Tube," Applied Scientific Research, Vol. 25, No. 314, December 1971, pp. 155-170.
18. Tiwari, S. N., "Applications of Infrared Band Model Correlations to Nongray Radiation," International Journal of Heat and Mass Transfer, Vol. 20, No. 7, July 1977, pp. 741-751.
19. Tiwari, S. N., "Radiative Interaction in Transient Energy Transfer in Gaseous System," NASA CR-176644, December 1985.
20. Tiwari, S. N. and Singh, D. J., "Interaction of Transient Radiation in Fully Developed Laminar Flow," AIAA Paper 86-1521, June 1987.
21. Kumar, A., "Numerical Simulation of Scramjet Inlet Flow Field," NASA TP-25117, May 1986.

22. Drummond, J. P., Hussaini, M. Y. and Zang, T. A., "Spectral Methods for Modelling Supersonic Chemically Reacting Flowfields," AIAA Journal, Vol. 24, No. 9, September 1986, pp. 1461-1467; also Drummond, J. P., "Numerical Simulation of a Supersonic Chemically Reacting Mixing Layers," Ph.D. Dissertation, George Washington University, May 1987.
23. Drummond, J. P., Rogers, R. C., and Hussaini, M. Y., "A Detailed Numerical Model of a Supersonic Reacting Mixing Layer," AIAA Paper No. 86-1427, June 1986.
24. Chitsomboon, T., Kumar, A., Drummond, J. P., and Tiwari, S. N., "Numerical Study of Supersonic Combustion Using a Finite-Rate Chemistry Model," AIAA Paper 86-0309, January 1986.
25. Mani, M., Tiwari, S. N., and Drummond, J. P., "Numerical Solution of Chemically Reacting and Radiating Flows," AIAA Paper 87-0324, January 1987.
26. Mani, M., Tiwari, S. N., and Drummond, J. P., "Investigation of Two-Dimensional Chemically Reacting and Radiative Supersonic Channel Flows," AIAA Paper 88-0462, January 1988.
27. Mani, M. And Tiwari, S. N., "Investigation of Supersonic Chemically Reacting and Radiating Channel Flow," NASA CR-182726, January 1988; also Ph.D. Dissertation by M. Mani, Old Dominion University, May 1988.
28. Chandrasekhar, R., Tiwari, S. N., and Drummond, J. P., "Radiative Interactions in a Hydrogen-Fueled Supersonic Combustor," AIAA Paper 91-0373, January 1991.
29. Anderson, D. A., Tannehil, J. C., and Pletcher, R. H., Computational Fluid Mechanics and Heat Transfer, Hemisphere Publishing Corporation, 1984.
30. Frankel, S. H., Drummond, J. P., and Hassan, H. A., "A Hybrid Reynolds Averaged/PDF Closure Model for Supersonic Turbulent Combustion," AIAA Paper 90-1573, ¹⁹⁹⁰ July
31. Patch, R., "Effective Absorption coefficient for Radiant Energy Transport in Nongray Nonscattering Gases," Journal of Quantitative Spectroscopy and Radiative Transfer, Vol. 7, No. 4, July/August 1967, pp. 611-637.
32. Smith, R. E. and Weigel, B. L., "Analytical and Approximation Boundary Fitted Coordinates System for Fluid Flow Simulation," AIAA Paper 80-0192, January 1980.
33. MacCormack, R. W., "The Effect of Viscosity in Hypervelocity Impact Cratering," AIAA Paper 69-354, May 1969.
34. Stalnaker, J. F., Robinson M. A., Spradley, L. W., Kurzius, S. C., and Theores, D., "Development of the General Interpolants Methods for the CYBER 200 Series of Computers," Report TR-0867354, Lockheed-Huntsville Research Engg. Center, Huntsville, Alabama, October 1983.
35. Bussing, T. R., and Murman, E. M., "A Finite Volume Method for the Calculation of Compressible Chemically Reacting Flows," AIAA Paper 85-0331, January 1985.

36. Wilkins, J. H., The Algebraic Eigenvalue Problem, Oxford University Press, Oxford, England, 1965, pp. 233-236.
37. Householder, A. S., The Theory of Matrices in Numerical Solution Analysis, Dover Publication, New York, 1964, pp. 122-140.
38. Rogers, R. C. and Schnexnayder, C. J., Jr. "Chemical Kinetic Analysis of Hydrogen-Air Ignition and Reaction Time," NASA TP-1856, 1981.
39. Rogers, R. C. and Chinitz, W., "Using a Global Hydrogen-Air Model in Turbulent Reacting Flow Calculations," AIAA Journal, Vol. 21, No. 4, April 1983.
40. Carpenter, M. H., "A Generalized Chemistry Version of SPARK," NASA CR-4196, December 1988.

Table 1. Hydrogen-Air Combustion Mechanism [40]

REACTION	A(moles)	N(cm ³)	E(calories/gm-mole)
** following reactions constitute the 18-step model **			
(1) $O_2 + H_2 \leftrightarrow OH + OH$	1.70×10^{13}	0	48150
(2) $O_2 + H \leftrightarrow OH + O$	1.42×10^{14}	0	16400
(3) $H_2 + OH \leftrightarrow H_2O + H$	3.16×10^7	1.8	3030
(4) $H_2 + O \leftrightarrow OH + H$	2.07×10^{14}	0	13750
(5) $OH + OH \leftrightarrow H_2O + O$	5.50×10^{13}	0	7000
(6) $H + OH + M \leftrightarrow H_2O + M$	2.21×10^{22}	-2.0	0
(7) $H + H + M \leftrightarrow H_2 + M$	6.53×10^{17}	-1.0	0
(8) $H + O_2 + M \leftrightarrow HO_2 + M$	3.20×10^{18}	1.0	0
(9) $OH + HO_2 \leftrightarrow O_2 + H_2O$	5.00×10^{13}	0	1000
(10) $H + HO_2 \leftrightarrow H_2 + O_2$	2.53×10^{13}	0	700
(11) $H + HO_2 \leftrightarrow OH + OH$	1.99×10^{14}	0	1800
(12) $O + HO_2 \leftrightarrow O_2 + OH$	5.00×10^{13}	0	1000
(13) $HO_2 + HO_2 \leftrightarrow O_2 + H_2O_2$	1.99×10^{12}	0	0
(14) $H_2 + HO_2 \leftrightarrow H + H_2O_2$	3.01×10^{11}	0	18700
(15) $OH + H_2O_2 \leftrightarrow H_2O + HO_2$	1.02×10^{13}	0	1900
(16) $H + H_2O_2 \leftrightarrow H_2O + OH$	5.00×10^{14}	0	10000
(17) $O + H_2O_2 \leftrightarrow OH + HO_2$	1.99×10^{13}	0	5900
(18) $H_2O_2 + M \leftrightarrow OH + OH + M$	1.21×10^{17}	0	45500
** remaining reactions complete the 35-step model **			
(19) $O_2 + M \leftrightarrow O + O + M$	2.75×10^{19}	-1.0	118700
(20) $N_2 + M \leftrightarrow N + N + M$	3.70×10^{21}	-1.6	225000
(21) $N + O_2 \leftrightarrow O + NO$	6.40×10^9	1.0	6300
(22) $N + NO \leftrightarrow O + N_2$	1.60×10^{13}	0	0
(23) $N + OH \leftrightarrow H + NO$	6.30×10^{11}	0.5	0
(24) $H + NO + M \leftrightarrow HNO + M$	5.40×10^{15}	0	-600
(25) $H + HNO \leftrightarrow H_2 + NO$	4.80×10^{12}	0	0
(26) $O + HNO \leftrightarrow OH + NO$	5.00×10^{11}	0.5	0
(27) $OH + HNO \leftrightarrow H_2O + NO$	3.60×10^{13}	0	0
(28) $HO_2 + HNO \leftrightarrow H_2O_2 + NO$	2.00×10^{12}	0	0
(29) $HO_2 + NO \leftrightarrow OH + NO_2$	3.43×10^{12}	0	-260
(30) $H + NO_2 \leftrightarrow OH + NO$	3.50×10^{14}	0	1500
(31) $O + NO_2 \leftrightarrow O_2 + NO$	1.00×10^{13}	0	600
(32) $NO_2 + M \leftrightarrow O + NO + M$	1.16×10^{16}	0	66000
(33) $M + OH + NO \leftrightarrow HNO_2 + M$	5.60×10^{15}	0	-1700
(34) $M + OH + NO_2 \leftrightarrow HNO_3 + M$	3.00×10^{15}	0	-3800
(35) $OH + HNO_2 \leftrightarrow H_2O + NO_2$	1.60×10^{12}	0	0
** following reactions constitute the global 2-step model [24, 27, 39] **			
(1'') $H_2 + O_2 \leftrightarrow 2 OH$	11.4×10^{17}	-10.0	4865
(2'') $2 OH + H_2 \leftrightarrow 2 H_2O$	2.50×10^{14}	-13.0	42500

STATE OF MICHIGAN

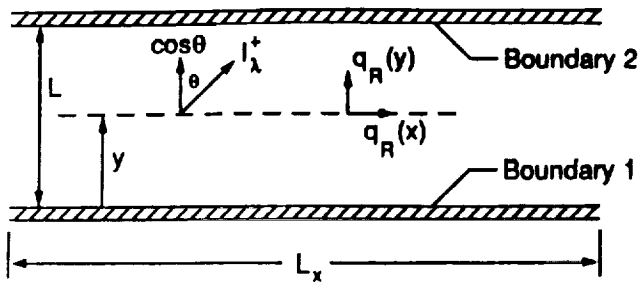


Fig. 1a Radiating gas flow between parallel boundaries.

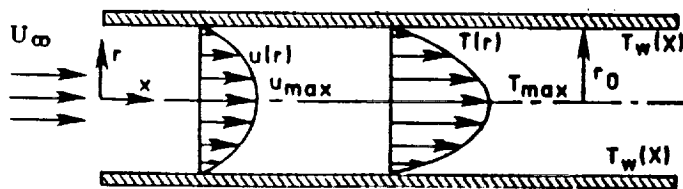


Fig. 1b Radiating gas flow within a circular tube.

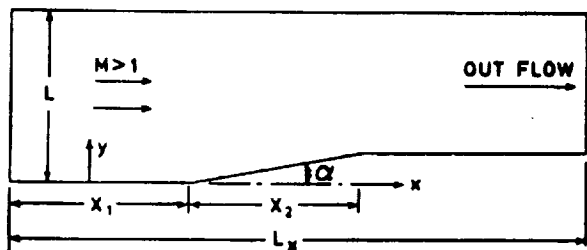


Fig. 1c Radiating gas flow in a channel with a compression-expansion ramp.

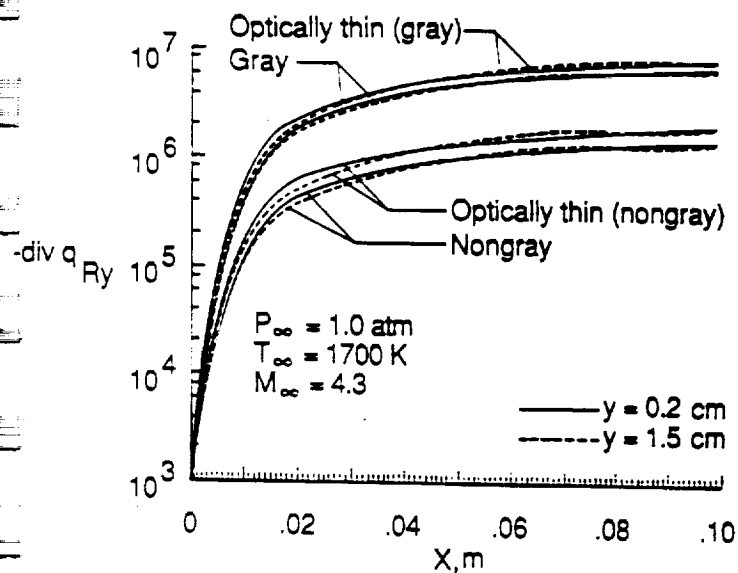


Fig. 2 Divergence of radiative flux along the channel for gray and nongray models, $M_\infty = 4.3$.

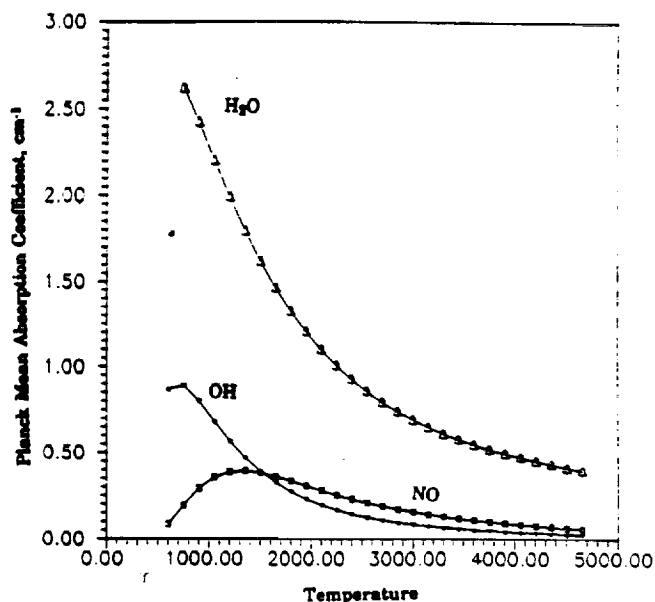


Fig. 3a Variation of the Planck-mean absorption coefficient for H_2O , NO, and OH.

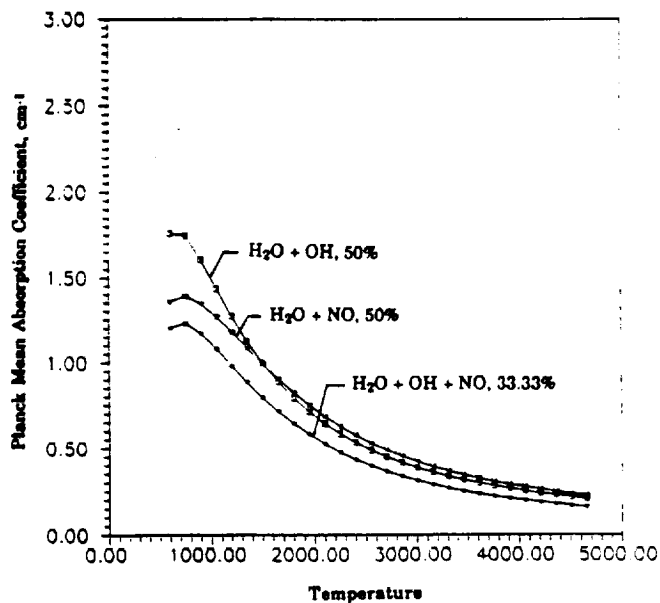


Fig. 3b Variation of the Planck-mean absorption coefficient for different mixtures of H_2O , NO, and OH.

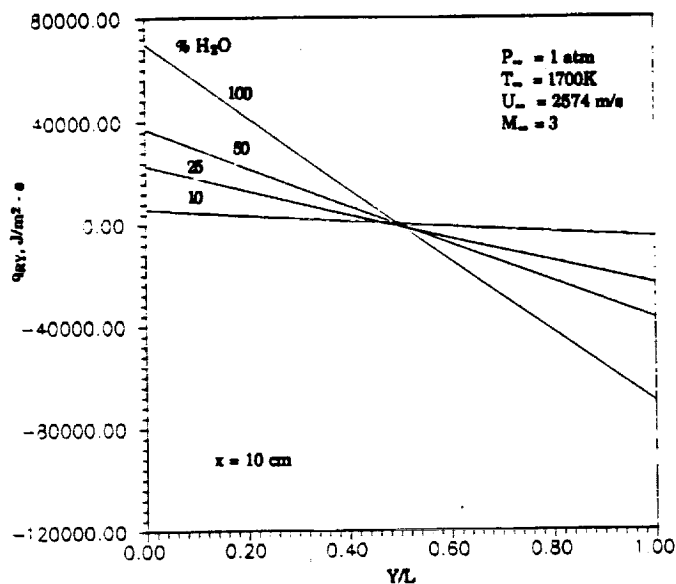


Fig. 4 Radiative flux vs. y at the channel exit, $M_\infty = 3.0$.

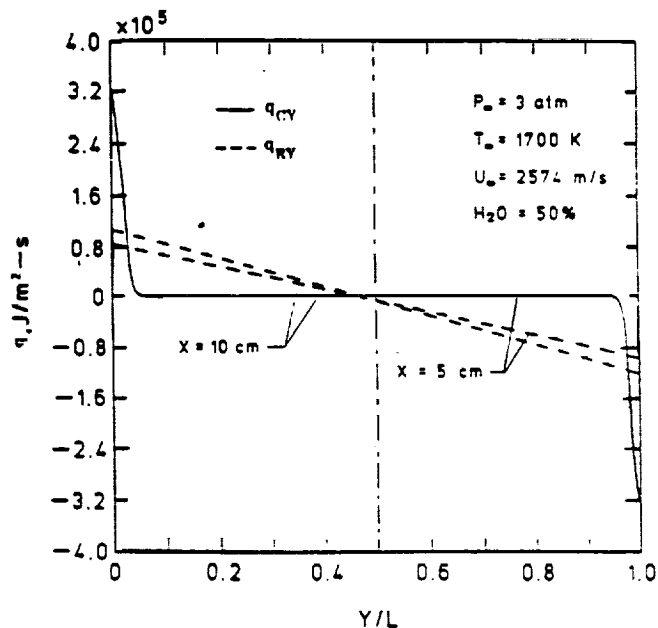


Fig. 6 Radiative and conductive fluxes vs. y for $P = 3$ atm, $x = 5$ and 10 cm, 50% H_2O , $M_\infty = 3.0$.

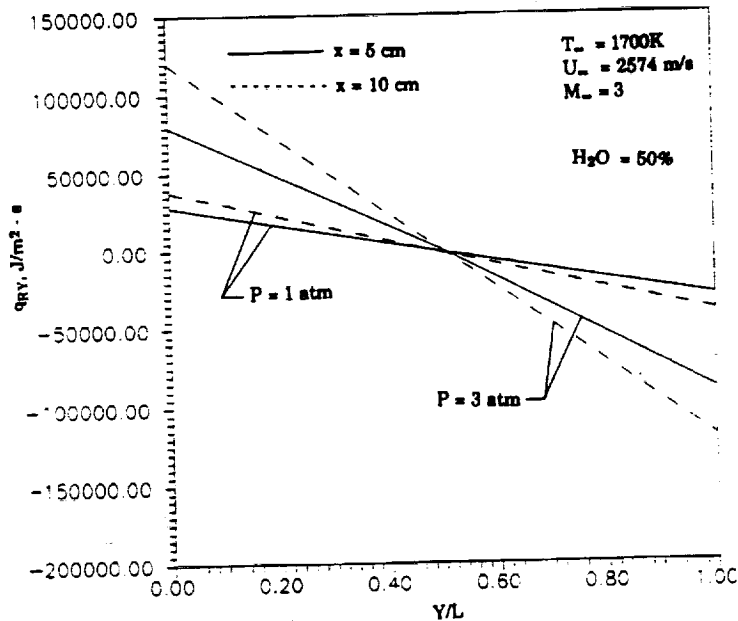


Fig. 5 Radiative flux vs. y for $P = 1$ and 3 atm, $x = 5$ and 10 cm, 50% H_2O , $M_\infty = 3.0$.

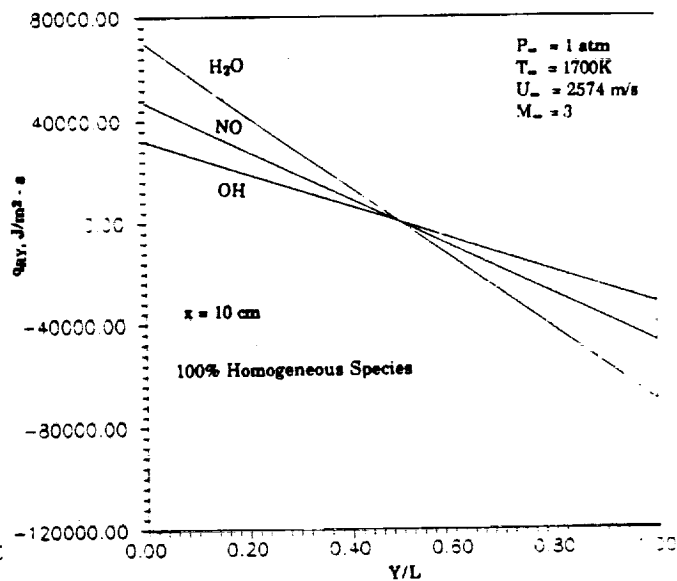


Fig. 7 Radiative flux vs. y for H_2O , NO , and HO , $P = 1$ atm, $M_\infty = 3.0$.

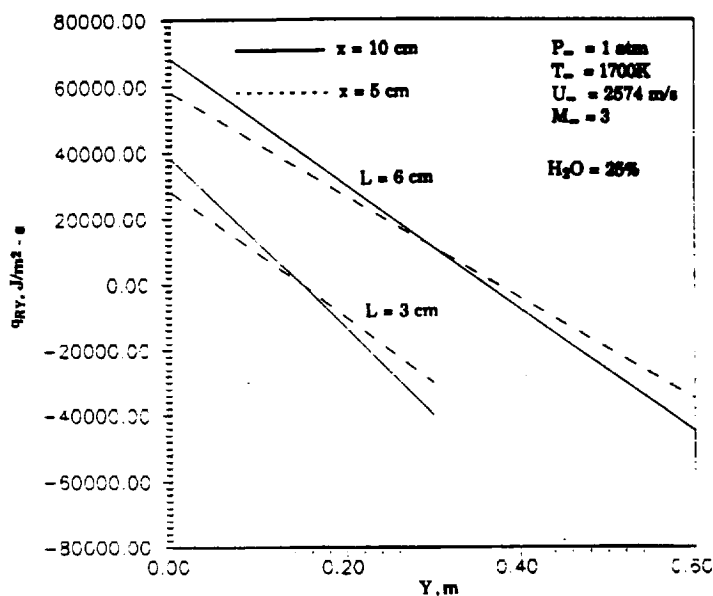


Fig. 8 Radiative flux vs. y for two different plate spacings ($L = 3$ and 6 cm) at $x = 5$ and 10 cm, $M_\infty = 3.0$.

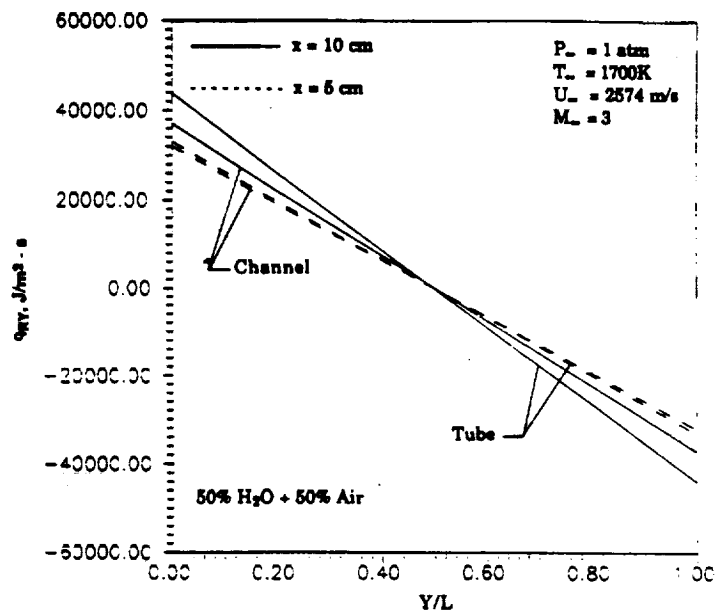


Fig. 10 Radiative flux vs. y for channel and tube ($L = D = 3$ cm) at $x = 5$ and 10 cm, $50\% \text{ H}_2\text{O}$, $M_\infty = 3.0$.

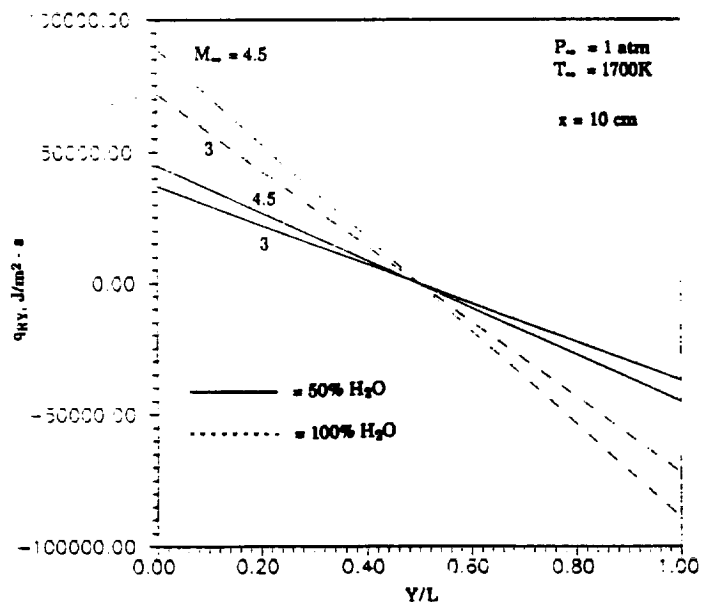


Fig. 9 Radiative flux vs. y for 50% and $100\% \text{ H}_2\text{O}$, $x = 10$ cm, $M_\infty = 3.0$ and 4.5 .

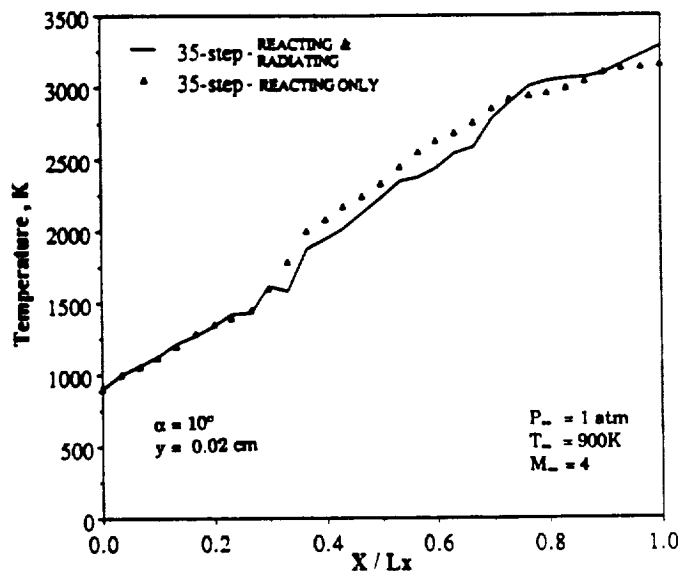


Fig. 11 Temperature variation with x for reacting, and reacting and radiating flows.

ORIGINAL PAGE IS
OF POOR QUALITY

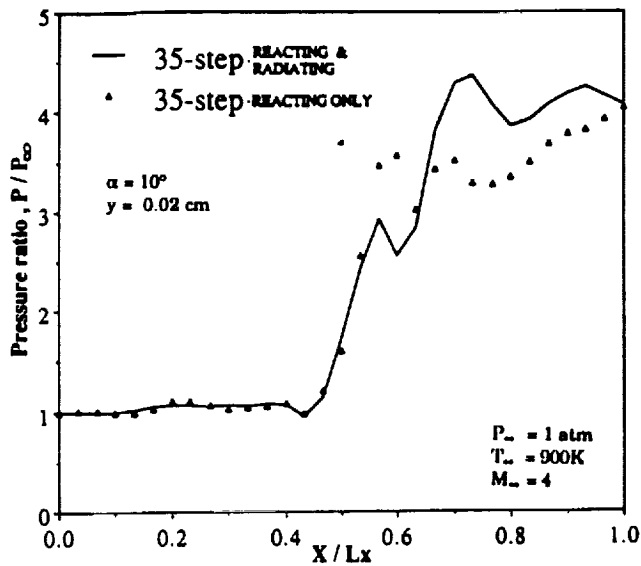


Fig. 12 Pressure variation with x for reacting, and reacting and radiating flows.

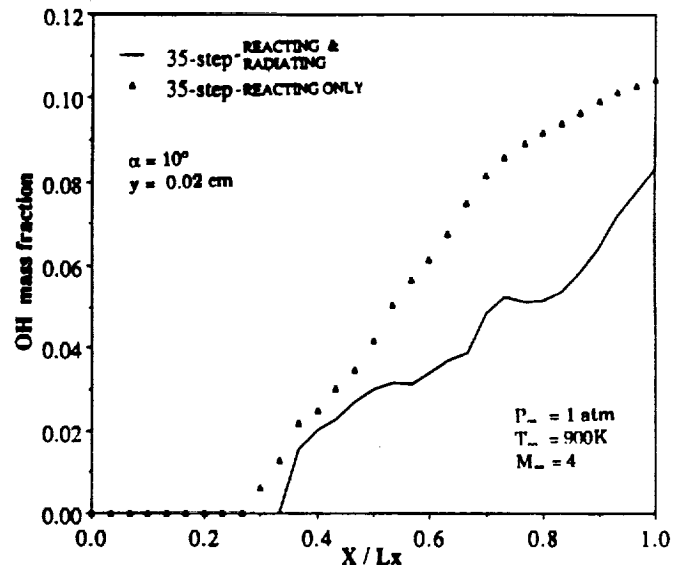


Fig. 14 Variation of OH mass fraction with x for reacting, and reacting and radiating flows.

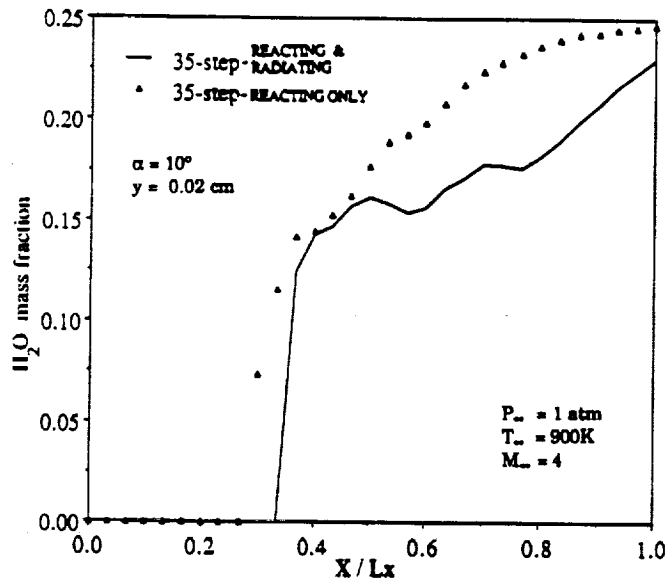


Fig. 13 Variation of H_2O mass fraction with x for reacting, and reacting and radiating flows.

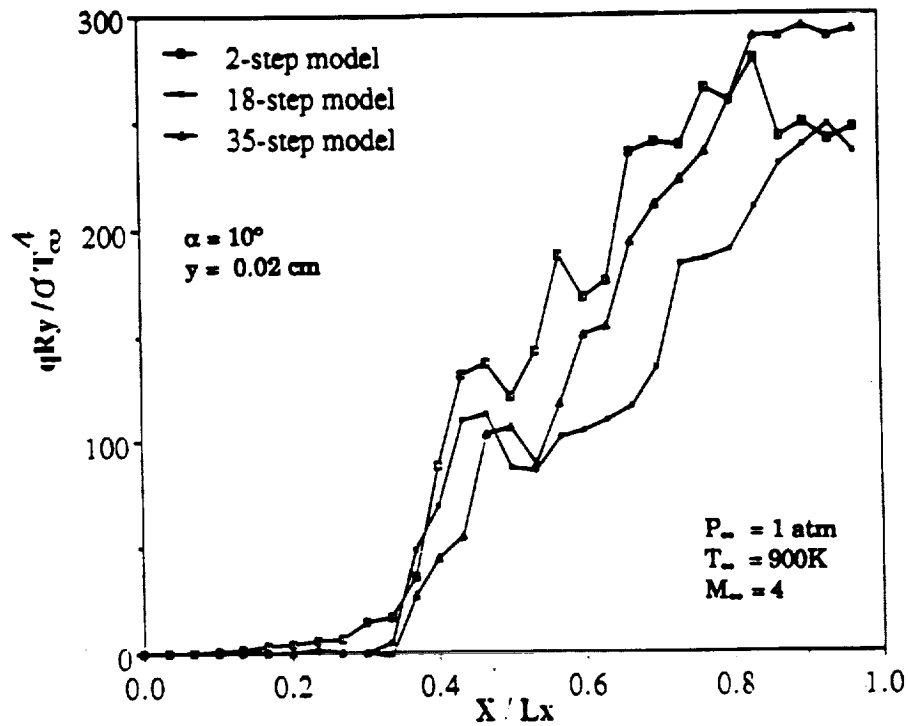


Fig. 15 Variation of normal radiative flux with x for three chemistry models.

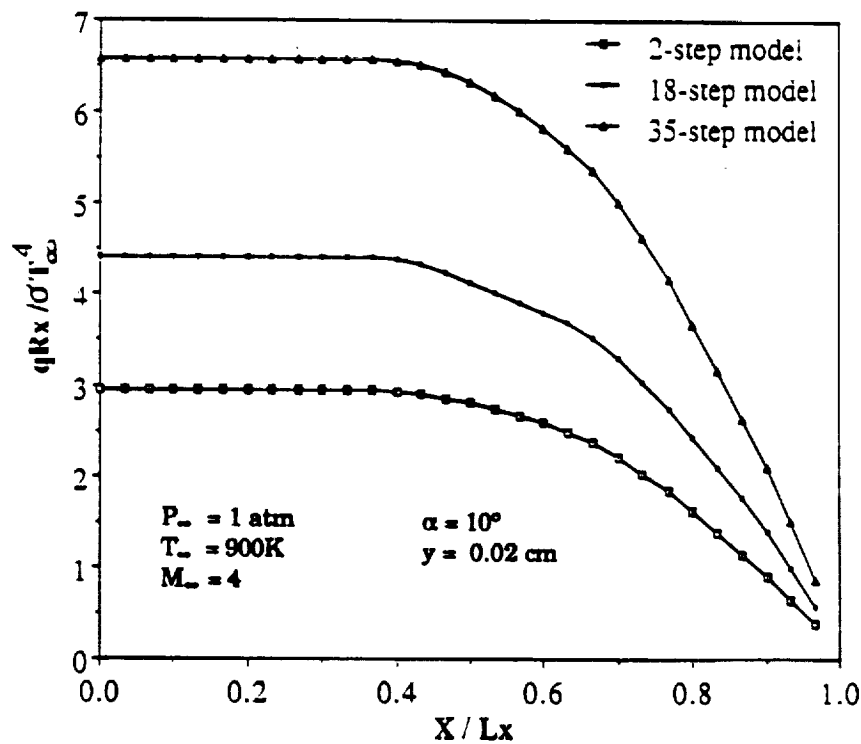


Fig. 16 Variation of streamwise radiative flux with x for three chemistry models.

PAGE _____ INTENTIONALLY BLANK